



저작자표시-비영리-변경금지 2.0 대한민국

이용자는 아래의 조건을 따르는 경우에 한하여 자유롭게

- 이 저작물을 복제, 배포, 전송, 전시, 공연 및 방송할 수 있습니다.

다음과 같은 조건을 따라야 합니다:



저작자표시. 귀하는 원저작자를 표시하여야 합니다.



비영리. 귀하는 이 저작물을 영리 목적으로 이용할 수 없습니다.



변경금지. 귀하는 이 저작물을 개작, 변형 또는 가공할 수 없습니다.

- 귀하는, 이 저작물의 재이용이나 배포의 경우, 이 저작물에 적용된 이용허락조건을 명확하게 나타내어야 합니다.
- 저작권자로부터 별도의 허가를 받으면 이러한 조건들은 적용되지 않습니다.

저작권법에 따른 이용자의 권리는 위의 내용에 의하여 영향을 받지 않습니다.

이것은 [이용허락규약\(Legal Code\)](#)을 이해하기 쉽게 요약한 것입니다.

[Disclaimer](#)

공학박사 학위논문

**Interfacial Structure Analysis Model for  
the Crystal Morphology Prediction of  
Centrosymmetric Growth Units**

계면 구조 분석 모델을 통한  
중심 대칭성 분자의 결정 형상 예측

2018 년 2 월

서울대학교 대학원

화학생물공학부

서 범 준

# Interfacial Structure Analysis Model for the Crystal Morphology Prediction of Centrosymmetric Growth Units

지도 교수 이윤우

이 논문을 공학박사 학위논문으로 제출함  
2018년 2월

서울대학교 대학원  
화학생물공학부  
서범준

서범준의 공학박사 학위논문을 인준함  
2018년 2월

위원장 이종민 (인)

부위원장 이윤우 (인)

위원 이원보 (인)

위원 김화용 (인)

위원 이홍식 (인)

# Abstract

## Interfacial Structure Analysis Model for the Crystal Morphology Prediction of Centrosymmetric Growth Units

Bumjoon Seo  
School of Chemical and Biological Engineering  
The Graduate School  
Seoul National University

Crystallization is used in various industries such as pharmaceutical, defense, food, electronics, and energy to obtain solid phase products. The quality of these products depends on their physical and chemical properties including polymorph, particle size, particle size distribution, morphology, and purity. Because these properties are determined by the crystallization process, predicting and controlling the crystal properties are essential parts of optimizing the process. Among those crystal properties, morphology has impacts on both the product efficacy and process efficiency such as the dissolution rate, bioavailability, reactivity, wettability, flowability and so on. Therefore, there have been continuous researches on developing models that can be used for predicting the crystal morphology. In these models, there are habit-controlling factors which are recognized as either internal or external. The internal factors include the crystal structure and interactions within the crystal, whereas external factors include the solvent, temperature, and supersaturation. Early models such as Bravais-Friedel-Donnay Harker model or Attachment Energy model considered only the internal factors, which is viable for crystal growth from vapor but not for growth from a solution. In order to predict the morphology of crystals grown from solution, mechanistic models such as two-dimensional nucleation growth model and spiral growth model were developed to account for the external habit controlling factors.

Among spiral growth models, the Interfacial Structure Analysis (ISA) model suggested two collective external habit-controlling factors. The first external habit-controlling factor is the anisotropic local concentration of the growth units at the interface. The second external habit-controlling factor is the orientational and conformational free energy barrier for reorientation of the growth units. In this model, an adsorbed growth unit with the orientation and conformation identical to that of a growth unit in the crystal is defined as the F1-unit. All the other adsorbed

growth units in the interfacial layer are defined as the F2-unit. The external factors are calculated from the concentration of the F2-units within one interplanar spacing from the surface and the free energy barriers between F2-units and F1-unit using molecular dynamics simulation of the solid-fluid interface. The relative growth rates of the faces are calculated by using these two external factors and spiral growth model based on the Burton-Cabrera-Frank theory.

In this dissertation, a model is developed that generalizes the previous ISA model and Extended Interfacial Structure Analysis (EISA) model with regard to the orientation and conformation of the growth unit. In the original ISA model, one angle was used whereas in the EISA model, more than two angles were used to identify the F1-unit. These methods are limited to simple molecular structures since sampling of the angles for complex molecules such as those containing rings becomes difficult within a molecular dynamics simulation. To overcome this difficulty, order parameters that can distinguish the F1-unit and F2-unit are used to reduce the dimensionality of the free energy surface. Moreover, metadynamics is used to cross the free energy barriers and calculate their heights in this lower dimension. By using this analysis and polygonal spiral growth model, the morphology of crystal comprised of centrosymmetric growth unit can be predicted.

Adipic acid crystal and  $\beta$ -HMX crystal are two representative crystals comprised of centrosymmetric growth units. For both crystals, the role of the anisotropic local concentration of the growth units at the interface as the habit controlling factor was found to be significant. As for the chain-like molecule of adipic acid, orientational free energy surface revealed that most of the molecules are adsorbed parallel to the surface with the azimuthal angle of  $\pi/2$ . This resulted in relative rate to be correlated with the azimuthal angle of the F1-unit, in that small azimuthal angle of the F1-unit require high free energy for ordering of the growth units. On the other hand, the orientational and conformational free energy surface of  $\beta$ -HMX obtained from metadynamics simulation with order parameters that identify F1-units showed that for all faces, the chair conformation of the crystal results in the instability of the F1-units at the interface. Therefore, all F2-units were assumed equivalent and only the local concentration of the growth units at the interface was used for the prediction of the morphology. For both crystals, polygonal spirals were assumed with appropriate rotation kinetics for different spiral geometries which showed more resemblance to the experimental morphologies than those obtained by using the original assumption of concentric circular spirals.

**Keyword : crystal morphology, spiral growth model, interfacial structure analysis model, metadynamics, dimensionality reduction, autoencoder neural network**

**Student Number : 2011-21038**

# Table of Contents

Chapter 1. Introduction.....	1
Chapter 2. Theoretical Background .....	3
2.1. Theory of Crystal Growth .....	3
2.1.1. Crystal Growth .....	3
2.1.2. Burton-Cabrera-Frank (BCF) Theory .....	7
2.1.3. Two-Dimensional Nucleation Theory .....	1 2
2.2. Morphology Prediction Models .....	1 4
2.2.1. Equilibrium Morphology of Crystals .....	1 4
2.2.2. Bravais-Friedel-Donnay-Harker (BFDH) Model .....	1 9
2.2.3. Hartman-Perdok Approach .....	2 1
2.2.4. Interfacial Structure Analysis Model .....	2 4
2.3. Centrosymmetric and Non-Centrosymmetric Growth Units ....	3 2
Chapter 3. Materials.....	3 4
3.1. Adipic Acid .....	3 4
3.1.1. Motivations for Predicting the Adipic Acid Morphology	3 4
3.1.2. Previous Studies on the Morphology of Adipic Acid.....	3 4
3.2. HMX .....	3 7
3.2.1. Motivations for Predicting the HMX Morphology .....	3 7
3.2.2. Previous Studies on the Morphology of HMX .....	3 7
Chapter 4. Computational Methods .....	4 1
4.1. Computational Methods Used for Adipic Acid Crystals .....	4 1

4.1.1. Periodic Bond Chain Analysis.....	4	1
4.1.2. Modified Attachment Energy Model .....	4	6
4.1.3. Interfacial Structure Analysis .....	4	8
4.1.4. Polygonal Spiral Growth Model .....	5	3
4.2. Computational Methods Used for $\beta$ -HMX Crystals.....	5	7
4.2.1. Periodic Bond Chain Analysis.....	5	7
4.2.2. Interfacial Structure Analysis .....	6	0
4.2.3. Metadynamics with Order Parameters .....	6	6
4.2.4. Generalized Interfacial Structure Analysis Model.....	7	9
Chapter 5. Results and Discussions .....	8	5
5.1. Morphology of the Adipic Acid Crystal.....	8	5
5.1.1. Orientational Free Energy Surface .....	8	5
5.1.2. Predicted Growth Morphology from Water .....	8	9
5.2. Morphology of the $\beta$ -HMX Crystal .....	9	3
5.2.1. Conformational Analysis of HMX Molecule .....	9	3
5.2.2. Orientational and Conformational Free Energy Surface	12	3
5.2.3. Predicted Growth Morphology from Acetone .....	12	8
Chapter 6. Conclusion .....	13	7
Bibliography .....	13	8
Abstract in Korean.....	14	9

## List of Figures

Figure 2-1. Incorporations in Kossel model of the crystal face (a) surface vacancy (b) edge vacancy (c) kink (d) edge and (e) step .....	5
Figure 2-2. Dependence of growth mechanism on supersaturation illustrated for an F-face [Lovette and Doherty, 2012]. .....	6
Figure 2-3. A schematic drawing of typical concentric circular growth spirals...	9
Figure 2-4. Drawings of spiral evolutions from a dislocation at different stages for (a) four sided spiral and (b) six sided spiral.....	1 0
Figure 2-5. Schematic drawing for the critical edge energy calculation.....	1 1
Figure 2-6. A curved surface ABCD and its displacement A'B'C'D' .....	1 8
Figure 2-7. Relations of tangential force on a face and interplanar spacings. .	2 0
Figure 2-8. Periodic Bond Chains and Attachment Energy. ....	2 3
Figure 2-9. A schematic drawing of the Interfacial Structure Analysis Model	2 7
Figure 2-10. Typical molecules whose crystals are comprised of (a) Centrosymmetric growth units (b) Non-centrosymmetric growth units. .	3 3
Figure 3-1. (a) Molecular structure and (b) Crystal structure of adipic acid. .	3 5
Figure 3-2. Schematic drawing of the interface of adipic acid crystal.....	3 6
Figure 3-2. (a) Molecular structure and (b) Crystal structure of $\beta$ -HMX. ....	3 8
Figure 3-2. Schematic drawing of the interface of $\beta$ -HMX crystal. ....	3 9
Figure 3-3. Optical observation of spirals for the (a) (020) and (b) (011) faces of $\beta$ -HMX crystals obtained by slow evaporation [Shim and Koo , 2015]. .	4 0
Figure 4-1. Bonding structures for the (a) (002), (b) (100), (c) ( <b>011</b> ), (d) (111), (e) (102), and (f) (202) faces of adipic acid crystal.....	4 2
Figure 4-2. Growth morphology of adipic acid crystal predicted by (a) BFDH model (b) AE model. ....	4 3
Figure 4-3. Growth morphology of adipic acid crystal predicted by different crystal structures, force fields, and charge sets. ....	4 4
Figure 4-4. Snapshots of the simulation cells for the different adipic acid crystal faces	5 0
Figure 4-5. Concentration of the adsorbed adipic acid molecules at the crystal- solution interface layer.....	5 1
Figure 4-6. Snapshots of the Connolly surfaces .....	5 2
Figure 4-7. Snapshots of the adsorbed growth units in the interface layer .....	5 2
Figure 4-8. Snapshots of the equilibrated growth units on the interface .....	5 2
Figure 4-9. Two-dimensional Bravais lattices. ....	5 4
Figure 4-10. Three-dimensional Bravais lattices .....	5 5
Figure 4-11. Possible shapes of growth spirals for the dominant faces of adipic acid crystal.....	5 6
Figure 4-12. Bonding structures for the (a) (020), (b) (011), (c) 110, and (d) (101) faces of $\beta$ -HMX crystal. .	5 8
Figure 4-13. Growth morphology of $\beta$ -HMX crystal predicted by (a) BFDH model and (b) AE model.....	5 9
Figure 4-14. HOMO isosurfaces and electrostatic potentials calculated for the chair and crown conformations of HMX with RESP formalism. ....	6 3
Figure 4-15. Concentration of the adsorbed HMX molecules at the crystal- solution interface layer.....	6 4
Figure 4-16. Local density values calculated on (a) (020), (b) (011), (c) (110), and (d) (101) faces. ....	6 5
Figure 4-17. Typical free energy barriers related to rare event problems. ....	6 9

Figure 4-18. Canonical conformations of cyclooctane by Evans and Boeyens [Evans and Boeyens, 1988]. .....	7 4
Figure 4-19. A schematic drawing of quaternions defined on atomic coordinates of HMX molecules. ....	7 8
Figure 4-20. Attachment and detachment rates of the growth units around kink sites	8 2
Figure 4-21. Free energy barriers related to the incorporation of solvated growth units into kinks from the solution. ....	8 3
Figure 4-22. The relation between edge length and propagation length for different number of nearest neighbors. ....	8 4
Figure 5-1. Free energy of the adsorbed adipic acid molecules plotted against the angle between the surface normal and C-C backbone of the F2-units.....	8 7
Figure 5-2. Free energy of the adsorbed adipic acid molecules plotted against both azimuthal and altitude angles.....	8 8
Figure 5-3. Adipic acid crystal morphology predicted by the original interfacial structure analysis model. ....	9 1
Figure 5-4. Adipic acid crystal morphology predicted by the modified interfacial structure analysis model. ....	9 2
Figure 5-5. Three-dimensional representation of the five-dimensional conformational space for cyclooctane [Allen et al., 1996] .....	9 5
Figure 5-6. Evans and Boeyens plot of the MD simulations using charge set and starting conformation of (a) AM1-BCC/crown, (b) AM1-BCC/crown, (d) RESP/crown, and (e) RESP/chair and Metadynamics simulations using charge set and starting conformation of (c) AM1-BCC/chair and (f) RESP/chair.	9 6
Figure 5-7. Evans and Boeyens plot of the MD simulations using AM1-BCC charge set and starting conformation of (a) chair, (b) crown, and (c) boat-boat .....	9 7
Figure 5-8. Polar Cremer-Pople puckering coordinates obtained from MD simulation of the chair family. ....	9 9
Figure 5-9. Polar Cremer-Pople puckering coordinates obtained from MD simulation of the crown family. ....	1 0 0
Figure 5-10. Polar Cremer-Pople puckering coordinates obtained from MD simulation of the boat family. ....	1 0 1
Figure 5-11. Cartesian Cremer-Pople puckering coordinates obtained from MD simulation of the chair family. ....	1 0 2
Figure 5-12. Cartesian Cremer-Pople puckering coordinates obtained from MD simulation of the crown family. ....	1 0 3
Figure 5-13. Cartesian Cremer-Pople puckering coordinates obtained from MD simulation of the boat family. ....	1 0 4
Figure 5-14. Cartesian Cremer-Pople puckering coordinates for $m = 2$ and $3$ obtained from MD simulation of the chair family. ....	1 0 5
Figure 5-15. Cartesian Cremer-Pople puckering coordinates for $m = 2$ and $3$ obtained from MD simulation of the crown family. ....	1 0 5
Figure 5-16. Cartesian Cremer-Pople puckering coordinates for $m = 2$ and $3$ obtained from MD simulation of the boat family. ....	1 0 5
Figure 5-17. Phase angle components of the polar Cremer-Pople puckering coordinates obtained from MD simulation of the chair family. ....	1 0 6
Figure 5-18. Phase angle components of the polar Cremer-Pople puckering coordinates obtained from MD simulation of the crown family. ....	1 0 6
Figure 5-19. Phase angle components of the polar Cremer-Pople puckering coordinates obtained from MD simulation of the boat family. ....	1 0 6
Figure 5-20. Representative phase angle components of the polar Cremer-Pople puckering coordinates obtained from MD simulation of the chair family .	1 0 7

Figure 5-21. Representative phase angle components of the polar Cremer-Pople puckering coordinates obtained from MD simulation of the crown family	1 0 7
Figure 5-22. Representative phase angle components of the polar Cremer-Pople puckering coordinates obtained from MD simulation of the boat family..	1 0 7
Figure 5-23. Structure of the autoencoder neural network. ....	1 0 9
Figure 5-24. Mean squared error of the input and reconstructed data. ....	1 1 0
Figure 5-25. Comparison of the (a) input data and (b) reconstructed data in the test set. ....	1 1 1
Figure 5-26. A three-dimensional visualization of the conformational space of HMX obtained from (a) MD simulations of ●: chair, ●: crown, and ●: boat families, (b) metadynamics simulations starting from chair conformation, and (c) overlap. ....	1 1 2
Figure 5-27. Polar Cremer-Pople puckering coordinates of $\beta$ -HMX at 0 K.	1 1 4
Figure 5-28. Cartesian Cremer-Pople puckering coordinates of $\beta$ -HMX at 0 K	1 1 5
Figure 5-29. Polar Cremer-Pople puckering coordinates of $\beta$ -HMX at 293.15 K	1 1 6
Figure 5-30. Cartesian Cremer-Pople puckering coordinates of $\beta$ -HMX at 293.15 K	1 1 7
Figure 5-31. Cartesian Cremer-Pople puckering coordinates of $\beta$ -HMX for $m = 3$ at 0 K. ....	1 1 8
Figure 5-32. Cartesian Cremer-Pople puckering coordinates of $\beta$ -HMX for $m = 3$ at 293.15 K. ....	1 1 8
Figure 5-33. Phase angle components of the polar Cremer-Pople puckering coordinates of $\beta$ -HMX at 0 K. ....	1 1 9
Figure 5-34. Representative phase angle components of the polar Cremer-Pople puckering coordinates of $\beta$ -HMX at 0 K. ....	1 1 9
Figure 5-35. Phase angle components of the polar Cremer-Pople puckering coordinates of $\beta$ -HMX at 293.15 K. ....	1 2 0
Figure 5-36. Representative phase angle components of the polar Cremer-Pople puckering coordinates of $\beta$ -HMX at 293.15 K. ....	1 2 0
Figure 5-37. Order parameter S1 defined from the Cremer-Puckering coordinates.	1 2 2
Figure 5-38. Typical free energy surfaces with regard to the order parameters obtained from the metadynamics simulations. ....	1 2 5
Figure 5-39. String evolution and transition tube by Finite Temperature String method on the free energy surfaces for (a) 020, (b) (011), (c) (110), and (d) (101) faces. ....	1 2 6
Figure 5-40. Free energy along the minimum energy path for the (a) 020, (b) (011), (c) (110), and (d) (101) faces. ....	1 2 7
Figure 5-41 Schematic diagram of the GAS process apparatus. ....	1 3 1
Figure 5-42. $\beta$ -HMX crystal morphology predicted by the generalized interfacial structure analysis model. ....	1 3 3
Figure 5-42. Morphology of the $\beta$ -HMX crystal obtained by using GAS process.	1 3 4
Figure 5-42. XRD pattern of the $\beta$ -HMX crystal obtained by using GAS process.	1 3 5
Figure 5-43. Comparison of the predicted morphology with the experimentally obtained $\beta$ -HMX crystal morphology at various angles. ....	1 3 6

## List of Tables

Table 4-1 Interplanar distances and attachment energies for the F-faces of adipic acid .....	4 3
Table 4-2. Atomic partial charges of the adipic acid molecule .....	4 5
Table 4-3. Interaction energies for the F-faces of the adipic acid crystal. ....	4 7
Table 4-4. Modified attachment energies and relative growth rates for the F-faces of the adipic acid crystal .....	4 7
Table 4-5 Interplanar distances and attachment energies for the F-faces of $\beta$ -HMX	5 9
Table 4-6. Atomic partial charges of the HMX molecule by the AM1-BCC model within GAFF for the chair conformation.....	6 2
Table 4-7. Atomic partial charges of the HMX molecule by the AM1-BCC model within GAFF for the crown conformation.....	6 2
Table 4-8. Atomic partial charges of the HMX molecule by the AM1-BCC model within GAFF for the boat-boat conformation.....	6 2
Table 4-9. Atomic partial charges of the HMX molecule by the RESP formalism within GAFF.....	6 2
Table 5-1 External habit-controlling factors obtained from ISA on the F-Faces of adipic acid crystals.....	9 0
Table 5-2 Habit-controlling factors and relative growth rates for the F-Faces of adipic acid crystals .....	9 0
Table 5-3 Parameters used for the calculation of the molecular order parameters	1 2 1
Table 5-4 Operating conditions for the GAS process .....	1 3 0
Table 5-5 External habit-controlling factors obtained from ISA on the F-Faces of adipic acid crystals.....	1 3 2
Table 5-6 Habit-controlling factors and relative growth rates for the F-Faces of $\beta$ -HMX crystals .....	1 3 2

# Chapter 1. Introduction

Crystallization is involved in various industries such as the pharmaceuticals, defense, and food industry since more than 90% of all pharmaceutical products and practical molecular explosives are provided in solid phases. As a unit process, it affects various properties such as crystal phase, mean size, size distributions, morphology, purity, etc. As one of the main factors, morphology has impacts on end-use efficacy (dissolution rate, bioavailability, reactivity), downstream processing efficiency (flowability, wettability), and convenience in handling (bulk density, thermal/mechanical stability) [Lovette, 2008]. Therefore, understanding the growth morphology of a crystal is critical for optimizing its industrial crystallization process.

The equilibrium morphology of a crystal can be unambiguously determined from the surface free energies of the faces. However, the growth morphology, which is of more interest, is determined from the kinetic factors which are more difficult to estimate. These kinetic factors, or the habit-controlling factors, can be divided into two categories: internal factors and external factors. The well-known internal factors include crystal structure and interaction between crystalline molecules while external factors include solvent, temperature, and driving force (supersaturation).

Earlier approaches could only utilize the internal factors which are solely based on the interactions between the molecules within the crystal. These ad-hoc recipes remain successful for vapor grown crystals. However, the external factors cannot be ignored for solution grown crystals which led to the development of various mechanistic models. These mechanistic models are built upon the idea that there is a dominant mechanism among simultaneously working growth mechanisms whose rates depend on the internal and external factors. It is well established that at low enough supersaturations, the spiral growth mechanism is dominant while transition to two-dimensional nucleation mechanism dominant region is observed as the supersaturation goes higher. At higher enough supersaturations, rough growth mechanism is dominant. At typical industrial crystallization conditions, fast consumption of supersaturation by nucleation leads to spiral growth of the crystals. This necessitates the understanding of the growth kinetics modeled by the spiral growth mechanism.

As the spiral growth model was refined for the purpose of morphology prediction, various concepts such as the step velocity, kink energy, and kink rate were integrated to form more reliable predictions. In the approaches called the interfacial structure analysis model, two additional factors of the local

concentration of the growth units at the interface and orientational or conformational free energy barrier for the pre-ordering of the growth units are considered important. The main drawback of interfacial structure analysis model is that computationally expensive molecular dynamics (MD) have to be conducted to obtain the necessary parameters. But as the computational resources are becoming more available, these methods are receiving more attention.

In the following chapters, the principles of spiral growth models viewed from the interfacial structure analysis model are revised to appropriately account for the recently devised spiral growth kinetics such as the spiral geometries and kink rates. Moreover, using the concepts of order parameters with the metadynamics simulation, sampling of the conformational free energy surface is enabled. With these generalized interfacial structure analysis model, two of the most commonly studied crystals comprised of centrosymmetric growth units are considered: adipic acid and  $\beta$ -HMX. The resulting morphologies show remarkable agreement to the experimental morphologies and reveal solute behaviors in relation to the orientational and conformational free energy surfaces.

## Chapter 2. Theoretical Background

### 2.1. Theory of Crystal Growth

#### 2.1.1. Crystal Growth

A solid phase and its saturated solution are in thermodynamic equilibrium. In order for the solid phase in contact with a fluid phase to grow, a driving force is essential. This driving force for crystallization is expressed as

$$\frac{\Delta\mu}{k_B T} = \ln \frac{a_A}{a_{A,eq}} \approx \ln \frac{x_A}{x_{A,eq}} \quad (1)$$

where  $\Delta\mu$  is the difference of chemical potential in the solid and fluid phase,  $a_A$  is the activity of the solute in fluid phase,  $a_{A,eq}$  is the activity of the solute in a saturated solution,  $x_A$  is the concentration of solute in the fluid phase, and  $x_{A,eq}$  is the solubility. This driving force is related to the supersaturations expressed as in either the supersaturation ratio  $S$  or the relative supersaturation  $\sigma$

$$S = \frac{x_A}{x_{A,eq}} \quad (2)$$

$$\sigma = \frac{x_A - x_{A,eq}}{x_{A,eq}} = S - 1 \quad (3)$$

Considering the solid phase, the growth occurs by attachment and detachment of growth units existing on the crystal face. Kossel model [Kossel, 1927; Stranski, 1928] describes the equilibrium structure of a crystal surface in terms of the sites for growth (Figure 2-1). These sites are identified by the number of saturated bonds and unsaturated bonds. A growth unit can be incorporated into (1) surface vacancies (5 saturated bonds and 1 unsaturated bond), (2) edge vacancies (4 saturated bonds and 2 unsaturated bonds), (3) kinks (3 saturated bonds and 3 unsaturated bonds), (4) steps (2 saturated bonds and 4 unsaturated bonds), and (5) terrace (1 saturated bond and 5 unsaturated bonds). In growth mechanisms, the kink sites are of the most importance among all the incorporation sites. The reason is that the kinks are the only sites for attachment and detachment of the growth units which (1) does not alter the surface free energy of the edges and (2) regenerate a new kink after the incorporation. Therefore, the growth by expansion along the step proceeds by the movement of kink sites along the step.

The actual process of the growth from solution occurs by individual processes which are

- (1) the volume (or bulk) diffusion of the growth units from the bulk solution to the face
- (2) the surface diffusion of the growth units from the terrace to near kink sites
- (3) the desolvation and incorporation of the growth units into the kink sites
- (4) the release of the latent heat of crystallization

The growth rates of different mechanisms are dependent on the supersaturation and temperature of the system. A crystal face will grow by the mechanism with the fastest growth rate. At low supersaturations, layered growth mechanism of spiral growth and two-dimensional nucleation growth will be dominant as long as the temperature is below the roughening temperature of the face. At high supersaturations, the face will grow by a rough growth with a linear dependence on the supersaturation because the activation energy for the formation of a critical nucleus is small. This is called the kinetic roughening. On the other hand, a face at a temperature above its roughening temperature will be rough on the atomic scale by a phase transition of the surface. This is called the thermal roughening.

It is generally assumed that for growth from solution, the growth rate of layered growth mechanism is limited by the surface integration (step 3 above), whereas that of rough growth mechanism is limited by the bulk transport (step 1 above).

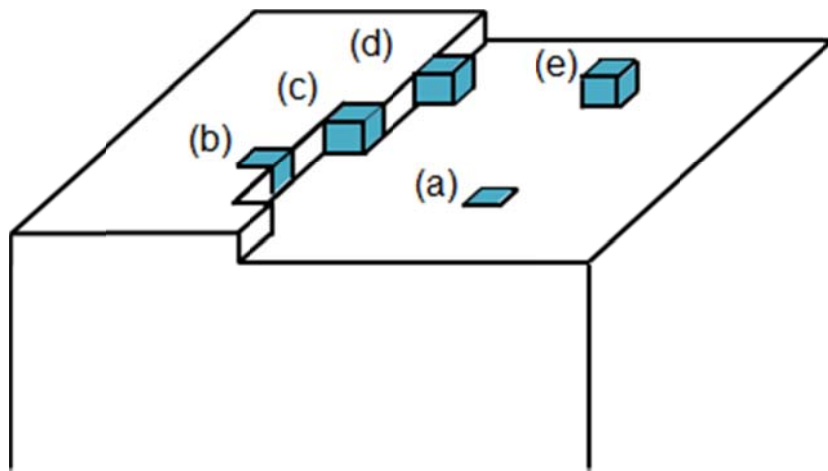


**Figure 2-1. Incorporations in Kossel model of the crystal face**  
(a) surface vacancy (b) edge vacancy (c) kink (d) edge and (e) step

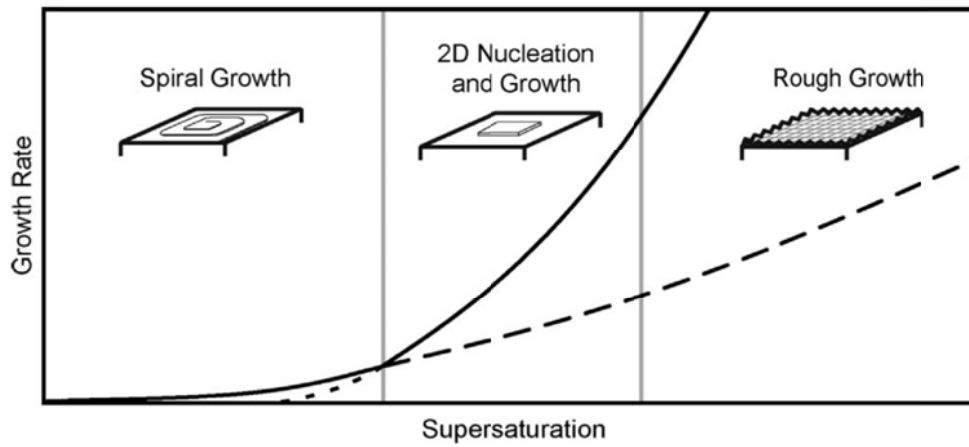


**Figure 2-2. Dependence of growth mechanism on supersaturation illustrated for an F-face [Lovette and Doherty, 2012].**

## 2.1.2. Burton-Cabrera-Frank (BCF) Theory

Crystals are known to grow at low supersaturations, even far below that needed for surface nucleation. This occurs by a growth spiral starting from a screw dislocation which acts as a permanent source of steps once it is formed [Frank, 1949]. The growth rate  $G_{hkl}$  of a face that grows with spiral growth mechanism can be expressed as [Burton et al., 1951]

$$G_{hkl} = \frac{h_{hkl}v_{hkl}}{\lambda_0} \quad (4)$$

where  $h_{hkl}$  is the step height which is generally equivalent to the interplanar spacing  $d_{hkl}$ ,  $v_{hkl}$  is the lateral velocity of the steps, and  $\lambda_0$  is the average distance between successive steps. This relation can be reformulated as

$$G_{hkl} = \frac{h_{hkl}}{\tau_{hkl}} \quad (5)$$

where the height of the step  $h_{hkl}$  is the interplanar spacing  $d_{hkl}$  and the rotation time  $\tau_{hkl}$  is the time required for one full turn of the spiral.

To determine the rotation time of a polygonal spiral, the step velocity profile with respect to the edge length  $l_i$  is required. The profile according to Gibbs-Thomson relationship is [Teng et al., 1998]

$$v_i = \begin{cases} 0 & \text{for } l_i < l_c \\ v_{\infty,i} \left(1 - \frac{e^{\sigma l_{c,i}/l_i} - 1}{e^{\sigma} - 1}\right) & \text{for } l_i \geq l_c \end{cases} \quad (6)$$

while a more simplified profile for low supersaturations proposed by Kaischew [Kaischew and Budevski, 1967] and later by Voronkov [Voronkov, 1973] is,

$$v_i = \begin{cases} 0 & \text{for } l_i < l_c \\ v_{\infty,i} & \text{for } l_i \geq l_c \end{cases} \quad (7)$$

Voronkov profile has been used for most of the spiral growth models. The more general case for the Voronkov profile was suggested by Chernov and others [Chernov et al., 2004] as an implicit expression of

$$\frac{l_i}{l_{c,i}} = \left( \frac{\phi_{i-1}^{edge} + \phi_{i+1}^{edge}}{k_B T} \right)^{-1} \left( \frac{y_i}{(1 - y_i^2)^{\frac{1}{2}}} \right) (\pi + 2 \arcsin(y_i)) + \frac{l_i^*}{l_{c,i}} \quad (8)$$

where  $y_i \equiv v_i/v_{\infty,i}$ ,  $\phi_i^{edge}$  is the edge energy on a molecule basis and  $l_i^*$  is a correction for stochastic nature of the edge. In this work, Voronkov profile is used, since this is sufficiently accurate for most industrial crystallization of organic molecules [Lovette and Doherty, 2012].

The rotation time for N-sided spiral is dependent on only the first turn for each sides of the spiral. Summing all the time required for the first turn for each sides, the equation for the one full rotation time for a spiral is obtained as [Snyder and Doherty, 2009]

$$\tau_{hkl} = \sum_{i=1}^N \frac{l_{c,i+1} \sin(\alpha_{i,i+1})}{v_i} \quad (9)$$

where  $l_{c,i}$  is the critical length of edge  $i$ ,  $\alpha_{i,i+1}$  is the angle between edge  $i$  and  $i + 1$ , and step velocity  $v_i$  is the lateral velocity of edge  $i$ . The critical length  $l_{c,i}$  of a spiral segment obeying the Gibbs-Thomson law is obtained by considering the free energy difference for adding a segment of  $n$  growth units to the edge [Lovette and Doherty, 2011].

$$\frac{\Delta G(n)}{k_B T} = 2 \left( \frac{\phi_i^{kink}}{k_B T} \right) (1 - \delta_n) - n\sigma \quad (10)$$

The free energy difference  $\Delta G(n)$  is zero for the critical length  $l_{c,i} = n_{c,i} a_{e,i}$ , resulting in

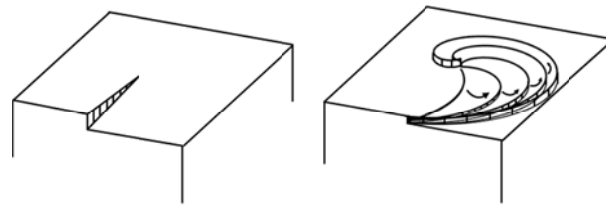
$$l_{c,i} = \frac{2a_{e,i}}{\sigma} \left( \frac{\phi_i^{kink}}{k_B T} \right) \quad (11)$$

where  $a_{e,i}$  is the distance between growth units along edge  $i$ , and the kink energy  $\phi_i^{kink}$  is the work or free energy change required to form a kink on edge  $i$ .

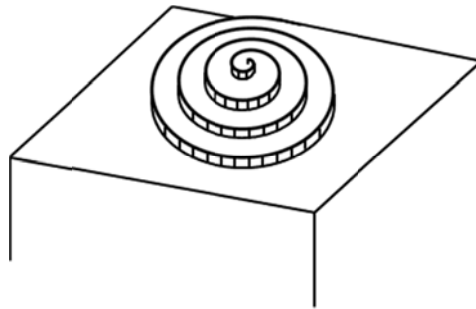
The Burton-Cabrera-Frank relationship between the growth rate and supersaturation is written as

$$R = A\sigma^2 \tanh(B/\sigma) \quad (12)$$

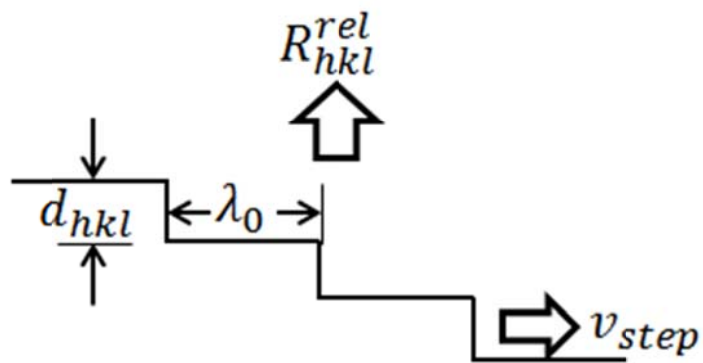
where  $A$  and  $B$  are constants depending on the temperature and identity of the face. At low supersaturation, this relationship approximates to  $R \propto \sigma^2$  (parabolic growth law) thereby, the relative growth rate  $R$  being independent of  $\sigma$ . At high supersaturations, the relationship approximates to  $R \propto \sigma$  (linear growth law).



(a)



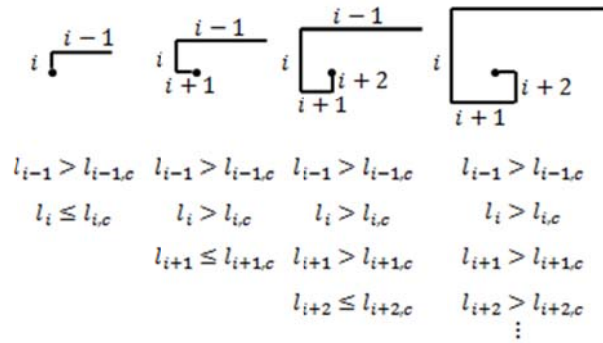
(b)



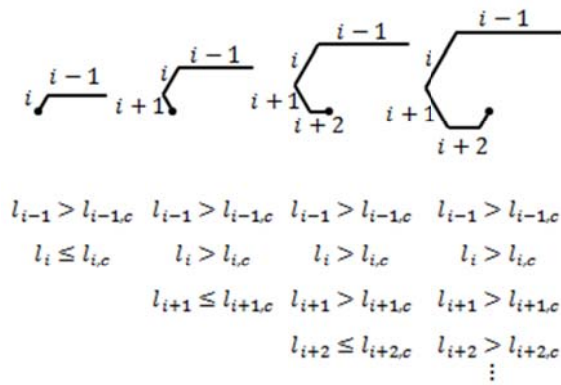
(c)

**Figure 2-3. A schematic drawing of typical concentric circular growth spirals.**

**(a) spiral evolution from screw dislocation (b) top view (b) side view**



(a)



(b)

Figure 2-4. Drawings of spiral evolutions from a dislocation at different stages for (a) four sided spiral and (b) six sided spiral

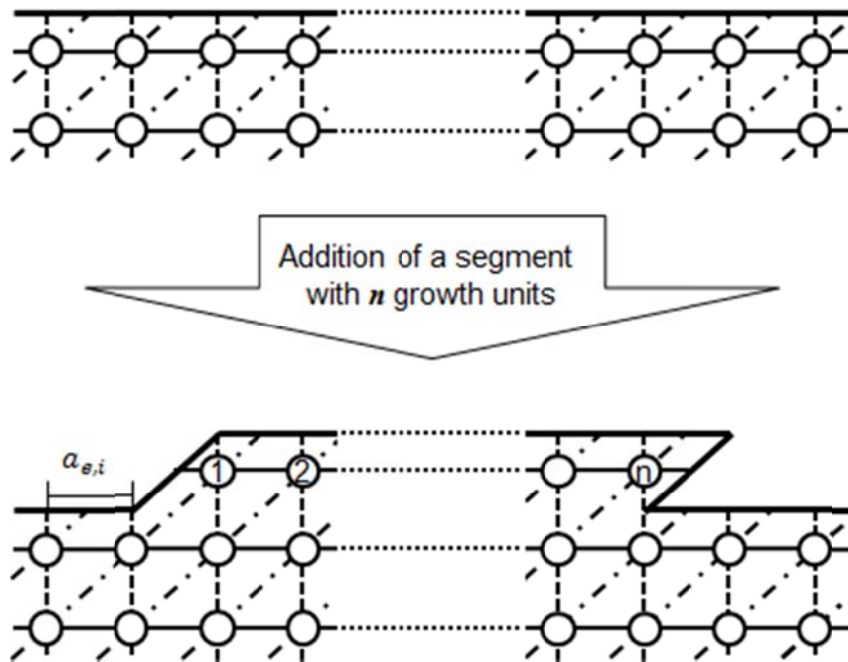


Figure 2-5. Schematic drawing for the critical edge energy calculation.

### 2.1.3. Two-Dimensional Nucleation Theory

For the case of a defectless crystal, two dimensional nuclei is another source of steps which can provide kink sites for incorporation [Volmer and Marder, 1931; Kaischew and Stranski, 1934]. In the traditional two-dimensional nucleation mechanism of birth and spread model, a disk shaped nuclei with isotropic edge velocities are considered [Ohara and Reid, 1973]. The two-dimensional nucleation is an energetically activated process in which the critical free energy barrier  $\Delta G_c$  should be overcome for the growth to take place. The nucleation rate for this case is given as

$$J = \kappa_{2D} \exp\left(-\frac{\Delta G_c}{k_B T}\right) \quad (13)$$

For the kinetic prefactor  $\kappa_{2D}$ , various expressions were suggested including that by Nielsen as,

$$\kappa_{2D} = \mathcal{D}/h^4 \quad (14)$$

where  $\mathcal{D}$  is the diffusion coefficient of the solute in solution and  $h$  is the height of the layer [Nielsen, 1964]. Ohara and Reid suggested

$$\kappa_{2D} = \frac{2\bar{v}\eta_1^2}{\pi} \left(\frac{v_m}{h}\right)^{1/2} \sigma^{1/2} \quad (15)$$

where  $\bar{v}$  is the speed of a molecule striking a nucleus,  $\eta_1$  is the number concentration of unbound molecules on the surface, and  $v_m$  is the molecular volume [Ohara and Reid, 1973]. Regardless of which kinetic prefactor is used, the relative growth rate of a crystal face growing by the 2D nucleation can be determined.

The growth rate can be obtained by considering a defectless crystal with size  $L$  [Chernov, 1984; Markov, 2003]. The frequency of 2D nucleation  $\tilde{J}$  is

$$\tilde{J} = JL^2 \quad (16)$$

For a given rate of lateral growth or the rate of the step advance  $v$ , the time for complete coverage of the face by one monolayer  $T$  is

$$T = \frac{L}{v} \quad (17)$$

where  $v$  is considered as an isotropic spreading velocity over the face. Inversely, the size of the nucleus  $l$  is related to the step velocity and the nucleation frequency as

$$l \cong \frac{v}{\tilde{f}} \quad (18)$$

Then by replacing  $l$  in  $\tilde{f} = Jl^2$ , the nucleation frequency in terms of the nucleation rate and step velocity is expressed as

$$\tilde{f} \cong (Jv^2)^{1/3} \quad (19)$$

The rate of growth by the 2D nucleation normal to the face is proportional to the nucleation frequency and the height as

$$R = \tilde{f}h \cong h(Jv^2)^{1/3} \quad (20)$$

where  $h$  is the height of the nucleus. Using the nucleation rate  $J$  from above, the rate is expressed as

$$R \cong h \left( \kappa_{2D} \exp\left(-\frac{\Delta G_c}{k_B T}\right) v^2 \right)^{1/3} \quad (21)$$

The kinetic prefactor and step velocity scale with the supersaturation as  $\kappa_{2D} \propto \sigma^{1/2}$  and  $v \propto \sigma$ , resulting in the supersaturation dependence of

$$R = \beta \sigma^{5/6} \exp\left(-\frac{\Delta G_c}{3k_B T}\right) \propto \sigma^{5/6} \exp\left(-\frac{F}{\sigma}\right) \quad (22)$$

where  $\beta$  is a kinetic coefficient and  $F$  is defined as

$$F \equiv \frac{1}{12} \left( \frac{c_n \phi_e}{k_B T} \right)^2 \quad (23)$$

where  $c_n$  is the shape factor and  $\phi_e$  is the effective edge energy

$$\phi_e = \frac{\sum_{i=1}^N n_i \phi_i^{edge}}{\sum_{i=1}^N n_i} \quad (24)$$

where  $n_i$  is the number of molecules located at the perimeter of the nucleus along edge  $i$  and  $N$  is the number of edges on the nucleus [Lovette and Doherty, 2012].

## 2.2. Morphology Prediction Models

### 2.1.4. Equilibrium Morphology of Crystals

Consider a curved surface ABCD and its displacement A'B'C'D' in Figure 2-6. The work required to increase the area of the surface by increasing the perpendicular arc lengths  $x$  and  $y$  to  $x + dx$  and  $y + dy$  must be accompanied by a pressure difference  $\Delta p$  across the element of the surface area defined as

$$\Delta p = p_i - p_o \quad (25)$$

The increased area is given by

$$dA = (x + dx)(y + dy) - xy \approx xdy + ydx \quad (26)$$

The increase in free energy is given by

$$dG = \gamma dA = \gamma(xdy + ydx) \quad (27)$$

where  $\gamma$  is the surface tension of the liquid. If the pressure-volume work is responsible for the expansion, the work required  $dw$  is given by

$$dw = \Delta p dV = \Delta p x y dz \quad (28)$$

Then, the equality between the free energy change and the required pressure-volume work leads to

$$\gamma(xdy + ydx) = \Delta p x y dz \quad (29)$$

Using the relation between arch length  $x$ , radii of curvature  $R_1$ , and angle  $\theta_1$ ,

$$x = R_1 \theta_1 \quad (30)$$

$$x + dx = (R_1 + dz) \theta_1$$

a proportionality is obtained as

$$\frac{x + dx}{R_1 + dz} = \frac{x}{R_1} \quad (31)$$

which simplifies to

$$\frac{dx}{x dz} = \frac{1}{R_1} \quad (32)$$

and using similar treatment for  $y$ ,

$$\frac{dy}{y dz} = \frac{1}{R_2} \quad (33)$$

Substituting Equation (32) and (33) into Equation (29) results in the Young-Laplace equation which describes the pressure difference across a curved interface

$$\Delta p = \gamma \left( \frac{1}{R_1} + \frac{1}{R_2} \right) \quad (34)$$

For a spherical liquid droplet with radius  $r$  in mechanical equilibrium with the surrounding vapor, the above equation simplifies to

$$\Delta p = p_l - p_v = \frac{2\gamma}{r} \quad (35)$$

where  $p_l$  is the liquid droplet inner pressure and  $p_v$  is the vapor pressure. The same result for the spherical interface can also be obtained from the Maxwell relation [Hiemenz and Rajagopalan, 1997]. Treating  $dG$  as an exact differential and including the surface term  $dA$ ,  $dG$  is given by two expressions

$$dG = V dp - S dT + \gamma dA \quad (36)$$

$$dG = \left( \frac{\partial G}{\partial p} \right)_{T,A} dp + \left( \frac{\partial G}{\partial T} \right)_{A,p} dT + \left( \frac{\partial G}{\partial p} \right)_{p,T} dA \quad (37)$$

At constant temperature, above relations simplify to

$$dG = V dp + \gamma dA \quad (38)$$

$$dG = \left( \frac{\partial G}{\partial p} \right)_A dp + \left( \frac{\partial G}{\partial p} \right)_T dA \quad (39)$$

The symmetry of second derivatives require

$$\left( \frac{\partial V}{\partial A} \right)_p = \left( \frac{\partial \gamma}{\partial p} \right)_A \quad (40)$$

Assuming a sphere of radius  $r$  with  $V = 4/3\pi r^3$  and  $A = 4\pi r^2$ , Equation (40) results in

$$dp = \frac{2}{r} d\gamma \quad (41)$$

For the same system at constant pressure  $p$  and temperature  $T$ , the Gibbs free energy is given by

$$dG = \mu_v dn_v + \mu_l dn_l + \gamma dA \quad (42)$$

where  $\mu_v$  and  $\mu_l$  are the chemical potentials of the vapor and liquid phases, respectively, and  $n_v$  and  $n_l$  are the number of moles in the respective phases. Since the system is closed,

$$dn_v + dn_l = 0 \quad (43)$$

At equilibrium,  $dG = 0$ , results in

$$\mu_v - \mu_l = \frac{\gamma dA}{dn_l} \quad (44)$$

Since the system consists of the liquid droplet in vapor,

$$n_l = \frac{4\pi r^3}{3} v_l \quad (45)$$

$$\mu_v - \mu_l = \frac{2\gamma v_l}{r} \quad (46)$$

where  $v_l$  is the molar volume of the liquid phase. By treating the vapor as an ideal gas, the difference in the chemical potential is related to the vapor pressure as

$$\Delta\mu = \mu_v - \mu_l = k_B T \ln \frac{p}{p_0} \quad (47)$$

where  $p_0$  is the equilibrium vapor pressure of the liquid phase. Combining Equation (46) and (47) results in the Gibbs-Thomson equation (or also called Ostwald-Freundlich equation) which describes the vapor pressure at a curved interface

$$\ln\left(\frac{p(r)}{p_\infty}\right) = \frac{2\gamma v_l}{rk_B T} \quad (48)$$

where  $p(r)$  is the vapor pressure at a curved interface of radius  $r$  and  $p_\infty$  is the vapor pressure at a flat interface ( $r = \infty$ ). If applied to solid-liquid systems, they can be expressed as

$$\ln\left(\frac{c(r)}{c^*}\right) = \frac{2\gamma M}{rk_B T \rho} \quad (49)$$

where  $c(r)$  is the solubility of particles of radius  $r$ ,  $c^*$  is the normal equilibrium solubility of the substance,  $M$  is the molar mass,  $\rho$  is the density of the solid, and  $\gamma$  is the interfacial tension of the solid in contact with the solution [Mullin, 2001].

For a crystal in a medium such as vapor, solution, or melt, the equilibrium shape is obtained at the idealized condition of infinitesimal supersaturation and infinite time. First suggested by Gibbs [Gibbs, 1878], Wulff developed the geometrical interpretation for the equilibrium morphology. This Wulff construction [Wulff, 1901; Herring, 1951] is obtained by minimizing the surface free energy term in the Gibbs-Thompson equation for a fixed crystal volume by

$$\sum_i \gamma_i A_i = 0 \quad (50)$$

which results in the following expression in terms of the distances of the faces from the origin  $H_i$  as

$$\frac{\gamma_1}{H_1} = \frac{\gamma_2}{H_2} = \dots = \frac{\gamma_i}{H_i} \quad (51)$$

This expression states that the distance of a face from the origin is proportional to the specific surface free energy of the face in the equilibrium shape. On the other hand, the actual growth shapes which are determined by the kinetics factor, are obtained by the Frank-Chernov condition [Frank, 1958; Chernov; 1963]

$$\frac{G_1}{H_1} = \frac{G_2}{H_2} = \dots = \frac{G_i}{H_i} \quad (52)$$

where  $G_i$  is the growth rate of the face and can be replaced by the relative growth rates  $R_i^{rel}$ .

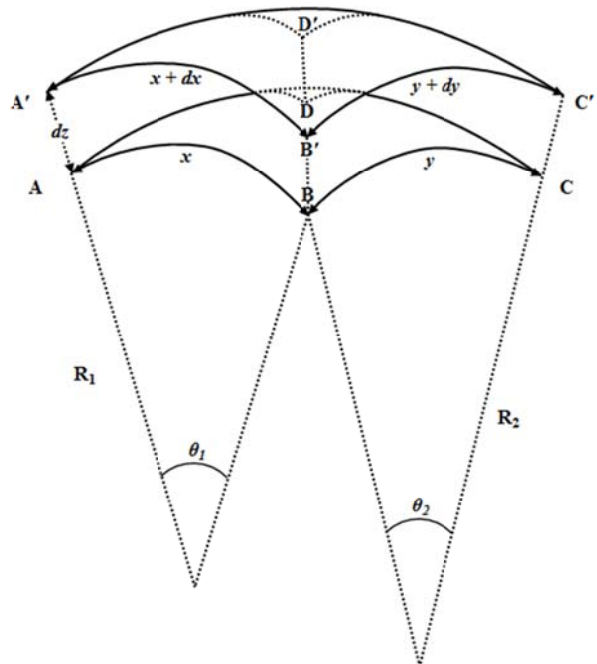


Figure 2-6. A curved surface ABCD and its displacement A'B'C'D'

### 2.1.5. Bravais-Friedel-Donnay-Harker (BFDH) Model

The earliest attempt to describe the morphology from internal habit-controlling factors such as the crystal structure was suggested by Bravais who discovered that the faces that are easiest to cleave are the slowest growing faces [Bravais, 1866]. These faces have strong cohesive forces in the tangential direction to the plane while they have weak cohesive forces in the normal direction to the plane. These ideas have been substantiated by Friedel who provided observations [Friedel, 1907].

For the slow growing faces, having strong tangential forces is equivalent to having greater reticular densities, which is the number of lattice points or nodes per unit surface. Furthermore, the reticular density is inversely proportional to the reticular area  $A_{hkl}$ , which is the area of a net plane per node. Therefore, the relative growth rate can be expressed as,

$$R_{hkl} \propto A_{hkl} \quad (53)$$

Considering that the lattice volume per node  $V_{latt}$  is constant for any lattice,

$$V_{latt} = A_{hkl}d_{hkl} \quad (54)$$

where the interplanar distance  $d_{hkl}$  is equal to the distance between the net planes, the relative growth rate of the face can be now expressed as

$$R_{hkl} \propto \frac{1}{d_{hkl}} \quad (55)$$

Furthermore, Donnay and Harker discovered extinction conditions, which are the effective reductions in the interplanar spacing by the space group symmetry. In this case, the smallest index plane is excluded from the morphological considerations for crystal structures with screw axes, glide planes, or centering [Donnay and Harker, 1937]. The extinction conditions are correlated with the same extinction of the corresponding patterns in the x-ray diffraction of the crystals.

strong tangential force

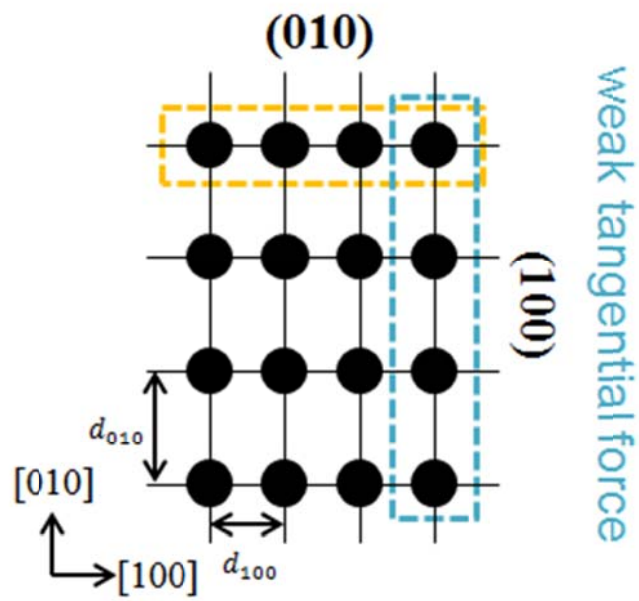


Figure 2-7. Relations of tangential force on a face and interplanar spacings.

## 2.1.6. Hartman-Perdok Approach

Two concepts have been suggested by Hartman and Perdok who have considered actual interactions rather than geometric factors as in BFDH model [Hartman and Perdok, 1955]. First of these key concepts is the periodic bond chain (PBC) theory. The PBCs are the repeated interactions called “bonds” which include all the interactions between the growth units on a crystal face. All faces can be classified according to the number of PBCs on the face as: Kinked (K) face if there is no PBC, Stepped (S) face if there is just one PBC, and Flat (F) face if there are more than two PBC parallel to the face. The K and S faces are regarded as to grow with the rough growth mechanism at any supersaturation while F faces are assumed to grow by the layered growth mechanisms. For organic molecules, the molecules within the coordination sphere are considered.

The second key concept is the attachment energy model. Based on the PBC theory, the lattice energy is defined as the total intermolecular interaction energy per mol, which is related to the sublimation enthalpy as [Gilli, 1992],

$$E^{latt} = -\Delta H^{sub} - 2RT \quad (56)$$

where the latter term is the correction for differences between the gas-phase enthalpy and the solid-state enthalpy corresponding to the translational and rotational contributions.

Lattice energy which is a constant value for a given crystal system, is divided into interactions within the slice of an interplanar distance  $E^{slice}$  called the slice energy and interactions of the molecules in the slice with the rest  $E^{att}$  called the attachment energy.

$$E^{latt} = E_{hkl}^{slice} + E_{hkl}^{att} \quad (57)$$

Considering that the bond energy is inversely proportional to the time required to form a bond, the relative growth rate is proportional to the interactions energy between a molecule on the face and those in the underlying crystal

$$R_{hkl} \propto |E_{hkl}^{att}| \quad (58)$$

The main drawback of the BFDH model and the attachment energy model is that these models only consider the geometric factors or interaction energies between the crystal molecules which solely come from the internal structure of the crystals. As a result, the external environmental factors such as the solvent interactions, temperature, supersaturations are not considered at all. This limits the reliability of these models to morphology of crystals grown from vapor where the solvent interaction is small and the growth rate is limited by diffusion. Deviations from experimental morphologies are frequent when these models are applied to crystals grown from solution.

One of the popular approaches to overcome the ignorance of the effect of solvents is the modified attachment energy model. Although variations exist, a common approach of these models is to calculate the interaction energy of adsorbed solvent molecules on the specific crystal faces [Duan et al., 2010]. From the energy of the crystal surface  $E_{surf}$ , the energy of the solvent layer  $E_{solv}$ , and the total energy  $E_{total}$ , the interaction energy is evaluated as

$$E_{int} = E_{total} - E_{surf} - E_{solv} \quad (59)$$

This value is converted to the correction term  $E_s$  by accounting for the surface area of the system  $A_{model}$  and the accessible solvent surface of the crystal face  $A_{acc}$  using

$$E_s = \frac{E_{int}A_{acc}}{A_{model}} \quad (60)$$

Then, the modified attachment energy which accounts for the effect of solvent is calculated as

$$E_{att}^s = E_{att} - E_s \quad (61)$$

This modification could account for the solvent binding energy by reducing the apparent attachment energy for the faces with large interaction with the solvent, thereby increasing the morphological importance for these faces.

The morphology can be predicted from this modified attachment energy using the same relation of

$$R \propto E_{att}^s \quad (62)$$

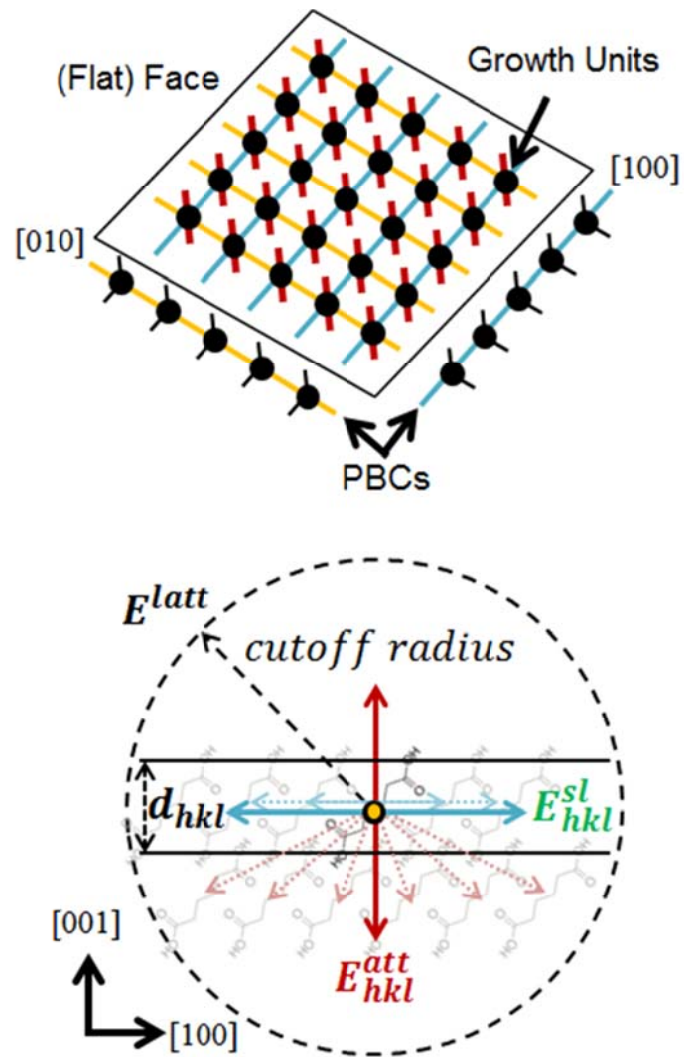


Figure 2-8. Periodic Bond Chains and Attachment Energy.

## 2.2.4. Interfacial Structure Analysis Model

The advent of mechanistic models was pioneered by Liu and Bennema, with their contribution of the interfacial structure analysis (ISA) model [Liu et al., 1995; Liu and Bennema, 1996].

Based on the spiral growth model of BCF, the growth rate of an F-face can be expressed by

$$R_{hkl}^{rel} = \frac{d_{hkl} v_{hkl}}{\lambda_{0,hkl}} \quad (63)$$

In this model, it is assumed that at some distance from the center, the spirals can be approximated with the concentric circular spiral of Cabrera and Levine for which the distance between the steps  $\lambda_{0,hkl}$  is given as [Cabrera and Levine, 1956]

$$\lambda_{0,hkl} = 19r_c = \frac{19\gamma_{hkl}^{step} V_m}{\Delta\mu} = \frac{19a_e \bar{\phi}_{hkl}^{step}}{\Delta\mu} \quad (64)$$

where  $a_e$  is the average edge length,  $\Delta\mu$  is the supersaturation defined as the difference in the chemical potentials of the crystal phase and the solution phase,  $\gamma_{hkl}^{step}$  is the average step energy per growth unit on the face ( $hkl$ ) per area,  $V_m$  is the molecular volume, and  $\bar{\phi}_{hkl}^{step}$  is the average step energy on the face ( $hkl$ ). In the original BCF theory, the Archimedean spiral is assumed with

$$\lambda_{0,hkl} = 4\pi r_c \quad (65)$$

instead of the 19 above.

For organic molecular crystals grown from solutions, kink incorporation is considered as the rate limiting step. Although surface diffusion could be critical for some cases, all growth units are assumed to arrive at the kink by isotropic bulk diffusion. In this case, the step velocity  $v_{hkl}$  at a given supersaturation  $\Delta\mu$  and temperature  $T$  is proportional to the propagation distance perpendicular to the edge direction  $a_p$ , the concentration of the adsorbed growth units around the kinks  $X_{A(hkl)}$ , the kink density  $\rho_{hkl}^{kink}$ , and a Boltzmann factor related to incorporation barrier. In the ISA model, the incorporation barrier factor is assumed as

$$\exp\left(-\frac{\Delta G_{hkl}^\ddagger}{k_B T}\right) \approx \frac{X_{A(hkl)}^{eff}}{X_{A(hkl)}} \exp\left(-\frac{\Delta G_{desolv}^*}{k_B T}\right) \quad (66)$$

where  $X_{A(hkl)}^{eff}$  is the concentration of the effective growth units which are the adsorbed solute molecules in the interface layer that have the proper orientation and conformation for incorporation into kinks. The contribution of the activation free energy for incorporation into kinks,  $\Delta G_{hkl}^\ddagger$  is divided into two parts. The concept of pre-ordered growth units in the interface layer with crystal-like orientation and conformation is reflected as a probability  $X_{A(hkl)}^{eff}/X_{A(hkl)}$ . The rest of the term is a Boltzmann factor related to the activation energy for desolvation of the growth units. For the case where the interactions between the units of solid and solvent at the interface are weak, this barrier is assumed to be isotropic with the value of  $k_B T$ , or comparable to the thermal fluctuations. The resulting proportionality of the step velocity is

$$v_{hkl} \propto a_p X_{A(hkl)}^{eff} \rho_{hkl}^{kink} \quad (67)$$

The kink density, the probability of encountering a kink site on an edge, can be approximated for centrosymmetric growth units by the approach of Frenkel [Frenkel, 1945]. The partition functions for the negative kink, the positive kink, and no kink are  $\exp(-\phi_{neg}^{kink}/k_B T)$ ,  $\exp(-\phi_{pos}^{kink}/k_B T)$ , and 1, respectively. Assuming  $\phi_{neg}^{kink} = \phi_{pos}^{kink}$ , the kink density is given as

$$\rho_{hkl}^{kink} = \left( 1 + \frac{1}{2} \exp\left(\frac{\bar{\phi}_{hkl}^{kink}}{k_B T}\right) \right)^{-1} \quad (68)$$

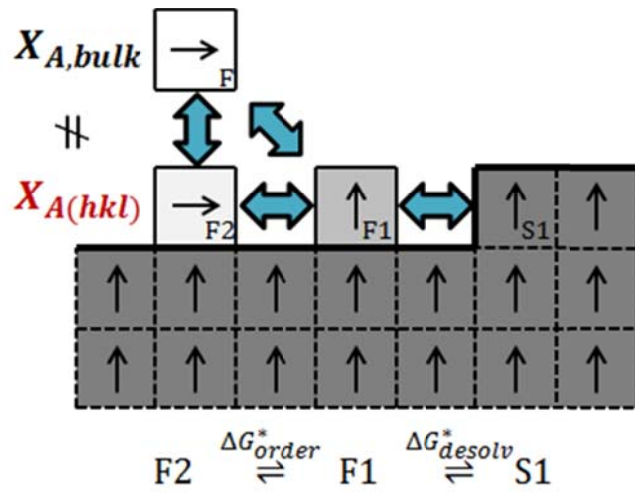
where  $\bar{\phi}_{hkl}^{kink}$  is the average kink energy on the face  $(hkl)$ , which represents the mean work or free energy change required to create a kink along an edge by the rearrangement of the structure. For the case of low energy edges, this approximation can fail and require multisite models for the kinks [Lovette, 2012]. In the original ISA model, the kink density is approximated as

$$\rho_{hkl}^{kink} \sim \exp\left(-\frac{\bar{\phi}_{hkl}^{kink}}{k_B T}\right) \quad (69)$$

The concentration of the effective growth units addresses the pre-ordering of the growth units in the fluid phase near the interface. The degree of pre-ordering can be described by the differences in the orientations and conformations of the growth units at the solid–fluid interface from the orientations and conformations in the bulk crystal. Liu and Bennema developed a model called the inhomogeneous cell model [Liu and Bennema, 1996] to treat this ordering of the fluid units. The

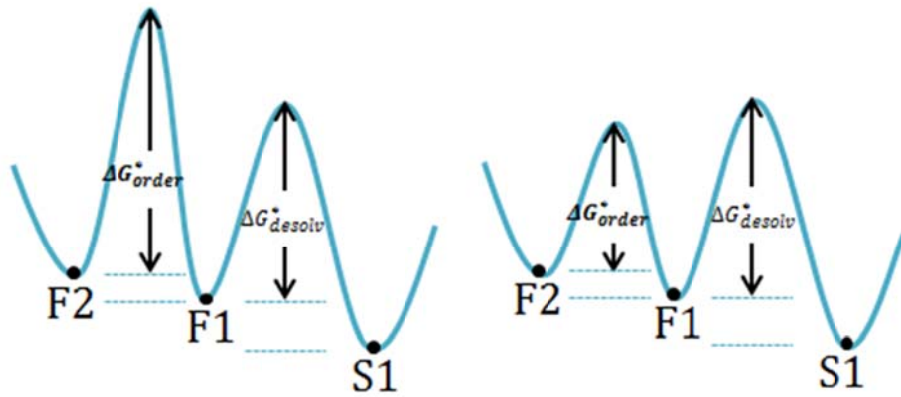
whole space parallel to the orientation of the face ( $hkl$ ) is divided into a set of layers, each with a thickness of  $d_{hkl}$ . This idea is based on the fact that the periodicity of the density oscillation in the fluid side has the same periodicity as in the solid phase. It is assumed that each layer in the fluid phase is homogeneous and all layers are in equilibrium with their adjacent layers.

To identify the adsorbed growth units, the growth units in the crystal phase are called S1 units. In the interface layer, which consists of the two adjacent layers of the first fluid layer and the first solid layer, the adsorbed growth units are classified into two types. F1-units are the adsorbed growth units that have the same orientation and conformation to the S1-units. The F2-units are all other growth units including F1-like units and not F1-like units. The F1-like units are defined below. An F2-unit has to be transformed into an F1-unit in order to enter a kink site.



(a)

$$\Delta G_{order}^* > \Delta G_{desolv}^* \quad \text{or} \quad \Delta G_{order}^* < \Delta G_{desolv}^*$$



(b)

Figure 2-9. A schematic drawing of the Interfacial Structure Analysis Model

(a) Classification of the growth units at the interface

(b) Free energy barriers between the F1 and F2 units.

Assuming that the equilibria between F2-units, F1-units, and S1-units are the only important kink incorporation steps, the transformation reaction from an F2-unit to an F1-unit and incorporation into a kink site to become a S1-unit is assumed to occur by



Here, it is assumed that the desolvation is the rate-determining step in the incorporation of an F1-unit into a kink site. Then the effectiveness factor of an F2-unit as a growth unit in terms of reaction rates or relaxation times is expressed as

$$\zeta(\tau) = \frac{R^{F2-S1}(\tau)}{R^{F1-S1}(\tau)} = \frac{1}{\frac{t_{relax}^{F2-S1}}{1}} = \frac{1}{\frac{1}{R^{F2-F1}(\tau)} + \frac{1}{R^{F1-S1}(\tau)}} \quad (71)$$

If the backward reaction is ignored, the effectiveness factor is expressed in terms of the frequency factors and free energy barriers as,

$$\zeta(\tau) \approx \frac{1}{\frac{v_1 \exp(-\Delta G_{desolv}^*/k_B T)}{1} + \frac{1}{v_2 \exp(-\Delta G^{**}/k_B T)}} \quad (72)$$

After assuming that the frequencies of thermal vibrations are equal for the F1 and F2 growth units, the effectiveness factor  $\zeta$  can be reformulated as

$$\begin{aligned} \zeta(\tau \neq F1) &\approx \frac{\exp\left(\frac{\Delta G_{desolv}^*}{k_B T}\right)}{\exp\left(\frac{\Delta G_{desolv}^*}{k_B T}\right) + \exp\left(\frac{\Delta G^{**}}{k_B T}\right)} \\ &= \frac{1}{2} \exp\left\{\frac{\Delta G_{desolv}^* - \Delta G^{**}}{2k_B T}\right\} \frac{2}{\exp\left\{\frac{\Delta G_{desolv}^* - \Delta G^{**}}{2k_B T}\right\} + \exp\left\{\frac{\Delta G^{**} - \Delta G_{desolv}^*}{2k_B T}\right\}} \\ &= \frac{1}{2} \exp\left\{\frac{[\Delta G_{desolv}^* - \Delta G^{**}(\tau)]}{2k_B T}\right\} \times \operatorname{sech}\left\{\frac{[\Delta G_{desolv}^* - \Delta G^{**}(\tau)]}{2k_B T}\right\} \end{aligned} \quad (73)$$

$$\zeta(\tau = F1) = 1 \quad (74)$$

Then the expectation value of the effectiveness factor  $\delta_{hkl}$  is

$$\delta_{hkl} = \sum_{\tau=F1,F2} [\zeta(\tau)P(\tau)] \quad (75)$$

where for the state  $\tau = F1$  or  $F2$ ,

$$P(\tau) = X_{A(hkl)}^{\tau} / X_{A(hkl)} \quad (76)$$

$$G^*(\tau) = -k_B T \ln P(\tau) + const \quad (77)$$

$$\Delta G^*(\tau) = G^*(\tau) - G^*(F1_{hkl}) \quad (78)$$

$$\Delta G^{**}(\tau) = 0 \text{ if } \Delta G^*(\tau) \leq 0 \quad (79)$$

$$\Delta G^{**}(\tau) = \Delta G^*(\tau) \text{ if } \Delta G^*(\tau) > 0 \quad (80)$$

where  $P(\tau)$  denotes the probability of an adsorbed growth unit to be in an orientational and conformational state  $\tau$ ,  $\Delta G^*(\tau)$  is the free energy barrier for the reorientation of an F2-unit into an F1-unit. The F2-units with  $\Delta G^*(\tau) \leq 0$  are called F1-like units since they are oriented differently but do not have the free energy barrier.  $\delta_{hkl}$  can be understood as the probability that an adsorbed solute molecule will obtain the required reorientation to enter a kink site.

Then the concentration of the effective growth units is

$$X_{A(hkl)}^{eff} = \zeta X_{A(hkl),F2} + X_{A(hkl),F1} = \delta_{hkl} X_{A(hkl)} \quad (81)$$

This concentration of the effective growth units is comprised of two factors, the anisotropic local concentration of the growth units at the interface  $X_{A(hkl)}$  and the average effectiveness factor  $\delta_{hkl}$  which is determined by the difference in the desolvation free energy barrier and orientational free energy barrier. In the ISA model, two collective external habit-controlling factors, the surface scaling factor  $C_{l(hkl)}^*$  and the molecular orientational factor  $t_{hkl}$  are defined as

$$C_{l(hkl)}^* = \frac{\Delta H_{hkl}^{diss}}{\Delta H^{diss}} = \frac{\ln X_{A(hkl)}^{eff}}{\ln X_A} \quad (82)$$

$$t_{hkl} = -\ln \left[ \frac{X_{A(hkl)}^{eff}}{X_{A(hkl)}} \right] \quad (83)$$

The surface scaling factor derives from the van't Hoff equation with the local dissolution enthalpy at the crystal surface  $\Delta H_{hkl}^{diss}$ , which typically differs from the bulk dissolution enthalpy  $\Delta H^{diss}$  because of the ordering of the fluid molecules and the crystal relaxation near the surface. In principles,  $C_{l(hkl)}^*$  values can also be obtained from roughening transition experiments or consistent-field lattice model calculations.

In order to calculate the relative growth rates from the above two collective external habit-controlling factors, energy terms which are the average step energy  $\bar{\phi}_{hkl}^{step}$  and the average kink energy  $\bar{\phi}_{hkl}^{kink}$  are needed. They can have the same value if a square nucleus or a circular nucleus is assumed. Between the two of them, the step energy  $\bar{\phi}_{hkl}^{step}$  is related to the bond energies from PBC analysis and local dissolution enthalpy from interfacial structure analysis through the Ising models (one of which is the inhomogeneous cell model) of the crystal-solution interface. The exchange bond energy between the nearby solid and fluid cells in the  $i$ -direction at the interface has the form of

$$\phi_i = \phi_i^{sf} - \frac{1}{2}(\phi_i^{ss} + \phi_i^{ff}) \quad (84)$$

where  $\phi_i^{sf}$ ,  $\phi_i^{ss}$ ,  $\phi_i^{ff}$  are interaction bond energies per mole of bond between nearby solid-fluid, solid-solid, and fluid-fluid cells. This exchange bond energy is equal to the work required to form one solid-fluid contact in the  $i$ -direction. In order to relate the bond energies to the experimental observables, an approximation called the proportionality condition is assumed that can be stated as,

$$\phi_1 : \phi_2 : \dots : \phi_m = \Phi_1^{ss} : \Phi_2^{ss} : \dots : \Phi_m^{ss} \quad (85)$$

where  $\Phi_i^{ss}$  is the exchange bond energy between solid-solid cells in the  $i$ -direction in the bulk solid. Then experimentally observables are related to the bond energies as,

$$\sum_i^m \Phi_i^{ss} = 2E_{latt} \quad (86)$$

$$\sum_i^{n_{hkl}} \Phi_i^{ss} = 2E_{hkl}^{slice} \quad (87)$$

$$\xi_{hkl} = \frac{E_{hkl}^{slice}}{E_{latt}} \quad (88)$$

$$\sum_i^m \phi_i = 2\Delta H_{hkl}^{diss} \quad (89)$$

where  $n_{hkl}$  is the coordination number from the PBC analysis. The factor of 2 is for the conversion from the exchange bond energy per bond to energy per growth unit. From the assumed proportionality condition, the exchange bond energies  $\phi_i$  and the average step energy  $\bar{\phi}_{hkl}^{step}$  can be obtained as

$$\phi_i = \left( \frac{\Phi_i^{ss}}{\sum_i^m \Phi_i^{ss}} \right) \sum_i^m \phi_i = \left( \frac{\Phi_i^{ss}}{2E_{latt}} \right) 2\Delta H_{hkl}^{diss} \quad (90)$$

$$\begin{aligned} \bar{\phi}_{hkl}^{step} &= \left( \sum_i^{n_{hkl}} \phi_i \right) / 2n_{hkl} = \left( \left( \frac{\sum_i^{n_{hkl}} \Phi_i^{ss}}{2E_{latt}} \right) 2\Delta H_{hkl}^{diss} \right) / 2n_{hkl} \\ &= \xi_{hkl} C_{l(hkl)}^* \Delta H^{diss} / n_{hkl} \end{aligned} \quad (91)$$

Then, the relative growth rate can be calculated by collecting the anisotropic factors as

$$R_{hkl}^{rel} \propto \frac{n_{hkl} d_{hkl}}{C_{l(hkl)}^* \xi_{hkl}} X_A^{C_{l(hkl)}^*} \exp\left(-\frac{C_{l(hkl)}^* \xi_{hkl} \Delta H^{diss}}{n_{hkl} k_B T}\right) \quad (92)$$

The internal factors  $d_{hkl}$ ,  $n_{hkl}$ ,  $\xi_{hkl}$  are determined from the PBC analysis whereas the external factor  $C_{l(hkl)}^*$  in terms of  $X_{A(hkl)}$  and  $\delta_{hkl}$ , are computed from MD simulations. Experimental value of the enthalpy of dissolution  $\Delta H^{diss}$  is also required.

### 2.3. Centrosymmetric and Non-Centrosymmetric Growth Units

Growth units can be comprised of a single molecule or dimer, etc. The center of mass and the inversion center of centrosymmetric growth units are the same. In this case, all kink sites for a single direction along an edge as well as for all edges on a face are equivalent because the bonds exposed at any kink sites are the same. Furthermore, there is just one type of kink site over the whole lattice since the bonds exposed at the kink site is also irrespective of the face. This is called Kossel-like. On the other hand, non-centrosymmetric growth units expose various bonds depending on the kink sites which are anisotropic for different edges [Kuvadiah and Doherty, 2011]. Therefore, kink density and kink rate that can consider this anisotropy is required for crystals composed of non-centrosymmetric growth units.

For example, assume that a non-centrosymmetric molecule has two different growth units  $A$  and  $B$  on an edge with different symmetry or orientation. Then the two different bonds with bond energies  $E_1$  and  $E_2$ , that alternate along the edge provide four different types of kink sites. All possible ways of rearrangements are I:  $(1,1 \rightarrow 1,1)$ , II:  $(1,1 \rightarrow 2,2)$ , III:  $(2,2 \rightarrow 1,1)$ , IV:  $(2,2 \rightarrow 2,2)$ . The energy expense per kink of these rearrangements are  $\varepsilon_I = (E_1 + E_1)/4$ ,  $\varepsilon_{II} = (E_1 + E_2)/4$ ,  $\varepsilon_{III} = (E_2 + E_1)/4$ , and  $\varepsilon_{IV} = (E_2 + E_2)/4$ , respectively. Then the overall kink density on edge  $i$  is given by summing the individual probability of formation for the four types of kink sites as

$$\rho_i = \frac{\exp\left(-\frac{\varepsilon_I}{k_B T}\right) + \exp\left(-\frac{\varepsilon_{II}}{k_B T}\right) + \exp\left(-\frac{\varepsilon_{III}}{k_B T}\right) + \exp\left(-\frac{\varepsilon_{IV}}{k_B T}\right)}{1 + \exp\left(-\frac{\varepsilon_I}{k_B T}\right) + \exp\left(-\frac{\varepsilon_{II}}{k_B T}\right) + \exp\left(-\frac{\varepsilon_{III}}{k_B T}\right) + \exp\left(-\frac{\varepsilon_{IV}}{k_B T}\right)} \quad (93)$$

The  $k$ th kink rate on edge  $i$  is also defined as

$$u_{i,k} = j^+ P_k - j_{k+1}^- P_{k+1} \quad (94)$$

$$P_{k+2} = \left(\frac{j^+ + j_{k+1}^-}{j_{k+2}^-}\right) P_{k+1} - \left(\frac{j^+}{j_{k+2}^-}\right) P_k \quad (95)$$

where  $j^+$  is the attachment rate of growth units into kink sites and  $j_k^-$  is the detachment rate of growth units from kink site  $k$ ,  $P_k$  is the probability of kink site being type  $k$  where  $\sum_{k=1}^n P_k$  and  $n$  is the number of types of kink sites. The overall kink rate on edge  $i$ ,  $u_i$  defined as the number of molecules added per unit time has the relationship [Shim et al., 2016]

$$u_{i,1} = \dots = u_{i,n} = u_i/n \quad (96)$$

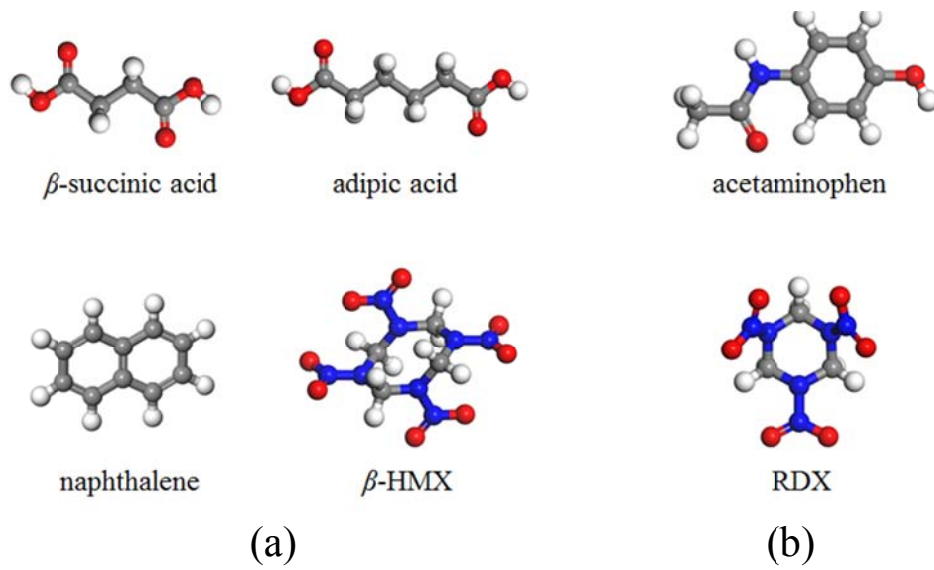


**Figure 2-10. Typical molecules whose crystals are comprised of (a) Centrosymmetric growth units (b) Non-centrosymmetric growth units.**

## Chapter 3. Materials

### 3.1. Adipic Acid

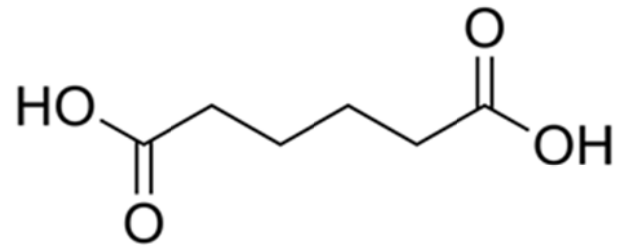
#### 3.1.1. Motivations for Predicting the Adipic Acid Morphology

Adipic acid ( $C_6H_{10}O_4$ , hexanedioic acid) is mainly used as a precursor to nylon-66. During the production process, crude adipic acid product is removed from nitric acid liquor by crystallization as a colorless and odorless crystal to remove byproducts such as succinic acid and glutaric acid. These impurities are readily incorporated into (100) face which will enlarge this specific face and reduce the flowability of the slurry [Klug and Van Mil, 1994; Clydesdale et al., 2005].

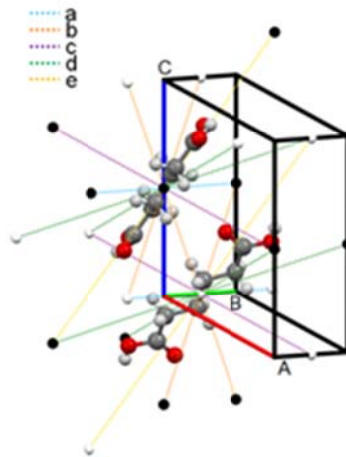
#### 3.1.2. Previous Studies on the Morphology of Adipic Acid

Various experimental studies indicated that the adipic acid crystal grown from aqueous solution has the morphology of hexagonal plate with the dominant (100) face. Some deviations are observed however, that the morphology reported by Davey et al., and Winn and Doherty showed crystal with 5 faces [Davey et al., 1992; Winn and Doherty, 2000] whereas those reported by others showed crystal with 3 faces [Michaels and Colville, 1959; Michaels and Tausch, 1961; Fairbrother and Grant, 1978; Chow et al, 1984; Davey et al., 1992; Klug and Van Mil, 1994; Pfefer and Boistelle, 2000; Keel et al., 2004]

BFDH model and attachment energy model have been applied for the prediction of adipic acid morphology grown from aqueous solution. As expected, deviation from the experimental morphology is observed for these methods [Myerson and Jang, 1995; Clydesdale et al., 2005; Pfefer and Boistelle, 2000]. Chan and others used a modified attachment energy model to account for the effects of external environments which considered the solvent interactions using coupled scene of MD and Monte Carlo [Chan et al., 2015]. Doherty and coworkers developed their spiral growth model that have evolved in time to accommodate many important concepts in crystal growth, and applied those models to adipic acid crystals in a number of papers [Winn and Doherty, 1998; Winn and Doherty, 2000; Tilbury et al., 2016].



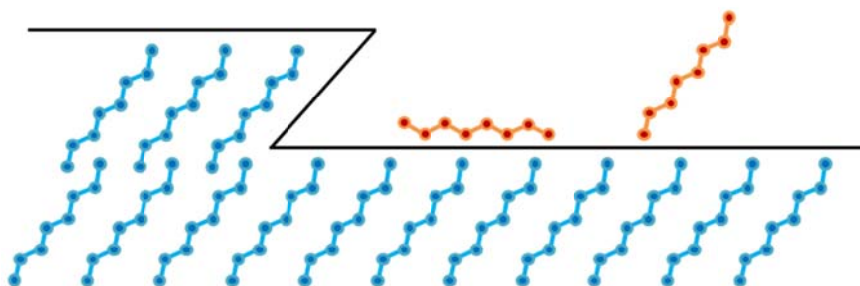
(a)



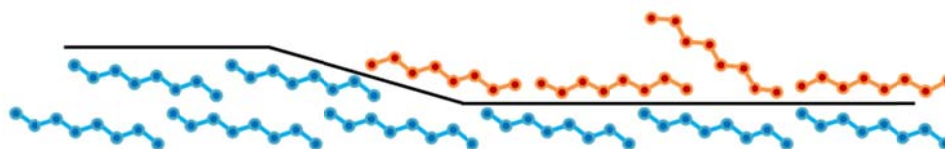
(b)

Figure 3-1. (a) Molecular structure and (b) Crystal structure of adipic acid.

**LOW** concentration at the interface AND/OR **HIGH** orientational barrier



**HIGH** concentration at the interface AND/OR **LOW** orientational barrier



**Figure 3-2. Schematic drawing of the interface of adipic acid crystal.**

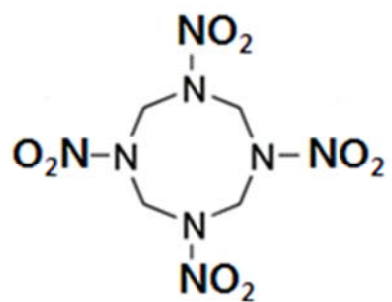
## 3.2. HMX

### 3.2.1. Motivations for Predicting the HMX Morphology

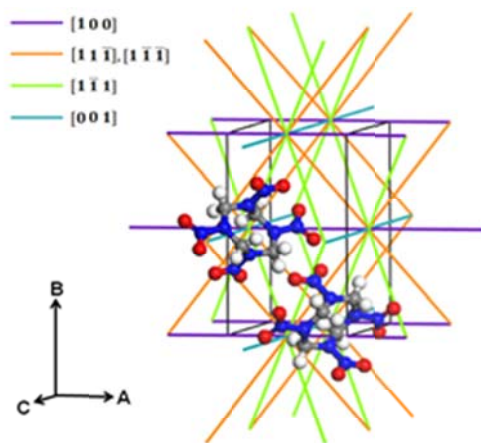
HMX, abbreviated for High Melting eXplosive ( $C_4H_8N_8O_8$ , cyclotetramethylenetetranitramine, octahydro-1,3,5,7-tetranitro-1,3,5,7-tetrazocine), belongs to the nitramine group which are the most common organic high explosives. Compared to the other widely used explosives such as TNT (trinitrotoluene), these molecules have higher densities which provide greater detonation properties while they also have higher sensitivities toward external stimuli resulting in higher likelihood of accidental ignitions. One factor that greatly affects these properties is the polymorph. Among the four known polymorphs, the  $\beta$  form is the most preferred one because of its high density and low friction/impact/shock sensitivities [Bernstein, 2002; Zhu et al, 2007]. Another factor that affects the sensitivities is the crystal morphology. The sensitivities are found to depend largely on the direction of the applied stress relative to the crystallographic orientations [Zamiri and De, 2011], and therefore on the relative areas of different faces [Song et al, 2008] which encourage a thorough understanding of its growth morphology.

### 3.2.2. Previous Studies on the Morphology of HMX

Several modified attachment model have been applied for [Duan et al, 2010; Zhang et al, 2013]. They are characterized by bulky crystal morphology with large (020) or (011) faces. On the other hand, remarkable agreements to the elongated crystal morphology have been achieved recently by the spiral growth model of Doherty [Shim and Koo, 2015; Tilbury and Doherty, 2017]. Further contribution is credited to Shim and Koo who applied the Lovette-Doherty method and kinetic Monte Carlo (KMC) method to compute crystal morphologies at varying supersaturations including the concept of transition of the dominant growth mechanism. It was shown that the growth in [100] direction is facilitated with two-dimensional nucleation resulting in elongated crystals obtained at higher supersaturations [Shim and Koo, 2015].



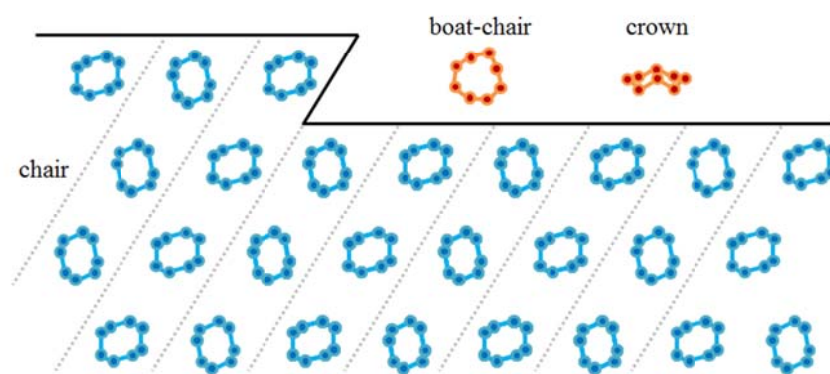
(a)



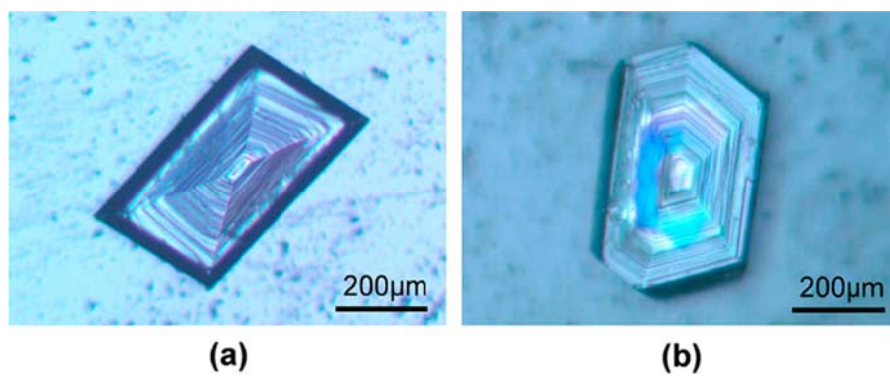
(b)

Figure 3-3. (a) Molecular structure and (b) Crystal structure of  $\beta$ -HMX.

**HIGH** conformational barrier



**Figure 3-4. Schematic drawing of the interface of  $\beta$ -HMX crystal.**



**Figure 3-5. Optical observation of spirals for the (a) (020) and (b) (011) faces of  $\beta$ -HMX crystals obtained by slow evaporation [Shim and Koo , 2015].**

## Chapter 4. Computational Methods

### 4.1. Computational Methods Used for Adipic Acid Crystals

#### 4.1.1. Periodic Bond Chain Analysis

Crystal structure of adipic acid by Hwang and Sagadevan (CCDC 1025098) was used. Compared to the earlier reported structure of Housty and Hospital (CCDC 1101301), (002), (011), (11 $\bar{1}$ ), ( $\bar{1}$ 02), and (20 $\bar{2}$ ) faces are newly indexed as (20 $\bar{2}$ ), (1 $\bar{1}\bar{1}$ ), (0 $\bar{1}$ 1), (10 $\bar{2}$ ), and (002) faces, respectively. Adipic acid crystallizes in a monoclinic structure with the space group P2 $_1$ /c with  $Z = 2$  per unit cell. The extinction conditions for the space group are  $h0l:l = 2n, 0k0:k = 2n, hkl:k + 1 = 2$ . The unit cell parameters are  $a = 7.1627 \text{ \AA}$ ,  $b = 5.1358 \text{ \AA}$ ,  $c = 9.9772 \text{ \AA}$ ,  $\beta = 110.810^\circ$ .

For the calculation of the internal habit controlling parameters, general AMBER force field was used for the calculation of intermolecular interactions. Atomic partial charge set was obtained by Mulliken population analysis [Owens and Wendt, 1969] on the adipic acid molecule whose geometry has been optimized by PM6 semiempirical method [Stewart, 2007]. The estimated lattice energy using this combination of force field and atomic partial charge set is -30.5 kcal/mol whereas the estimated value from experiment is -29.9 kcal/mol using the value of enthalpy of sublimation calculated by Bruns and coworkers [Bruns et al., 2012].

The comparison of the resulting morphologies obtained by BFDH model and AE model with different crystal structure, force field, and charge sets is shown in Figure 4-3. The conditions are:

For BFDH model,

- (a) Housty and Hospital structure
- (b) Hwang and Sagadevan structure

For AE model,

- (c) Housty and Hospital structure, force field and charge set by Lifson et al.
- (d) Hwang and Sagadevan structure, force field and charge set by Lifson et al.
- (e) Housty and Hospital structure, GAFF force field, and PM6 charge set
- (f) Hwang and Sagadevan structure, GAFF force field, and PM6 charge set.

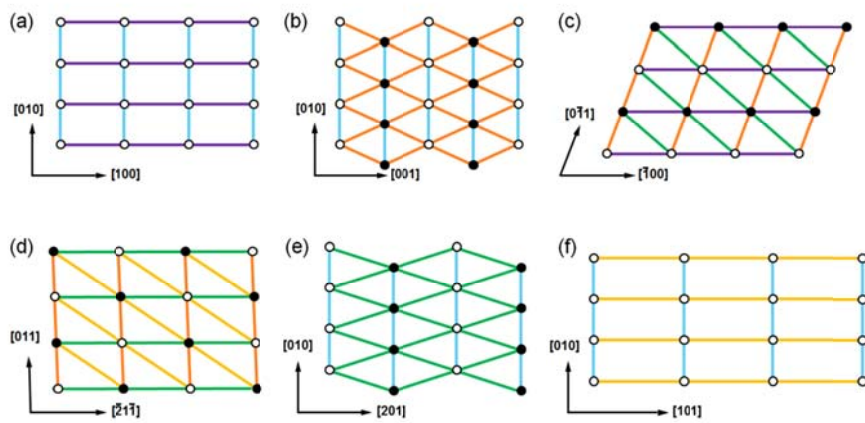


**Figure 4-1. Bonding structures for the (a) (002), (b) (100), (c) (011), (d)  $(11\bar{1})$ , (e)  $(10\bar{2})$ , and (f)  $(20\bar{2})$  faces of adipic acid crystal.**

**Table 4-1 Interplanar distances and attachment energies for the F-faces of adipic acid**

Layer Miller Index	$d_{hkl}$ [Å]	$E_{hkl}^{att}$ [kcal/mol]
(002)	4.663	-29.13
(100)	6.695	-16.20
(011)	4.499	-20.58
(11 $\bar{1}$ )	4.071	-13.41
(10 $\bar{2}$ )	4.686	-22.70
(20 $\bar{2}$ )	3.339	-21.14

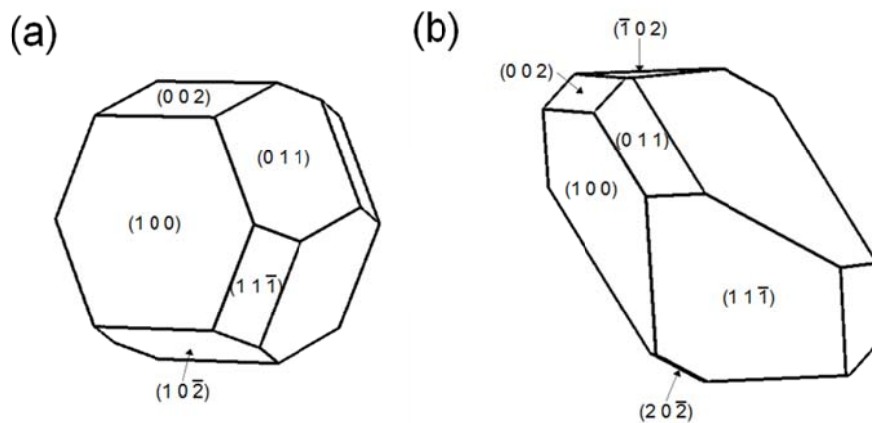


**Figure 4-2. Growth morphology of adipic acid crystal predicted by (a) BFDH model (b) AE model.**

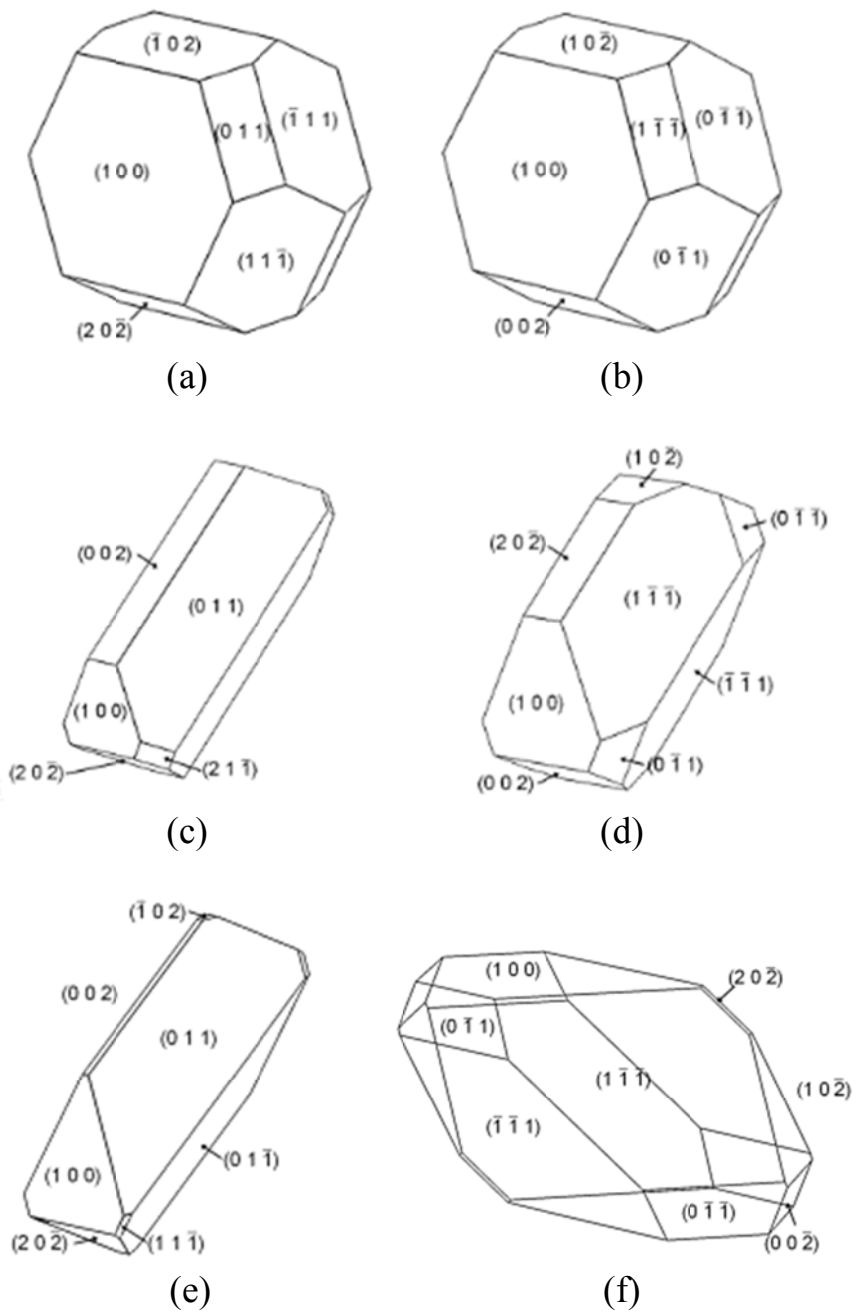


Figure 4-3. Growth morphology of adipic acid crystal predicted by different crystal structures, force fields, and charge sets.

**Table 4-2. Atomic partial charges of the adipic acid molecule.**

Atom	Partial charge
H19	0.374
O6	-0.590
C1	0.680
O7	-0.531
C2	-0.494
H11	0.242
H12	0.242
C3	-0.313
H13	0.195
H14	0.195
C4	-0.313
H15	0.195
H16	0.195
C5	-0.494
H17	0.242
H18	0.242
C8	0.680
O10	-0.531
O9	-0.590
H20	0.374

### 4.1.2. Modified Attachment Energy Model

The modified attachment energy model accounts for the solvents effects using the solvent accessible area and the interaction energy between the solvent molecules and crystalline molecules. The results from this approach are presented in Table 4-3 and Table 4-4.  $S$  in Table 4-4 is the accessible solvent surface of unit area. Snapshots of the solvent accessible areas of (002), (100), and (011) faces are shown in Figure 4-6. The double cubic lattice method [Eisenhaber et al., 1994] has been used for calculation of the Connolly surface. [Connolly, 1983]

It is noticeable that the interaction energy for the  $(20\bar{2})$  face is lower while that for others are similar. Since the only external factor considered in this model is the interaction energy, this leads to overall similar trends with the previous attachment energy model calculations except for the  $(20\bar{2})$  face which will have higher growth rate. Therefore, the resulting morphology from this model still does not coincide with the experimental descriptions. This is expected since this model does not consider any other external factors such as the growth mechanism, supersaturation, etc. This result shows that in order to accurately account for the external environments, considering the interaction energy is not enough, which led to development of other mechanistic models.

**Table 4-3. Interaction energies for the F-faces of the adipic acid crystal.**

Layer Miller Index	$E_{tot}$	$E_{surf}$	$E_{solv}$	$E_{int}$
(002)	-1341	-7239	-1025	6924
(100)	-1265	-7557	-1058	7350
(011)	-1231	-7527	-1040	7335
(11 $\bar{1}$ )	-1131	-7734	-1002	7605
(10 $\bar{2}$ )	-1333	-7487	-1016	7169
(20 $\bar{2}$ )	-1198	-3787	-1061	3650

**Table 4-4. Modified attachment energies and relative growth rates for the F-faces of the adipic acid crystal.**

Layer Miller Index	$S$	$E_{att}^s$	$R_{hkl}$
(002)	1.453	-31.39	0.4868
(100)	2.219	-64.49	1.0000
(011)	1.579	-37.46	0.5808
(11 $\bar{1}$ )	1.218	-25.62	0.3973
(10 $\bar{2}$ )	1.429	-38.24	0.5930
(20 $\bar{2}$ )	1.179	-30.45	0.4721

### 4.1.3. Interfacial Structure Analysis

All initial surfaces were cleaved from the unit cell using Materials Studio (version 7.0) and reoriented in the z-direction in the simulations. All MD simulations were performed using Gromacs (version 4.6.5). The initial aqueous solution was prepared by inserting adipic acid and water molecules at random positions with the mole fraction of 0.00628 (96 adipic acid molecules and 15200 water molecules), which is near the saturation concentration (mole fraction of 0.00627) at 313.15 K [Gaivoronskii and Granzhan, 2005], using the genbox (previous version of insert-molecules) package of Gromacs. After insertion, energy minimization with the steepest descent method, and equilibration at 1.013 bar and 700 K for 1 ns by NPT (isothermal–isobaric) simulation to remove spurious structures were carried out. The desired saturated solution was obtained by NPT simulation at 1.013 bar and 313.15 K for 2 ns.

The saturated solution was then brought into contact with the cleaved surfaces at the upper and lower regions in the z direction. The constructed system underwent a series of steps for an equilibrium run. First, an energy minimization of the system was carried out. Second, an NVT (isothermal-isochoric) equilibration was carried out at 313.15 K, with the “freeze group” option on the crystal molecules, for 100 ps. Lastly, an NPT equilibration of the solution was carried out at 313.15 K, using a pressure of 1.013 bar for 2 ns with anisotropic pressure coupling in the z direction and positional restraints on the crystal molecules. After these system preparations, the system was cooled by an NPT production run at 307 K for 50 ns, with otherwise the same condition with the NPT equilibration run.

Temperature coupling was achieved by the Bussi-Donadio-Parrinello thermostat [Bussi et al., 2007] for all simulations. Semi-isotropic pressure coupling was achieved by a Berendsen barostat [Berendsen et al., 1984] followed by a Parrinello–Rahman barostat [Parrinello and Rahman, 1981; Nosé and Klein, 1983] for the NPT simulations. The generalized AMBER force field [Cornell et al, 1995; Wang et al, 2004] was used for the intra- and intermolecular interactions of adipic acid. SPC/E model was used for water. The Particle Mesh Ewald (PME) method [Darden et al, 1993] was used for the long-range electrostatic interactions. The cutoff distances were 9 Å for Coulombic interactions and 14 Å for Lennard-Jones interactions. All bonds were constrained by the LINCS algorithm with a timestep of 2 fs. Periodic boundary conditions were applied in all three directions. The concentrations and orientational distributions of the growth units at the interfaces were extracted from the trajectories of MD simulation results of the last 5 ns.

The average concentration of the adsorbed growth units,  $X_{A(hkl)}$ , was obtained by calculating the mole fraction of adipic acid in water for all molecules

whose center of mass are within the first fluid layer. The first fluid layer was defined as a layer with a thickness of one  $d_{hkl}$  in the  $z$  direction from the average value of the center of mass for the topmost layer of the crystal slab. For the (002) face, however, a thickness of  $2 d_{hkl}$  was assumed because of the two alternating layers of growth units present in the  $z$  direction. From the orientations of these adsorbed growth units, the probability of orientational distributions  $P(\tau)$  and the corresponding free energy distributions  $G^*(\tau)$  are obtained. The free energy landscape of the different growth units was deduced in either a 1-dimensional or a 2-dimensional space depending on the number of angles considered. The molar enthalpy of dissolution,  $\Delta H^{diss}$ , of adipic acid in water at 307 K, which was interpolated from the data in range from 303.0 to 403.0 K reported by Suren and coworkers was 10.7 kcal/mol [Suren et al., 2013].  $\xi_{hkl}$  and  $n_{hkl}$  values obtained from the PBC analysis and the  $C_l^*$  values obtained from the MD simulation were used to calculate the average step energy  $\bar{\phi}_{hkl}^{step}$  and kink density  $\rho_{hkl}^{kink}$ .

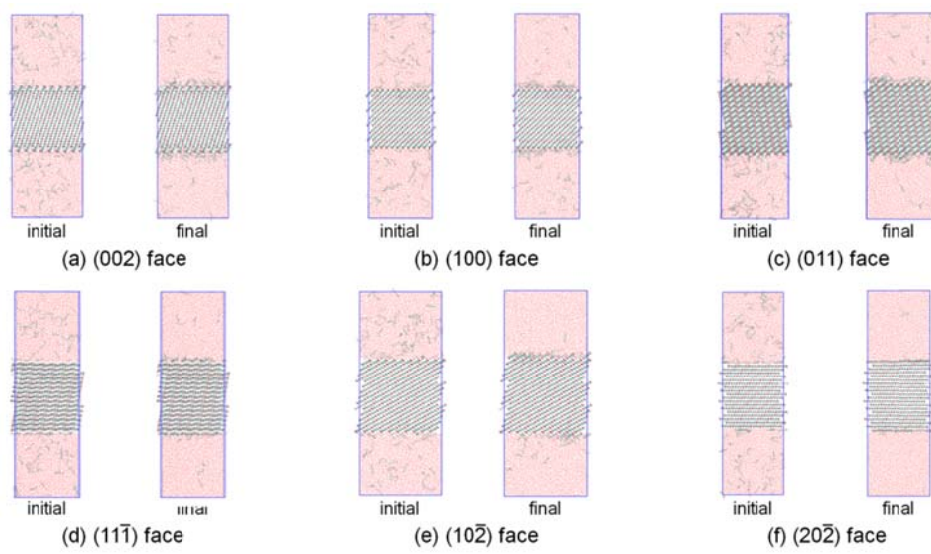


**Figure 4-4. Snapshots of the simulation cells for the different adipic acid crystal faces.**

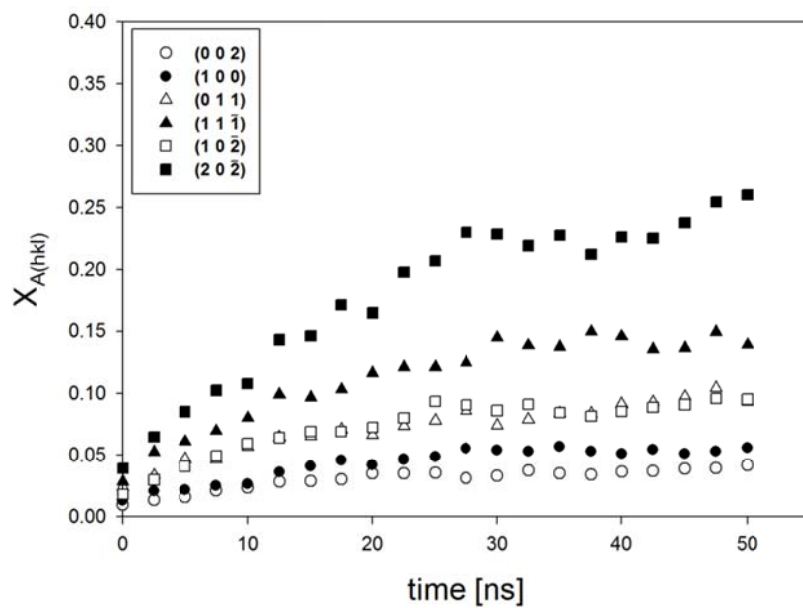
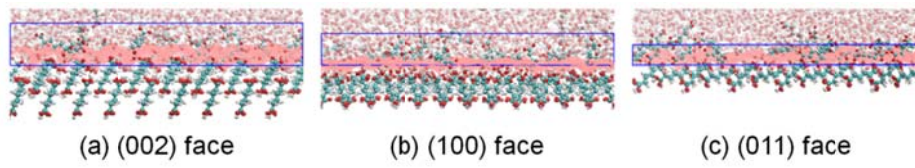
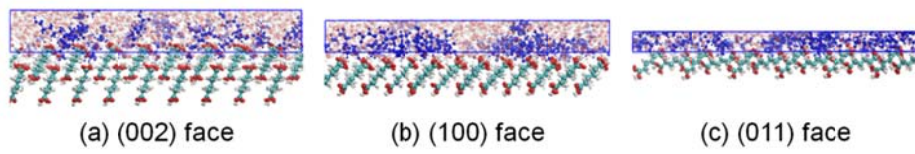


Figure 4-5. Concentration of the adsorbed adipic acid molecules at the crystal-solution interface layer.



**Figure 4-6. Snapshots of the Connolly surfaces**



**Figure 4-7. Snapshots of the adsorbed growth units in the interface layer**

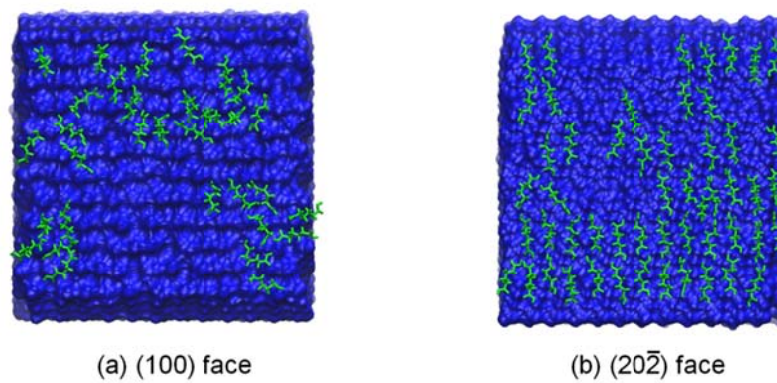


**Figure 4-8. Snapshots of the equilibrated growth units on the interface**

#### 4.1.4. Polygonal Spiral Growth Model

The original ISA model suggests a rate expression which lacks terms for both the edge-dependent lateral velocity and the geometry of the spirals. This derives from the fact that concentric circular spiral of Cabrera and Levine is assumed. Within the framework of ISA, the edge-dependent values of the step energies, which are required for the calculation of the edge-dependent lateral velocity, cannot be estimated because of the process of averaging over all step energies within the plane parallel to the given crystal face. On the other hand, the geometry of the spirals can be considered using procedures suggested by Winn and Doherty [Winn and Doherty, 2000]. However, the step energies and the related kink energies are independent of the edge directions which implies square or regular hexagon nucleus. Different values of pre-factors  $\kappa$  and different relations between  $\bar{\phi}_{hkl}^{kink}$  and  $\bar{\phi}_{hkl}^{step}$  are assigned for different spiral geometries.

In order to determine the pre-factors, possible geometries for the spirals are examined. As in the 14 possible Bravais lattices for the 3D case, the rotational symmetry in 2D allow 5 Bravais lattices of the square, hexagonal, rectangular, oblique, and centered rectangular. Considering these 2D lattices, allowed rotation symmetries are one-, two-, three-, four-, and sixfold rotations [Kittel, 2005]. If only the first-neighbor interactions are considered for the strong interactions between growth units, four or six-sided spirals are possible which are considered in this work.

The relative growth rate with these geometrical factors leads to,

$$R_{hkl}^{rel} \propto \frac{n_{hkl} d_{hkl}}{\kappa_{n_{hkl}} C_{l(hkl)}^* \xi_{hkl}} X_A^{C_{l(hkl)}^*} \left[ 1 + \frac{1}{2} \exp \left\{ \left( \frac{\bar{\phi}_{hkl}^{kink}}{\bar{\phi}_{hkl}^{step}} \right)_{n_{hkl}} \frac{C_{l(hkl)}^* \xi_{hkl} \Delta H^{diss}}{n_{hkl} k_B T} \right\} \right]^{-1} \quad (97)$$

where  $\kappa_{n_{hkl}} = 8$  and  $\bar{\phi}_{hkl}^{step} = \bar{\phi}_{hkl}^{kink}$  for  $n_{hkl} = 4$ , while  $\kappa_{n_{hkl}} = 6$  and  $\bar{\phi}_{hkl}^{step} = 2\bar{\phi}_{hkl}^{kink}$  for  $n_{hkl} = 6$ , if the differences in the edge velocities of selected edges within the plane, that are obtained from PBC analysis, are assumed to be small. The value of  $\kappa_{n_{hkl}}$  accounts for the number of turns and the distance required for one complete spiral rotation, and  $\left( \frac{\bar{\phi}_{hkl}^{kink}}{\bar{\phi}_{hkl}^{step}} \right)_{n_{hkl}}$  counts the number of unsaturated bonds at the edge surface. The equation for the kink density was restored to the original approach of Frenkel [Frenkel, 1945] because the average kink energy values were small compared to  $k_B T$ .



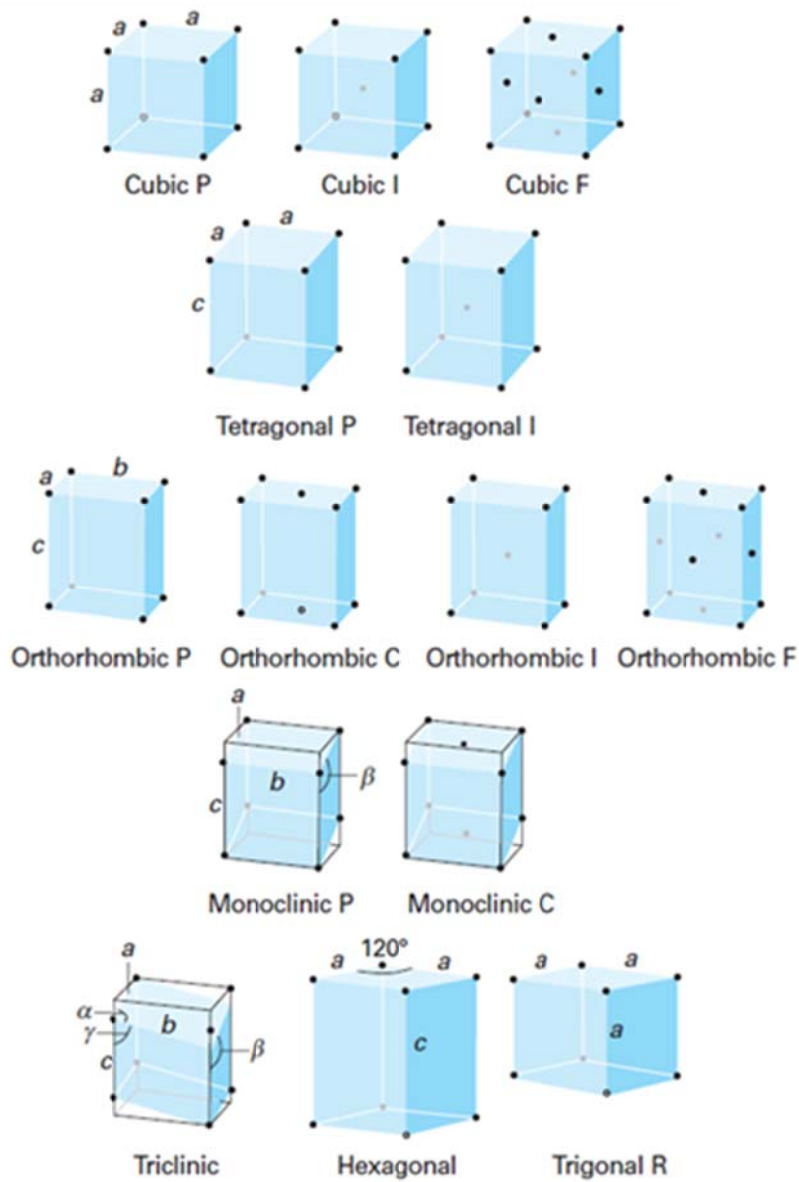
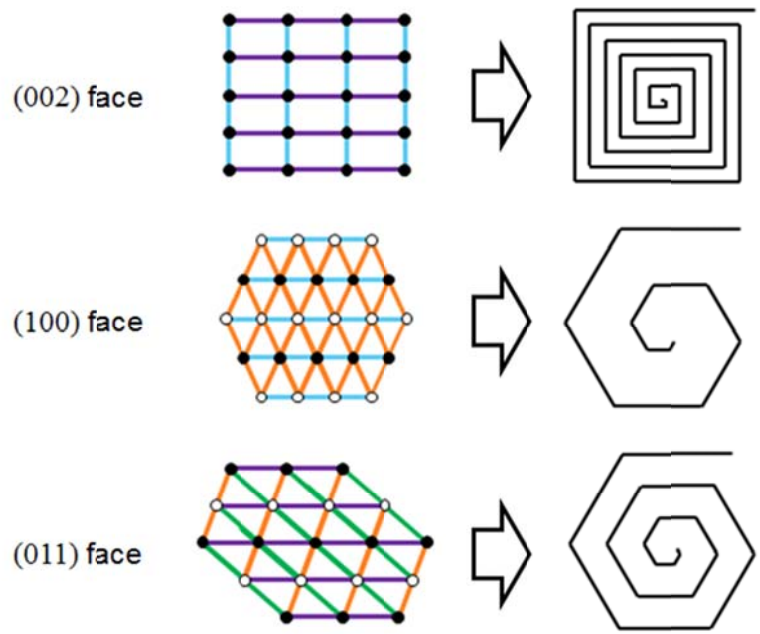


Figure 4-10. Three-dimensional Bravais lattices

[from Atkins and de Paula, 2006].



**Figure 4-11. Possible shapes of growth spirals for the dominant faces of adipic acid crystal.**

## 4.2. Computational Methods Used for $\beta$ -HMX Crystals

### 4.2.1. Periodic Bond Chain Analysis

Crystal structure of  $\beta$ -HMX by Deschamps et al. (CCDC 792930) was used. Compared to the earlier reported structure of Choi and Boutin (CCDC 1225495),  $(11\bar{1})$ ,  $(10\bar{2})$ , and  $(100)$  faces are newly indexed as  $(110)$ ,  $(101)$ , and  $(10\bar{1})$  faces, respectively.  $\beta$ -HMX crystallizes in a monoclinic structure with the space group  $P2_1/n$  with  $Z = 2$  per unit cell. The unit cell parameters are  $a = 6.5255 \text{ \AA}$ ,  $b = 11.0369 \text{ \AA}$ ,  $c = 7.364 \text{ \AA}$ ,  $\beta = 102.67^\circ$ . PBC analysis done by Shim and Koo is reproduced here [Shim and Koo, 2015].

General AMBER force field and atomic partial charges by MNDO/C semiempirical method [Thiel, 1981] were used for the atomic interactions. The lattice energy obtained from this combination was  $-45.50 \text{ kcal/mol}$  which is in agreement with the experimental value of  $-45.34 \text{ kcal/mol}$  [Qian et al., 2014].

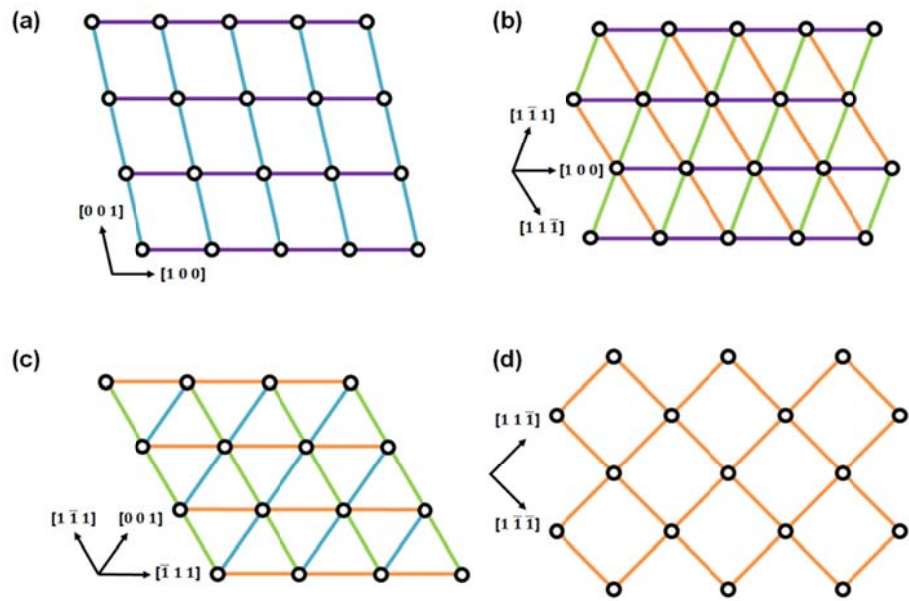


**Figure 4-12. Bonding structures for the (a) (020), (b) (011), (c) (110), and (d) (101) faces of  $\beta$ -HMX crystal.**

**Table 4-5 Interplanar distances and attachment energies for the F-faces of  $\beta$ -HMX**

Layer Miller Index	$d_{hkl}$ [ $\text{\AA}$ ]	$E_{hkl}^{att}$ [kcal/mol]
(020)	5.518	-24.69
(011)	6.021	-22.46
(110)	5.515	-28.05
(101)	5.387	-35.17

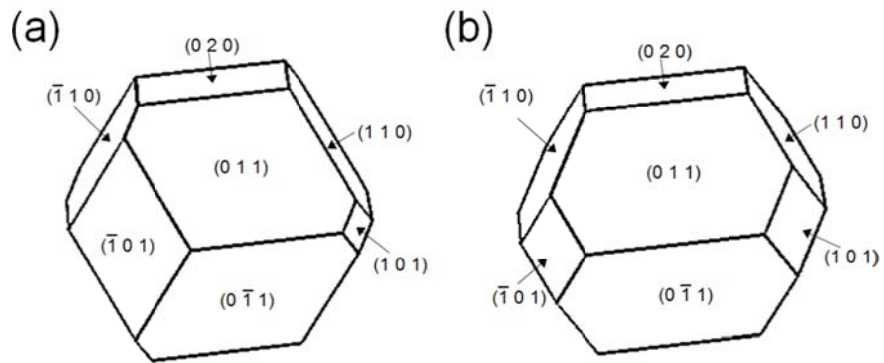


**Figure 4-13. Growth morphology of  $\beta$ -HMX crystal predicted by (a) BFDH model and (b) AE model.**

## 4.2.2. Interfacial Structure Analysis

The generalized AMBER force field [Cornell et al., 1995; Wang et al., 2004] was used for the HMX and acetone molecules. Bergh and Caleman have reported that when generalized AMBER force field was applied to HMX crystal, the crystal symmetries (and other properties such as the density, isothermal compressibility, bulk modulus, and coefficients of thermal expansions) were preserved at the ambient and high temperature-pressure conditions for the crystal structure of Deschamps [Bergh and Caleman, 2016]. The relaxed molecular structure of the crown and chair conformations of an HMX molecule were obtained by density functional theory (DFT) structural optimization performed at B3LYP/6-31G(d,p) level starting from the crown and chair conformations which are in  $\alpha$ -HMX and  $\beta$ -HMX crystals, respectively. The relaxation was also performed on the acetone molecule using the same method.

Initially, two sets of partial atomic charges were computed using the AM1-BCC model [Jakalian et al., 2002] and restrained electrostatic potential (RESP) formalism [Bayly et al., 1993] to emulate the electrostatic potential evaluated at HF/6-31G\* level of theory using R.E.D. tools [Dupradeau et al., 2010]. Charge derivation for the AM1-BCC model was performed by AmberTools16 [Salomon-Ferrer et al., 2013; Case et al., 2005]. An additional charge set for boat-boat conformation by AM1-BCC model was prepared for the conformational analysis of a HMX molecule in acetone solution using the initial atomic coordinates by Molt and coworkers [Molt et al., 2013]. DFT calculations for the RESP formalism were carried out using GAMESS-US [Schmidt et al., 1993; Gordon and Schmidt, 2005]. The effect of two charge sets on the exploration of the conformational space was compared using the plot suggested by Evans and Boeyens [Evans and Boeyens, 1988]. RESP charge set was chosen for calculating the local concentrations and the free energy surfaces.

Initial surface structures of (011), (020), (110), and (101) faces were cleaved using Materials Studio (version 7.0) in the appropriate orientations. All MD simulations were performed by GROMACS 5.1.4 [Brendsen et al., 1995; Lindahl et al., 2001; van der Spoel et al., 2005; Hess et al., 2008] equipped with PLUMED 2.3 [Tribello et al., 2014] plugin. An acetone solution with the HMX mole fraction of 0.00724 at 313.15 K (56 HMX molecules and 7680 acetone molecules) was prepared using the genbox package of GROMACS. This concentration corresponds to a supersaturation value of  $\sigma = 0.613$  at 293.15K which is roughly 90% of the lowest onset supersaturation  $\sigma_{2D}$ , the supersaturation at which transition from spiral growth dominant regime to 2D nucleation growth dominant regime occurs among the F-faces [Shim and Koo, 2015].

After insertion, energy minimization of the molecules by steepest descent method and equilibration at 313.15 K and 1.013 bar for 1 ns were performed. The resulting solution was brought into contact with the specific faces, and then the whole system was equilibrated with short 100 ps NVT simulation at 313.15 K followed by 10 ns NPT simulation at 313.15 K, 1 bar. After equilibration, production runs were carried out in NPT simulation for 200 ns at 293 K, 1 bar. For all simulations, Bussi-Donadio-Parrinello thermostat [Bussi et al., 2007] and semiisotropic Berendsen barostat [Berendsen et al., 1984] followed by the semiisotropic Parrinello-Rahman barostat [Parrinello and Rahman, 1981; Nosé and Klein, 1983] were used with coupling constants of 0.1 and 2 ps, respectively. All bonds were constrained by LINCS algorithm with a timestep of 2 fs. The cutoff distances were 1.4 nm for both Coulombic interaction and Lennard-Jones interactions. The Particle Mesh Ewald (PME) method [Darden et al., 1993] was used for the long-range electrostatic interactions. Three-dimensional periodic boundary conditions were applied.

A Matlab implementation of the Finite Temperature String method by Vanden-Eijnden [Vanden-Eijnden and Venturoli, 2009] was modified for use in reducing the dimensionality of the free energy surface. The value of the parameters used was the temperature parameter  $\mu = 10$ , timestep  $h = 0.001$ , smoothing coefficient  $\kappa = 0.1$ , and number of images  $n_1 = 30$ .

**Table 4-6. Atomic partial charges of the HMX molecule by the AM1-BCC model within GAFF for the chair conformation.**

Atom	Partial charge
o	-0.179000
no	0.458000
n3	-0.808900
c3	0.474000
h2	0.117450

**Table 4-7. Atomic partial charges of the HMX molecule by the AM1-BCC model within GAFF for the crown conformation.**

Atom	Partial charge
o	-0.166000
no	0.453000
n3	-0.823400
c3	0.472000
h2	0.115200

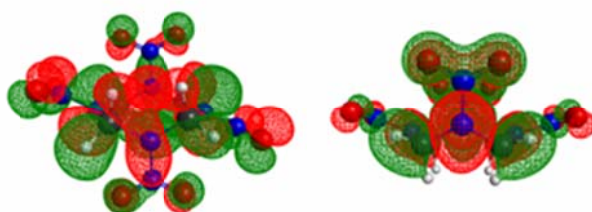
**Table 4-8. Atomic partial charges of the HMX molecule by the AM1-BCC model within GAFF for the boat-boat conformation.**

Atom	Partial charge
o	-0.175500
no	0.429500
n3	-0.797901
c3	0.438000
h2	0.140700

**Table 4-9. Atomic partial charges of the HMX molecule by the RESP formalism within GAFF.**

Atom	Partial charge
o	-0.409000
no	0.694600
n3	0.001400
c3	-0.141600
h2	0.131800

HOMO isosurface at 0.018 a.u.



ESP (a.u.) mapped onto  $\rho = 0$  a.u.

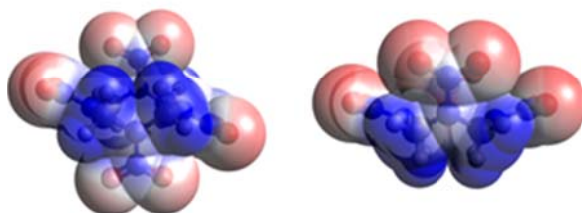


**Figure 4-14. HOMO isosurfaces and electrostatic potentials calculated for the chair and crown conformations of HMX with RESP formalism.**

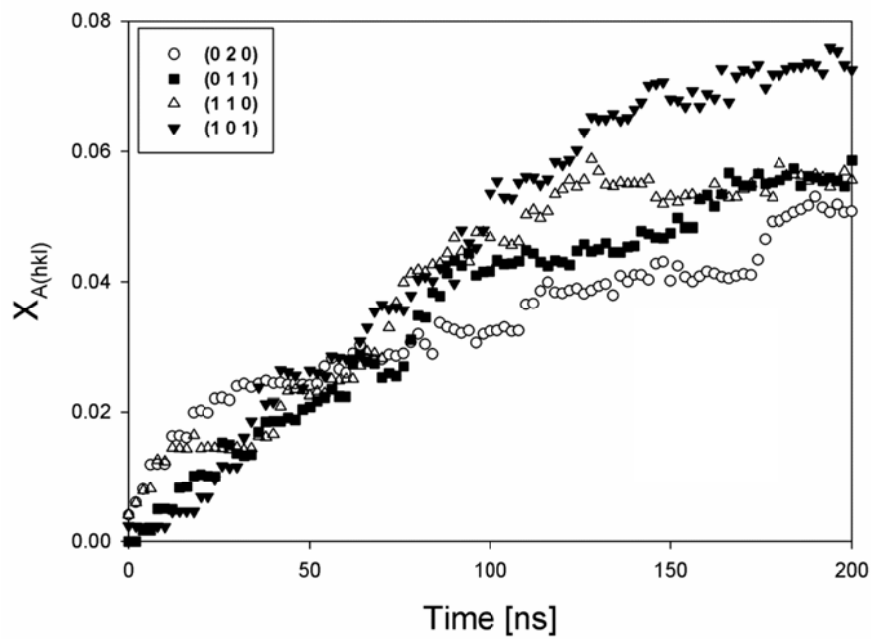
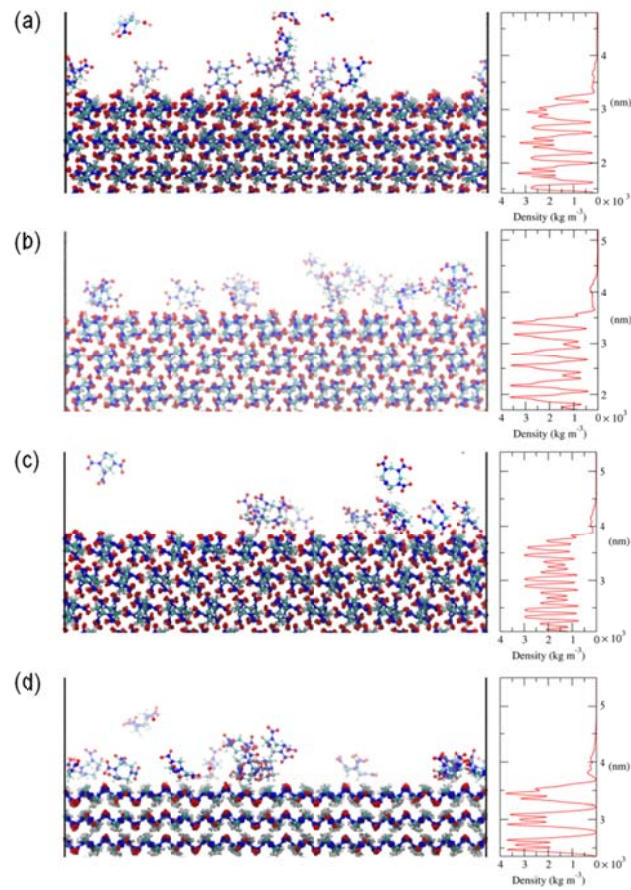


Figure 4-15. Concentration of the adsorbed HMX molecules at the crystal-solution interface layer.



**Figure 4-16. Local density values calculated on (a) (020), (b) (011), (c) (110), and (d) (101) faces.**

### 4.2.3. Metadynamics with Order Parameters

To investigate the free energy surfaces associated with the reorientation of an adsorbed HMX molecule in the acetone solution in contact to specific crystal faces, metadynamics [Laio and Parrinello, 2002] was used.

In a metadynamics simulation, a coarse-grained dynamics is driven by the forces from the free energy of the system and a sum of history dependent bias potentials in the space of a set of selected degrees of freedom called the collective variables  $S(\mathbf{R})$  which are functions of the atomic coordinates  $\mathbf{R}$ .

$$S(\mathbf{R}) = (S_1(R), S_2(R), \dots, S_d(R)) \quad (98)$$

where  $d$  is the dimensionality of the collective variables.

The equilibrium distribution of the collective variables without any bias is expressed as

$$P(s) = \int d\mathbf{R} \delta(s - S(\mathbf{R}))P(\mathbf{R}) \quad (99)$$

Since the distribution of the atomic coordinates are expressed as

$$P(\mathbf{R}) = \frac{\exp(-U(\mathbf{R})/k_B T)}{\int d\mathbf{R} \exp(-U(\mathbf{R})/k_B T)} \quad (100)$$

where  $U$  is the potential energy. The equilibrium distribution of  $s$  is expressed as

$$P(s) = \frac{\exp(-F(s)/k_B T)}{\int ds \exp(-F(s)/k_B T)} \quad (101)$$

where  $F$  is the Helmholtz free energy.

The free energy with respect to the collective variables is given by

$$F(s) = -\frac{1}{\beta} \ln P(s) \quad (102)$$

From a trajectory,  $P(s)$  can be obtained by taking the histogram along this trajectory as

$$P(s) \sim \frac{1}{t} \int_0^t dt' \delta(S(\mathbf{R}(t')) - s) \quad (103)$$

For a non-Boltzmann sampling method with a bias  $V(s)$  added to the potential, the equilibrium distribution of the collective variables is changed to

$$P(s) = \frac{\exp(-F(\mathbf{s})/k_B T - V(s)/k_B T)}{\int ds \exp(-F(\mathbf{s})/k_B T - V(s)/k_B T)} \quad (104)$$

In a metadynamics simulation, Gaussian bias potentials are added every few steps so that the history-dependent potential becomes

$$V_G(S(\mathbf{R}), t) = \sum_{\substack{t'=\tau_G, 2\tau_G \\ t' \leq t}} \omega \exp\left(-\sum_{i=1}^d \frac{(S_i(\mathbf{R}) - s_i(\mathbf{R}(t')))^2}{2\sigma_i^2}\right) \quad (105)$$

where  $\omega$  is the height,  $\sigma_i$  is the width, and  $\tau_G$  is the frequency of added Gaussians. At a sufficiently long time, an estimate of the underlying free energy surface can be obtained with

$$\lim_{t \rightarrow \infty} V_G(S, t) \sim -F(S) \quad (106)$$

For the well-tempered variant [Barducci et al, 2008], the height is rescaled to

$$\omega(S, t) = \omega_0 \exp\left(-\frac{V_G(S, t)}{k_b \Delta T}\right) \quad (107)$$

where  $\Delta T$  is a temperature. In this case, the bias potential converges to

$$\lim_{t \rightarrow \infty} V_G(S, t) \sim -\frac{\Delta T}{\Delta T + T} F(S) \quad (108)$$

The collective variables (1) should be explicit functions of the atomic positions and should have continuous derivatives with respect to them as well, (2) should be able to distinguish the different states of the system by representing every slow evolving degree of freedom of the system. For the purpose of describing a crystallization process, traditionally used collective variables include coordination numbers and Steinhardt parameters [Steinhardt et al., 1983] which are applicable to highly symmetric molecules or spherical geometry. For non-spherical cases like organic molecular crystals, however, the order parameters suggested by Santiso and Trout [Santiso and Trout, 2011] is considered appropriate which has been extended for various nucleation simulations [Giberti et al., 2015]. The parameter is based on the concept of a generalization of the pair distribution

function, which considers the center of mass distances between two molecules, to include the relative orientations between them and internal degrees of freedom of the molecule as well. For a crystal at 0 K, the peaks are completely localized with

$$g(\mathbf{r}, q, \psi) = \sum_{\alpha}^{\infty} \delta(\mathbf{r} - \mathbf{r}_{\alpha}) \delta(q - q_{\alpha}) \delta(\psi - \psi_{\alpha}) \quad (109)$$

where  $\mathbf{r}$  and  $q$  are the center of mass distances and relative orientation between a molecule and its neighbor,  $\psi$  is the internal degrees of freedom such as its conformation. Only the terms corresponding to those within the unit cell are relevant in practice. For a crystal at finite temperatures, the delta functions are replaced with the probability densities as

$$g(\mathbf{r}, q, \psi) = \sum_{\alpha}^{\infty} f_{\alpha}(\mathbf{r}, q, \psi) \approx \sum_{\alpha}^{\infty} f_{\alpha}^r(\mathbf{r}) f_{\alpha}^q(q) f_{\alpha}^{\psi}(\psi) \quad (110)$$

where  $f$  denotes the associated probability density. The normalization factor can be modified so that the order parameters discriminate between the disordered state at  $S = 0$  and the ordered state at  $S = 1$  [Giberti, 2015].

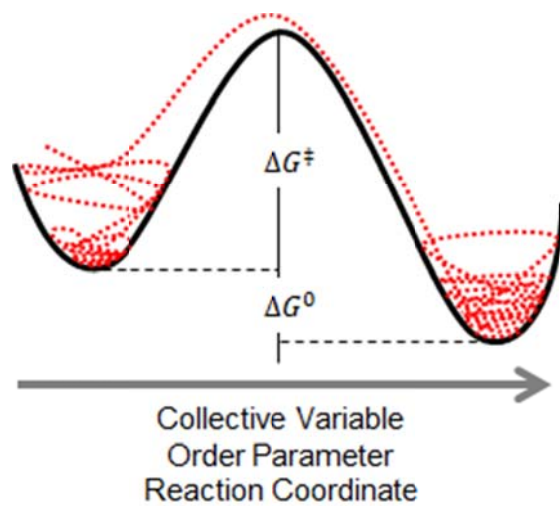


Figure 4-17. Typical free energy barriers related to rare event problems.

Conformations of ring-containing molecules can be described equivalently by the Cartesian coordinates of the ring atoms, dihedral angles, Strauss-Pickett coordinates [Strauss and Pickett, 1970], and Cremer-Pople puckering coordinates [Cremer and Pople, 1975; Evans and Boeyens, 1988]. As for HMX which has eight atoms on the ring, 24 Cartesian coordinate, 8 dihedral angles, or 5 puckering coordinates (three amplitudes and two phase angles) are needed to describe its conformation. Cremer-Pople puckering coordinate was used because it has the least number of parameters among them.

The Cremer-Pople coordinates of a molecule with N-membered ring is obtained from the positions of the ring atoms. If the position vector of the nuclei of the  $i$ th atom is specified by  $R_i$ , the origin must satisfy

$$\sum_{j=1}^N R_j = 0 \quad (111)$$

The mean plane passing through the origin is uniquely defined by

$$\sum_{j=1}^N z_j = 0 \quad (112)$$

$$\sum_{j=1}^N z_j \cos[2\pi(j-1)/N] = 0 \quad (113)$$

$$\sum_{j=1}^N z_j \sin[2\pi(j-1)/N] = 0 \quad (114)$$

The orientation of this mean plane is determined by

$$R' = \sum_{j=1}^N R \sin[2\pi(j-1)/N] \quad (115)$$

$$R'' = \sum_{j=1}^N R \cos[2\pi(j-1)/N] \quad (116)$$

$$n = \frac{R' \times R''}{|R' \times R''|} \quad (117)$$

The displacements from the mean plane are then given by

$$z_j = R_j \cdot n \quad (118)$$

For  $N$  larger than three, the generalized ring-puckering coordinates are defined as,

$$q_m \cos \phi_m = (2/N)^{1/2} \sum_{j=1}^N z_j \cos[2\pi m(j-1)/N] \quad (119)$$

$$q_m \sin \phi_m = -(2/N)^{1/2} \sum_{j=1}^N z_j \sin[2\pi m(j-1)/N] \quad (120)$$

where  $m = 2, 3, \dots, (N-1)/2$  for odd  $N$  and  $N/2 - 1$  for even  $N$  and  $q_m \geq 0, 0 \leq \phi_m \leq 2\pi$ . For even  $N$ , there is an additional puckering coordinate of

$$q_{N/2} = N^{-1/2} \sum_{j=1}^N z_j \cos[\pi(j-1)] \quad (121)$$

which is equivalent to

$$\cos\theta = q_{N/2} / \left( \sum_m q_m^2 \right)^{1/2} \quad (122)$$

It is important that there are several equivalent values of Cremer-Pople puckering coordinates for a conformation. The rules for enumerating them have been identified by Kessler and Perez for molecules with arbitrary sized rings [Kessler and Perez, 2012]. For a molecule with a ring comprised of  $N$  atoms, a  $N$ -dimensional vector for the displacements from the mean plane  $z_i$  is defined as,

$$\mathbf{z} = (z_1, \dots, z_N) \quad (123)$$

For operations are defined as

$$\text{Translation T: } Tz = (z_2, z_3, \dots, z_N, z_1) \quad (124)$$

$$\text{Change of direction D: } Dz = -(z_2, z_3, \dots, z_N, z_1) \quad (125)$$

$$\text{Mirror image M: } Mz = -(z_1, z_2, \dots, z_{N-1}, z_N) \quad (126)$$

the following relations hold that

$$\text{Translation T: } Tq_m = q_m, T\varphi_m = \varphi_m + \frac{2\pi m}{N} \quad (127)$$

and if  $N$  is even,  $T_{q_{N/2}} = -q_{N/2}$ .

$$\text{Change of direction D: } Dq_m = q_m, D\varphi_m = \pi - \varphi_m \quad (128)$$

and if  $N$  is even,  $D_{q_{N/2}} = -q_{N/2}$ .

$$\text{Mirror image M: } Mq_m = q_m, M\varphi_m = \pi + \varphi_m \quad (129)$$

and if  $N$  is even,  $M_{q_{N/2}} = -q_{N/2}$ . For an eight-membered ring, these operations result in

$$\text{Translation T: } T\varphi_2 = \varphi_2 + \frac{\pi}{2}, T\varphi_3 = \varphi_3 + \frac{3\pi}{4}, T\theta = \pi - \theta \quad (130)$$

$$\text{Change of direction D: } D\varphi_2 = \pi - \varphi_2, D\varphi_3 = \pi - \varphi_3, D\theta = \pi - \theta \quad (131)$$

$$\text{Mirror image M: } M\varphi_2 = \varphi_2 + \pi, M\varphi_3 = \varphi_3 + \pi, M\theta = \pi - \theta \quad (132)$$

while  $q_2$  and  $q_3$  are invariant under all three operations.

Using these three operations, it is possible to deduce that the chair conformation of an HMX molecule has eight equivalent peaks at

$$\varphi_3, \frac{\pi}{2} + \varphi_3, \pi + \varphi_3, \frac{3\pi}{2} + \varphi_3, \frac{\pi}{2} - \varphi_3, \pi - \varphi_3, \frac{3\pi}{2} - \varphi_3, 2\pi - \varphi_3 \quad (133)$$

Representative puckering coordinates for eight-membered rings can be obtained by using the corollary by Kessler and Perez.

$$\varphi'_2 = (\varphi_2 \bmod \pi) \quad (134)$$

$$\varphi'_3 = (\varphi_3 \bmod \pi/2) \quad (135)$$

$$m'_2 = (\varphi_2 \operatorname{div} \pi) \quad (136)$$

$$m'_3 = (\varphi_3 \operatorname{div} \pi/2) \quad (137)$$

$$\theta' = D^{m'_2+m'_3}\theta \quad (138)$$

where *div* denotes integer division.

$$(\varphi_2'', \varphi_3'') = \begin{cases} (\varphi_2', \varphi_3') & \text{if } \varphi_2' \leq \pi/2 \\ (\pi - \varphi_2', \frac{\pi}{2} - \varphi_3') & \text{if } \varphi_2' > \pi/2 \end{cases} \quad (139)$$

$$(\bar{\varphi}_2, \bar{\varphi}_3) = \begin{cases} (\varphi_2'', \varphi_3'') & \text{if } \varphi_2'' \leq \pi/4 \\ (\pi/2 - \varphi_2'', \pi/4 - \varphi_3'') & \text{if } \varphi_2'' > \pi/4 \text{ and if } \varphi_3'' \leq \pi/4 \\ (\pi/2 - \varphi_2'', 3\pi/4 - \varphi_3'') & \text{if } \varphi_2'' > \pi/4 \text{ and if } \varphi_3'' > \pi/4 \end{cases} \quad (140)$$

which will reduce the range of the  $\bar{\varphi}_2$  and  $\bar{\varphi}_3$  into  $[0, \pi/4]$  and  $[0, \pi/2]$ , respectively. In spite of their reduction of the ranges for the phase angles, the representative puckering coordinates have not been used in the metadynamics simulations because of the computational efficiency and inability to reduce the chair phase angles into a single value.

For the five mutually orthogonal Cartesian forms, a vector of Cartesian form Cremer-Pople puckering coordinates  $\mathbf{CP}$  is defined as,

$$\mathbf{CP} = (CP_1, CP_2, CP_3, CP_4, CP_5) = (q_2 \cos \phi_2, q_2 \sin \phi_2, q_3 \cos \phi_3, q_3 \sin \phi_3, q_4) \quad (141)$$

The distribution of the puckering coordinates is approximated as a multiplication of five independent Gaussian terms

$$f_\alpha^\psi(\mathbf{CP}) = \prod_{n=1}^5 \frac{1}{\sqrt{2\pi\sigma_{CP_n}^2}} \exp \left[ -\frac{(CP_n - \overline{CP_n})^2}{2\sigma_{CP_n}^2} \right] \quad (142)$$

where  $\overline{CP_n}$  and  $\sigma_{CP_n}$  are the mean and standard deviation values of the corresponding probability distribution of the Cremer-Pople puckering coordinates. More accurate description can be obtained by using multivariate Gaussian such as

$$f_\alpha^\psi(\mathbf{CP}) = \frac{1}{(2\pi)^{5/2}} \frac{1}{|\Sigma|^{1/2}} \exp \left[ -\frac{1}{2} (\mathbf{CP} - \overline{CP_\alpha})^T \Sigma_{CP}^{-1} (\mathbf{CP} - \overline{CP_\alpha}) \right] \quad (143)$$

where  $\Sigma$  is the covariance matrix. In this work, however, the distribution was approximated by the multiplication of Gaussians with a single variable each for computational efficiency.

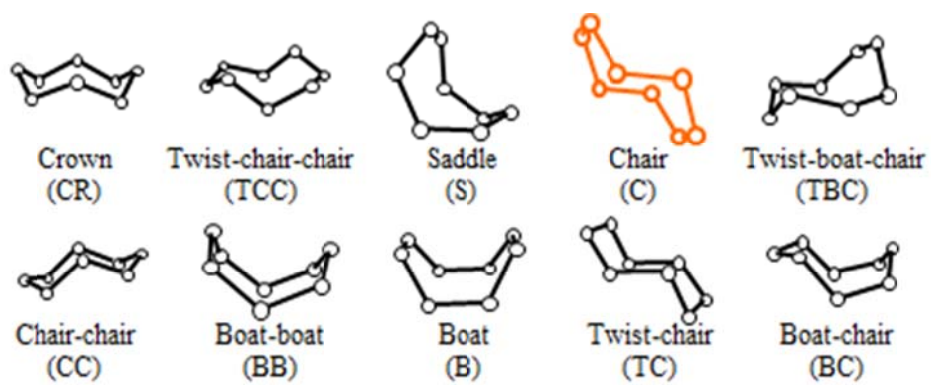


Figure 4-18. Canonical conformations of cyclooctane by Evans and Boeyens [Evans and Boeyens, 1988].

For the relative orientation between two molecules, quaternions of the molecular frames on ring nitrogen atoms that are connected to nitro groups are used. In two-dimensional space, rotation of the coordinate frame  $\{\mathbf{X}, \mathbf{Y}\}$  onto  $\{\mathbf{x}, \mathbf{y}\}$  can be expressed by the rotation matrix

$$R = \begin{bmatrix} \cos \theta & \sin \theta \\ -\sin \theta & \cos \theta \end{bmatrix} \quad (144)$$

where  $\theta$  is the angle between the original frame and the rotated frame. Similarly, rotation of the coordinate frame  $\{\mathbf{X}, \mathbf{Y}, \mathbf{Z}\}$  onto  $\{\mathbf{x}, \mathbf{y}, \mathbf{z}\}$  can be expressed by the rotation matrix (or also called the direction cosine matrix)

$$R = \begin{bmatrix} \mathbf{x} \cdot \mathbf{X} & \mathbf{y} \cdot \mathbf{X} & \mathbf{z} \cdot \mathbf{X} \\ \mathbf{x} \cdot \mathbf{Y} & \mathbf{y} \cdot \mathbf{Y} & \mathbf{z} \cdot \mathbf{Y} \\ \mathbf{x} \cdot \mathbf{Z} & \mathbf{y} \cdot \mathbf{Z} & \mathbf{z} \cdot \mathbf{Z} \end{bmatrix} = \begin{bmatrix} r_{11} & r_{12} & r_{13} \\ r_{21} & r_{22} & r_{23} \\ r_{31} & r_{32} & r_{33} \end{bmatrix} \quad (145)$$

Euler angles that can also express the rotation in a three-dimensional space is related to the rotation matrix as

$$\tan \psi = \frac{r_{12}}{r_{11}} \quad (146)$$

$$\sin \theta = -r_{13} \quad (147)$$

$$\tan \phi = \frac{r_{23}}{r_{33}} \quad (148)$$

The quaternion equivalent to this rotation matrix can be expressed as

$$\mathbf{q} = (q_w, q_x, q_y, q_z) = (q_w, \mathbf{q}) \quad (149)$$

where the components are related to the components of the rotation matrix as

$$\mathbf{q} = \left( \frac{1}{2} \sqrt{r_{11} + r_{22} + r_{33} + 1}, \frac{r_{23} - r_{32}}{4q_w}, \frac{r_{31} - r_{13}}{4q_w}, \frac{r_{12} - r_{21}}{4q_w} \right) \quad (150)$$

Other relations between quaternion and Euler angles also exist as

$$q_w = \cos \frac{\psi}{2} \cos \frac{\theta}{2} \cos \frac{\phi}{2} + \sin \frac{\psi}{2} \sin \frac{\theta}{2} \sin \frac{\phi}{2} \quad (151)$$

$$q_x = \cos \frac{\psi}{2} \cos \frac{\theta}{2} \sin \frac{\phi}{2} - \sin \frac{\psi}{2} \sin \frac{\theta}{2} \cos \frac{\phi}{2} \quad (152)$$

$$q_y = \cos \frac{\psi}{2} \sin \frac{\theta}{2} \cos \frac{\phi}{2} + \sin \frac{\psi}{2} \cos \frac{\theta}{2} \sin \frac{\phi}{2} \quad (153)$$

$$q_w = \sin \frac{\psi}{2} \cos \frac{\theta}{2} \cos \frac{\phi}{2} - \cos \frac{\psi}{2} \sin \frac{\theta}{2} \sin \frac{\phi}{2} \quad (154)$$

Other relations between the rotation matrix, quaternion, and Euler angles exist but will not be needed here. Quaternion can also be expressed in a hyper complex number as

$$\mathbf{q} = w\mathbf{u} + x\mathbf{i} + y\mathbf{j} + z\mathbf{k} \quad (155)$$

where the four elementary vectors have the relationship of

$$\mathbf{i}^2 = \mathbf{j}^2 = \mathbf{k}^2 = -\mathbf{u}, \mathbf{ij} = -\mathbf{ji} = \mathbf{k}, \mathbf{jk} = -\mathbf{kj} = \mathbf{i}, \mathbf{ki} = -\mathbf{ik} = \mathbf{j} \quad (156)$$

There are several quaternion operations that should be mentioned. The quaternion product of two quaternions  $p$  and  $q$  is defined as

$$pq = (p_w q_w - \mathbf{p} \cdot \mathbf{q}, p_w \mathbf{q} + q_w \mathbf{p} + \mathbf{p} \times \mathbf{q}) \quad (157)$$

This multiplication of two quaternions is closed under multiplication, associative, and not commutative. The conjugate of a quaternion  $q$  is defined as

$$q^* = (q_w, -\mathbf{q}) = (q_w, -q_x, -q_y, -q_z) \quad (158)$$

The norm of the quaternion  $q$  is defined as

$$\|q\| = \sqrt{q^* q} = \sqrt{q_w^2 + q_x^2 + q_y^2 + q_z^2} \quad (159)$$

The inverse of quaternion  $q$  has the same meaning of the inverse of the rotation matrix  $R$  and is defined as

$$q^{-1} = \frac{q^*}{\|q\|^2} \quad (160)$$

The relative orientation between two molecular frames  $q_{i,j}$  and  $q_k$  is calculated using the quaternion multiplication and conjugate as

$$q_{rel}(i,j,k) = (q_{rel,w}(i,j,k), q_{rel,x}(i,j,k), q_{rel,y}(i,j,k), q_{rel,z}(i,j,k)) = q_{i,j}^* q_k \quad (161)$$

where  $i = 1, 2$  is the index for asymmetric units,  $j = 1, 2$  is the index for the ring nitrogen atom with axial NO<sub>2</sub> groups of a crystal molecule, and  $k = 1, 2, 3$ , and 4 is the index for the ring nitrogen atoms with both the axial and equatorial NO<sub>2</sub> groups of a solute molecule. The distribution of the relative quaternions can be approximated by a bipolar Watson distribution [Santiso and Trout, 2011] of the form

$$f_\alpha^q(q) \approx \frac{1}{{}_1F_1(1/2, 2, \xi_\alpha)} \exp[\xi_\alpha (q_\alpha \cdot q_{rel}(i,j,k))^2] = \frac{1}{{}_1F_1(1/2, 2, \xi_\alpha)} \exp[\xi_\alpha q_{rel,w}^2(i,j,k)] \quad (162)$$

where  ${}_1F_1(1/2, 2, x)$  is the confluent hypergeometric function,  $q_\alpha$  is the mean relative orientation for the same asymmetric units of a crystal at 0 K and is equal to the quaternion multiplication identity (1, 0, 0, 0),  $\xi_\alpha$  is the concentration parameter for a crystal at the temperature of interest, and the symbol  $\cdot$  denotes the standard 4D dot product. From the above two probability densities, the two order parameters are defined as

$$S_1 = \sum_{\alpha=1}^8 \prod_{n=1}^5 \exp\left[-\frac{(CP_n - \overline{CP}_{n,\alpha})^2}{2\sigma_{CP_{n,\alpha}}^2}\right] \quad (163)$$

$$S_2 = \sum_{i=1}^2 \sum_{(k_1, k_2)} \left[ \frac{\exp\{\xi_\alpha (q_{rel,w}(i, j_1, k_1))^2\}}{\exp(\xi_\alpha)} \frac{\exp\{\xi_\alpha (q_{rel,w}(i, j_2, k_2))^2\}}{\exp(\xi_\alpha)} \right] \quad (164)$$

where  $i$  is the index for different asymmetric units,  $j$  is the index for the axial NO<sub>2</sub> groups of a crystal molecule,  $(k_1, k_2)$  is the pair of indices for NO<sub>2</sub> groups at the opposite side of the ring in the solute molecule.

The simulations were carried out in NVT simulation with the reduced cut off distances of 1.2 nm (1.1 nm for 101 face) to match half the box size. Gaussian hills with initial height of 0.1 kJ/mol, width of 0.1 in each CV, were deposited every 1 ps with the bias factor of 5.

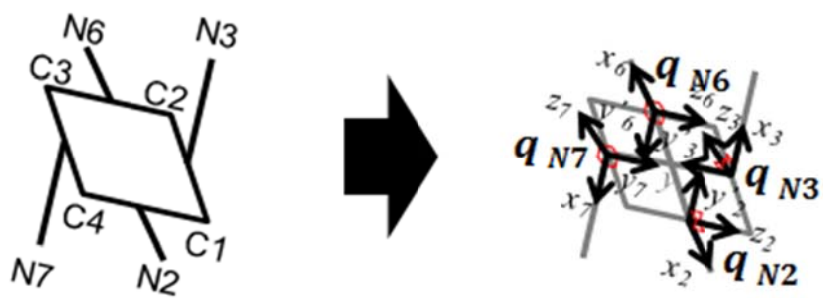


Figure 4-19. A schematic drawing of quaternions defined on atomic coordinates of HMX molecules.

#### 4.2.4. Generalized Interfacial Structure Analysis Model

The kink rate  $u_{hkl,i}$  is the net rate of growth units attachment into and detachment from kink sites on edge  $i$ . This can be used in the formulation of the edge dependent step velocities as [Kim et al., 2014; Li et al., 2016]

$$u_{hkl,i} = j_{hkl}^+ - j_{hkl,k,i}^- \quad (165)$$

$$v_{hkl,i} = a_{p,i} \rho_{hkl,i}^{kink} u_{hkl,i} \quad (166)$$

where  $j_{hkl}^+$  is the attachment rate of growth units into kink sites,  $j_{hkl,k,i}^-$  is the detachment rate of growth units from kink site  $k$  on edge  $i$ .

The rate expressions for kink attachment and detachment which are first and zeroth order in  $x_{eq,hkl}$  respectively [Li et al., 2016], can be expressed as

$$j_{hkl}^+ = k^+ x_{eq} S \quad (167)$$

$$j_{hkl,k,i}^- = k_{k,i}^- \quad (168)$$

where the rate constants are

$$k^+ = v_0 \exp\left(-\frac{\Delta G^\ddagger}{k_B T}\right) \approx v_0 \exp\left(-\frac{\Delta G_{desolv}^*}{k_B T}\right) \quad (169)$$

$$k_{k,i}^- = v_0 \exp\left(-\frac{\Delta G^\ddagger + \Delta G^0}{k_B T}\right) = k^+ \exp\left(-\frac{\Delta G^0}{k_B T}\right) \approx k^+ \exp\left(-\frac{\Delta W_{k,i}}{k_B T}\right) \quad (170)$$

where  $v_0$  is the frequency factor,  $\Delta G^\ddagger$  is the attachment energy barrier, which largely results from desolvation free energy barrier  $\Delta G_{desolv}^*$ ,  $\Delta G^0$  is the detachment energy barrier or standard free energy required to detach a growth unit from a kink-incorporated site. If the entropic portion is assumed to be zero, it is equal to the energetic detachment work from kink  $k$  on edge  $i$ ,  $\Delta W_{k,i} = \sum_j^m (\phi_{k,i}^{SF})_j$ , where  $(\phi_{k,i}^{SF})_j$  is the solid-fluid interaction energy of bond  $j$  on kink site  $k$  on edge  $i$ ,  $m$  is the total number of bonds at the kink site  $k$ .

The kink attachment rate is independent on the identity of the kink site. However, the detachment rate and the related detachment work is dependent on the kink site. As for the centrosymmetric growth units, all kink sites for a single direction along an edge are equivalent because the bonds exposed at any kink sites are the same. Therefore, the detachment work is isotropic ( $\Delta W_{k,i} = \Delta W_{hkl}$ ) over

the face which is half of the lattice energy in vacuum. Accordingly, the detachment rate is also isotropic ( $k_{k,i}^- = k_{hkl}^-$ ) over the face. This is not for the case of noncentrosymmetric growth units, where averaging the kink site dependent value for each edge is required.

$$\overline{\Delta W}_i = \frac{1}{n_k} \sum_{k=1}^{n_k} \Delta W_{k,i} \quad (171)$$

where  $n_k$  is the number of different kink sites on an edge. The detachment rate for a centrosymmetric unit on face  $hkl$  is

$$k_{hkl}^- = v_0 \exp\left(-\frac{\Delta G_{desolv}^* + \Delta W_{hkl}}{k_B T}\right) = k^+ \exp\left(-\frac{\Delta W_{hkl}}{k_B T}\right) \quad (172)$$

At equilibrium, the attachment rate and detachment rate are the same, resulting in

$$j_{hkl,eq}^+ = j_{hkl,eq}^- \quad (173)$$

$$S_{eq} = 1 \quad (174)$$

$$x_{eq,hkl} = \exp\left(-\frac{\Delta G^0}{k_B T}\right) \approx \exp\left(-\frac{\Delta W_{hkl}}{k_B T}\right) \quad (175)$$

Then the average detachment rate and kink rate over the face are

$$j_{hkl}^- = k_{hkl}^- = k^+ x_{eq,hkl} \quad (176)$$

$$u_{hkl} = k^+ x_{eq,hkl} (S - 1) = v_0 \exp\left(-\frac{\Delta G_{desolv}^*}{k_B T}\right) x_{eq,hkl} (S - 1) \quad (177)$$

If the  $a_{p,i}$ s are averaged over all edges on the face  $hkl$ ,

$$\bar{v}_{hkl} = v_0 \left[ \bar{a}_{p,hkl} \{x_{eq,hkl} (S - 1)\} \rho_{hkl}^{kink} \exp\left(-\frac{\Delta G_{desolv}^*}{k_B T}\right) \right] \quad (178)$$

If the concentration of the effective growth units at the interface is taken as the equilibrium concentration [Shim and Koo, 2016],

$$x_{eq,hkl} = X_{A(hkl)}^{eff} \quad (179)$$

collecting the anisotropic terms results in

$$\bar{v}_{hkl} \propto \bar{a}_{p,hkl} X_{A(hkl)}^{eff} \rho_{hkl}^{kink} \quad (180)$$

where  $\bar{a}_{p,hkl}$  is the average step propagation length on the face.

The concentration of the effective growth units is related to the equilibrium value of the concentration at the interface by the average effectiveness factor  $\delta_{hkl}$  which is determined from two free energy barriers: the free energy barrier for desolvation  $\Delta G_{desolv}^*$  and for reorientation  $\Delta G_{order}^*$ .

$$X_{A(hkl)}^{eff} = \delta_{hkl} X_{A(hkl)} \approx \frac{\exp\left(\frac{\Delta G_{desolv}^*}{k_B T}\right)}{\exp\left(\frac{\Delta G_{desolv}^*}{k_B T}\right) + \exp\left(\frac{\Delta G_{order}^*(hkl)}{k_B T}\right)} X_{A(hkl)} \quad (181)$$

Then the relative growth rate expressed as

$$R_{hkl} \propto \frac{\bar{a}_{p,hkl} d_{hkl}}{\bar{a}_{e,hkl} n_{hkl} \sin \bar{\alpha}_{hkl} \bar{\phi}_{hkl}^{kink}} \delta_{hkl} X_{A(hkl)} \left(1 + \frac{1}{2} \exp\left(\frac{\bar{\phi}_{hkl}^{kink}}{k_B T}\right)\right)^{-1} \quad (182)$$

In the original approach, edge dependent values are averaged by assuming square or regular hexagon spirals with  $\bar{a}_{e,hkl} \approx \bar{a}_{p,hkl} \approx a \approx (V_m)^{\frac{1}{3}}$ , where  $V_m$  is the molecular volume. The anisotropy between square and regular hexagon spirals can be further considered by comparing the lengths. The value of the ratio  $\bar{a}_{p,hkl}/\bar{a}_{h,hkl}$  is equal to 1 for the square and  $\sqrt{3}/2$  for the regular hexagon. Multiplying this ratio by the value of  $\sin \bar{\alpha}_{hkl}$  for each case result in the  $\bar{a}_{p,hkl}/(\bar{a}_{h,hkl} \sin \bar{\alpha}_{hkl})$  value of 1 for the both cases. Therefore, the relative rate expression is further simplified by collecting the anisotropic factors of  $G_{hkl}$  into

$$R_{hkl} \propto \frac{d_{hkl}}{C_{l(hkl)}^* \xi_{hkl}} \delta_{hkl} X_{A(hkl),eq} \left(1 + \frac{1}{2} \exp\left(\frac{C_{l(hkl)}^* \xi_{hkl} \Delta H^{diss}}{n_{hkl} k_B T}\right)\right)^{-1} \quad (183)$$

In comparison to the previous expression by Liu [Liu and Bennema, 1995],

$$R_{hkl}^{rel} \propto \frac{n_{hkl} d_{hkl}}{C_{l(hkl)}^* \xi_{hkl}} \delta_{hkl} X_{A(hkl),eq} \exp\left(-\frac{C_{l(hkl)}^* \xi_{hkl} \Delta H^{diss}}{n_{hkl} k_B T}\right) \quad (184)$$

where  $n_{hkl}$  is the number of nearest neighbors in the two-dimensional lattice and  $\bar{\alpha}_{hkl}$  is the angle between spiral edges, the factor of  $n_{hkl}$  is missing due to the anisotropic number of turns.

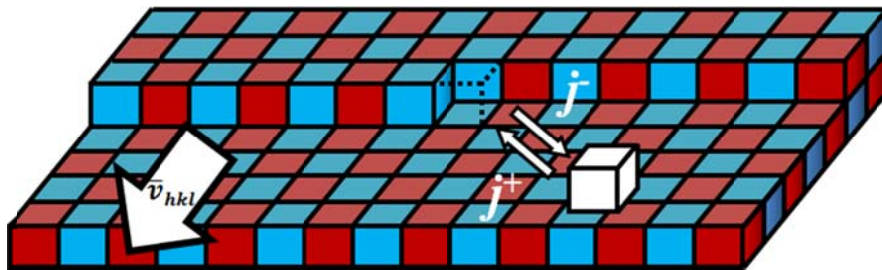


Figure 4-20. Attachment and detachment rates of the growth units around kink sites.

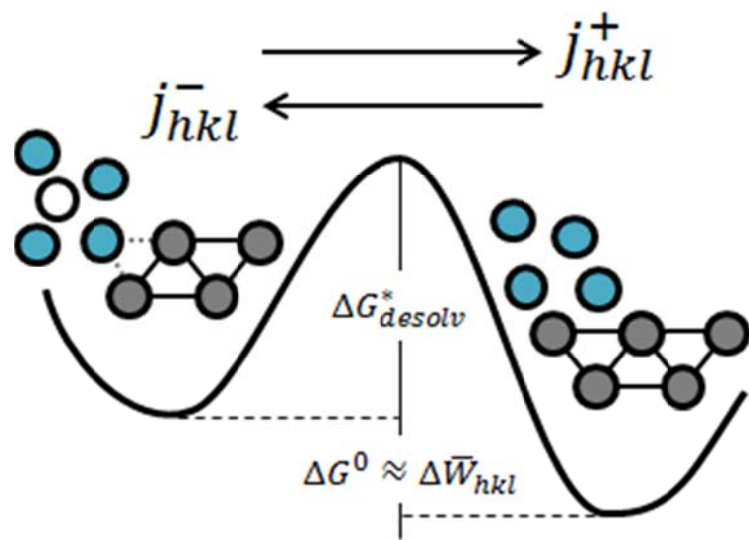
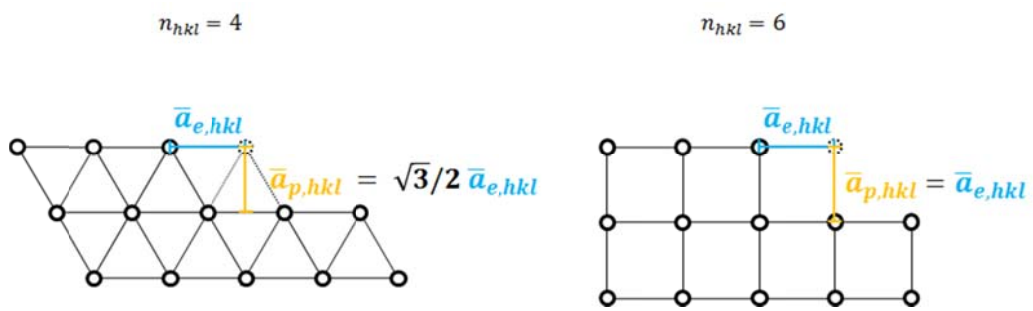


Figure 4-21. Free energy barriers related to the incorporation of solvated growth units into kinks from the solution.



**Figure 4-22.** The relation between edge length and propagation length for different number of nearest neighbors.

## Chapter 5. Results and Discussions

### 5.1. Morphology of the Adipic Acid Crystal

#### 5.1.1. Orientational Free Energy Surface

A two dimensional free energy surface can be obtained in a manner similar to that by Gnanasambandam and coworkers [Gnanasambandam et al., 2010]. The altitude angle  $\theta$  and the azimuthal angle  $\phi$  were used to describe the orientation of the molecule within the 3 dimensional space. This two dimensional free energy surface show that with the exception of (100) face, the F1-units are in the areas with relatively low free energy. This could be attributed to the relatively high value of  $\theta$  for the F1-units of (100) face compared to the others. Although (002) face has a higher value of  $\theta$  for the F1-unit, this can be overcome by the geometry of alternating layers which can be seen in Figure 4-6 and Figure 4-7. A common feature in the free energy surfaces is that mostly large value of  $\theta$  results in lower value of the free energy due to the adsorption of the chain on to the crystal surface.

Another feature that should be reminded is that the high energy barrier for the  $(20\bar{2})$  face between the two local minima at  $\theta = 87^\circ$  is nonphysical in the sense that all  $\phi$  values that are symmetric with respect to  $\phi = 180^\circ$  are equivalent at  $\theta = 90^\circ$  due to the centrosymmetric structure of adipic acid molecule. Although the free energy difference between all F2-units and the F1-unit can be calculated using methods such as the Finite String Method [Weinan and Ren, 2005; Vanden Eijnden and Venturoli, 2009] as was done by Jion and Rajagopalan [Jion and Rajagopalan, 2014], we simply used a one dimensional free energy surface along the angle  $\theta$ , since the important variations are in this direction.

In the ISA model, there are several parameters that are considered as an external habit controlling factor. Various representations have been given such as in  $C_{l(hkl)}^*$  [Liu et al., 1995; Liu 1999],  $X_{A(hkl)}^{eff}$  [Liu et al., 1995],  $C_{l(hkl)}^*$  and  $t_{hkl}$  [Liu et al., 1996],  $X_{A(hkl)}^{eff}$  and  $C_{l(hkl)}^*$  [Gnanasambandam and Rajagopalan, 2010], or  $\delta_{hkl}$  [Jion and Rajagopalan]. Additionally, the set of  $X_{A(hkl),F1}$  and  $X_{A(hkl),F2}$  could be considered as another possibility, but these values were found to have large relative standard deviations depending on the bin width of the histogram. In this dissertation, we use the representation by  $C_{l(hkl)}^*$  and  $t_{hkl}$ . However, it should be mentioned that any set of two parameters with that encompasses the physical meaning of anisotropic local concentration at the interface and the free energy barrier for reorientation of the growth units is considered adequate.

The surface scaling factor  $C_l^*$  describes the structure of the interface. In a reference state known as the equivalent wetting condition ( $C_l^* = 1$ ), both the solid and liquid have the same structure in the bulk and the interface. For realistic cases, the less-than-equivalent wetting condition ( $C_l^* > 1$ ) indicate a negative adsorption of the solute molecules, while the more-than-equivalent wetting condition ( $C_l^* < 1$ ) indicate a positive adsorption of the solute molecules.  $C_l^*$  is incorporated into the rate expression since its absolute value is directly indicative of the concentration of effective growth units at the interface.

The molecular orientational factor  $t_{hkl}$  represents the free energy barrier for reorientation of the growth units. The reorientation can be considered as a pre-ordering step before being incorporated into a kink site. Spherical particles, such as inorganic crystals, or for cases with relatively weak interactions between solid and fluid units at the interface can reorientate themselves easily which results in the value of  $t_{hkl} \approx 0$ . On the other hand, chain-like molecules such as n-paraffin or complex molecules such as proteins are expected to have higher free energy barrier for reorientation which results in larger values of  $t_{hkl}$ . The overall trends in the  $t_{hkl}$  values were found to closely follow the characteristics of the free energy surface defined by  $\theta$  in the sense that smaller value of  $\theta$  for the F1-units are correlated with higher values of  $t_{hkl}$ .

For the case of adipic acid, it was found that the surface scaling factor values indicates more-than-equivalent wetting condition at all faces. This has the physical meaning of positive adsorption of the growth units on the crystal face. Comparison of the above two external-habit controlling factors shows that (002), (100), and (011) faces have the higher value of both  $C_{l(hkl)}^*$  and  $t_{hkl}$ . This indicates that these faces have both the lower value of local concentration of the effective growth units and free energy barrier for reorientation of the growth units. The  $(10\bar{2})$  face has the value of  $C_{l(hkl)}^*$  similar to that of (011) face and a relatively low value of  $t_{hkl}$  which make this face less likely to appear on the face than the faces with large values of both parameters. The difference is shown visually by the adsorbed molecules in Figure 4-8 where the pre-ordering can be observed on the  $(20\bar{2})$  face whereas the diffuse state of the growth units on the (100) face does not show any sign of such.

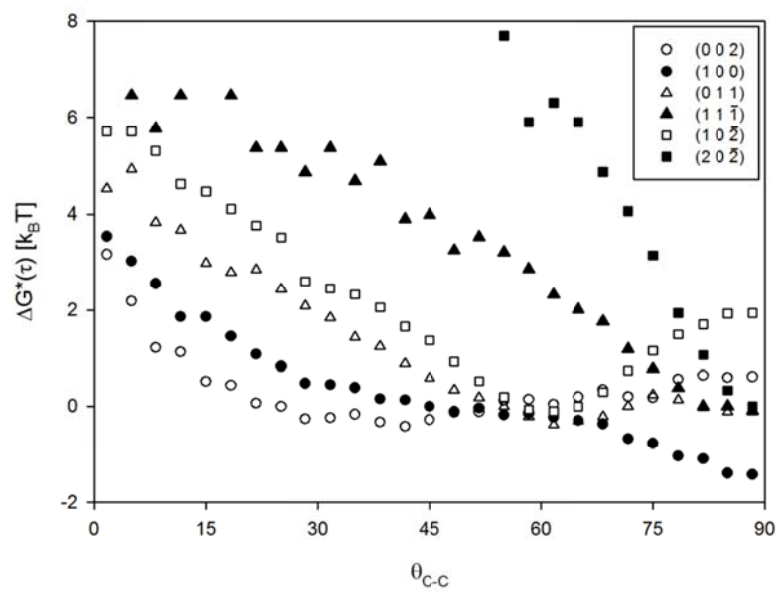
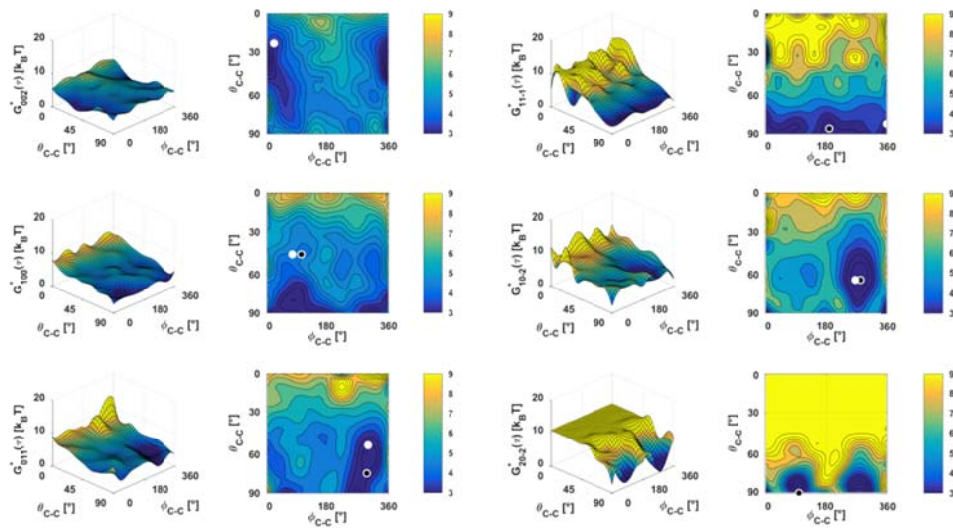


Figure 5-1. Free energy of the adsorbed adipic acid molecules plotted against the angle between the surface normal and C-C backbone of the F2-units.



**Figure 5-2. Free energy of the adsorbed adipic acid molecules plotted against both azimuthal and altitude angles.**

### 5.1.2. Predicted Growth Morphology from Water

There are two conflicting views on the interpretation of the solvent ordering in the interfacial layer [Singh and Banerjee, 2013]. The first view of roughening hypothesis [Bourne and Davey, 1976] expects the favorable solvent interactions to lower the interfacial tension on the crystal face which will roughen the interface to increase the growth rate. In the second view of inhibition model, the adsorbed solvent molecules have to be removed from the kink sites in order for growth units to be incorporated. Earlier works on the adipic acid by Davey and coworkers were in accordance with the second view as they suggest that the adipic acid molecules that approach the (100) face cannot experience the expected H-bonding interactions with the crystal molecule because of the solvent [Davey et al., 1992]. This was one of the main concerns in the earlier works on adipic acid morphology since the strong hydrogen bonds in the [100] direction was related to the low face area of (100) face (~23%) for the calculations from AE model. There was an agreement among the previous works where the experimental morphology was characterized by three faces, on that these faces are characterized as (100), (002), and (011) faces [Klug and Van Mil, 1994; Pfefer and Boistelle, 2000; Keel et al., 2004; Clydesdale, 2005]. According to Pfefer and Boistelle, larger supersaturations change the main faces that are exposed to (100), (011), and  $(10\bar{2})$  [Pfefer and Boistelle, 2000]. Our results coincides with these results in that the morphology calculated by the relative growth rates that accounts for the polygonal spirals show (100), (002), and (011) faces obtained from MD simulations at low supersaturations. This can be related to the higher values of both  $C_{l(hkl)}^*$  and  $t_{hkl}$  of these faces. Therefore, we suggest that the morphology of this crystal can be explained by the anisotropic local concentration at the interface and the free energy barrier for reorientation, in addition to the previously considered molecular bond energetics at the interfaces.

**Table 5-1 External habit-controlling factors obtained from ISA on the F-Faces of adipic acid crystals**

Layer Miller Index	$X_{A(hkl)}$	$\delta_{hkl}$	$X_{A(hkl)}^{eff}$	$\bar{\Phi}_{hkl}^{step}$	$\rho_{hkl}^{kink}$
(002)	0.0380	0.715	0.0271	0.173	0.627
(100)	0.0528	0.580	0.0307	0.966	0.552
(011)	0.0937	0.730	0.0684	0.520	0.607
(11 $\bar{1}$ )	0.143	0.832	0.119	0.703	0.585
(10 $\bar{2}$ )	0.0895	0.760	0.0680	0.413	0.619
(20 $\bar{2}$ )	0.236	0.849	0.200	0.443	0.562

**Table 5-2 Habit-controlling factors and relative growth rates for the F-Faces of adipic acid crystals**

Layer Miller Index	$d_{hkl}$ [Å]	$\xi_{hkl}$	$n_{hkl}$	$C_{l(hkl)}^*$	$t_{hkl}$	$R_{hkl}^{rel,(a)}$	$R_{hkl}^{rel,(b)}$
(002)	4.663	0.0554	4	0.711	0.335	7.61	2.93
(100)	6.695	0.480	6	0.687	0.544	1.00	1.00
(011)	4.499	0.336	6	0.529	0.315	4.36	3.06
(11 $\bar{1}$ )	4.071	0.571	6	0.420	0.184	4.21	3.42
(10 $\bar{2}$ )	4.686	0.266	6	0.530	0.275	6.31	4.07
(20 $\bar{2}$ )	3.339	0.318	4	0.317	0.164	12.0	5.43

(a) using rate expression of Liu et al., 1995

(b) using Equation (97)

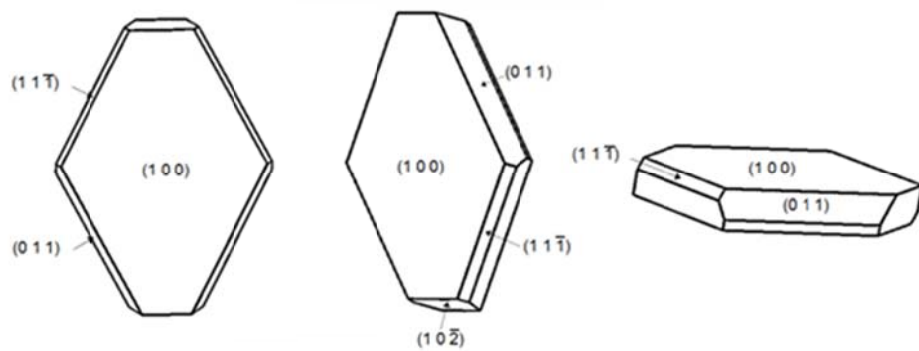


**Figure 5-3. Adipic acid crystal morphology predicted by the original interfacial structure analysis model.**

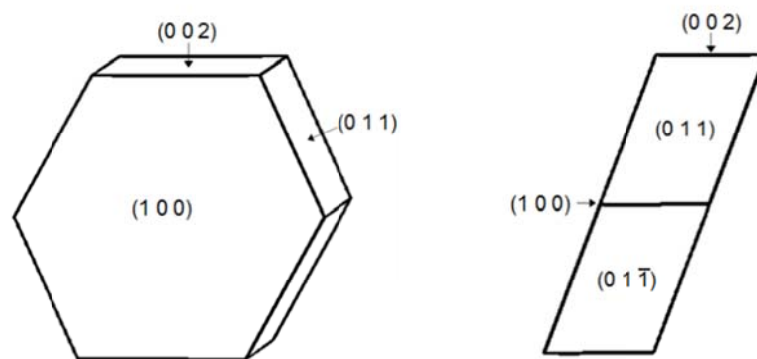


**Figure 5-4. Adipic acid crystal morphology predicted by the modified interfacial structure analysis model.**

## 5.2. Morphology of the $\beta$ -HMX Crystal

### 5.2.1. Conformational Analysis of HMX Molecule

As was mentioned in the previous section, conformation of HMX molecule can be described in various ways. Cremer-Pople puckering coordinates offer an efficient way since the total number of parameters of five is one of the smallest value among that of other analytical methods. However, analyzing and visualizing these parameters are not obvious because of the dimensionality. Evans and Boeyens suggested a mapping of the five-dimensional hyperspace into a three dimensional space by using a set of tori on the surface of a sphere for the conformations of cyclooctane and other molecules with eight-membered ring [Evans and Boeyens, 1988; Allen et al., 1996].

In this approach, the following equations are used to map a set of coordinate  $(\cos\phi_2, \sin\phi_2, q_3\cos\phi_3, q_3\sin\phi_3, \theta)$  by

$$x = [\sin\theta + q_3 \cos\phi_3] \cos\phi_2 \quad (185)$$

$$y = [\sin\theta + q_3 \cos\phi_3] \sin\phi_2 \quad (186)$$

$$z = \cos\theta + q_3 \sin\phi_3 \quad (187)$$

In this representation, the radius from the center of the hole of the center of the torus tube is  $\sin\theta$ , radius of the tube is  $q_3$ .  $\phi_2$  and  $\phi_3$  are the phase angle around the torus.  $q_2$  is tied to others and has is not represented on the tori.

The plot suggested by Evans and Boeyens was applied to the three different conformational families of chair (BC: boat-chair, TBC: twist-boat-chair, C: chair, TC: twist-chair) crown (CR: crown, CC: chair-chair, TCC: twist-chair-chair), and boat (B: boat, BB: boat-boat, TB: twist-boat) [Martin et al., 2010]. One HMX molecule in a solution of 137 acetone molecules (mole fraction of 0.00725) at 313.15 K was prepared. NPT simulations for 10 ns have been performed for different assemblies of charge set, simulation method, and starting conformation. Other simulation details are the same as described in section 4.2.2. Analysis for the boat family using the trajectory from MD simulations starting from boat-boat conformation was executed for first 3 ns, since transition into chair family was observed. For the metadynamics simulation, Cartesian form of the Cremer-Pople puckering coordinates was used as five collective variables. It should be noted that in metadynamics simulations with more than three collective variables, convergence of the free energy surface cannot be assured since the efficiency scales

exponentially and inversely with the dimensionality of the collective variable. In this analysis, metadynamics has been used to explore different regions of the conformational space rather than to deduce the free energy surface.

Several observations can be made on Figure 5-6. Firstly, the effect of different charge sets on the transition of the conformation is significant. The charge set obtained from RESP formalism showed faster transition between the two different families of chair and crown. On the other hand, no transition was observed within the simulation time of 10 ns for simulations using AM1-BCC model. Secondly, metadynamics simulations resulted in larger part of the conformational space within the same simulation time. The effect of the charge set is also significant when the metadynamics simulations using different charge sets are compared. It can be also deduced, as was also mentioned by Martin and coworkers, that the transition of the transition between two crown conformations at the poles are relatively unlikely while the transition between various boat-chair and twist-boat-chair conformations occur more readily.

For Figure 5-7, equivalences of the puckering coordinates have been used to account for the pseudorotations of different conformations. One of the important features is that the two tori obtained from the MD simulations of the chair family are mainly derived from the boat-chair and twist-boat-chair conformations. Chair and twist-chair conformations are supposed to be on the meridian of the sphere. However, using our formulation, the chair conformations lie on the equator where other conformations in the boat family are. Other differences from the chair conformation will be described below. The pseudo rotational pathways for the boat-chair and twist-boat-chair occurs at  $\theta \cong 75, 105$ . The crown family including crown, chair-chair, and twist-chair-chair is placed near both poles in this plot. Difference from previous studies was observed that rather than four tori (or two tori and two points), two hourglasses are formed at the poles. The boat family including boat, boat-boat, and twist-boat lie on the equator of the sphere. Twist-boat is also called saddle (S) in other literatures. The three conformations are not distinguishable on this plot. No significant transition is observed within the boat family. Rather, the symmetry operation revealed that there are four equivalent segments on the equator.

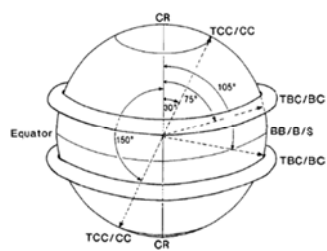


**Figure 5-5. Three-dimensional representation of the five-dimensional conformational space for cyclooctane [Allen et al., 1996]**

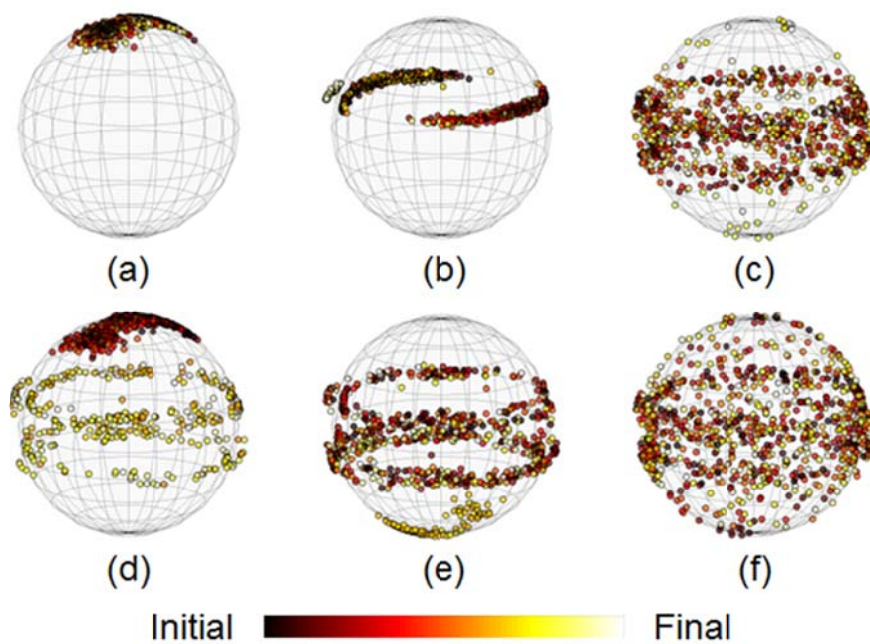


**Figure 5-6. Evans and Boeyens plot of the MD simulations using charge set and starting conformation of (a) AM1-BCC/crown, (b) AM1-BCC/crown, (d) RESP/crown, and (e) RESP/chair and Metadynamics simulations using charge set and starting conformation of (c) AM1-BCC/chair and (f) RESP/chair.**

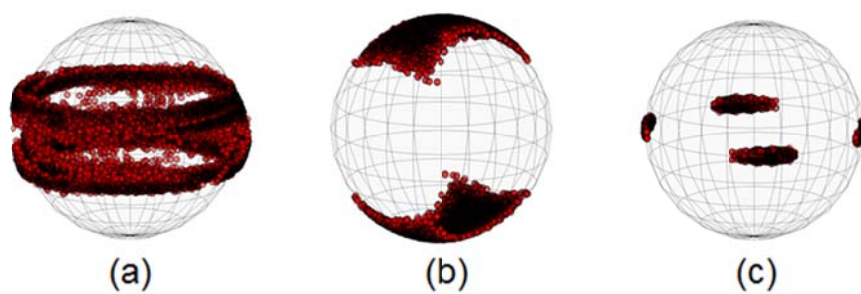


**Figure 5-7. Evans and Boeyens plot of the MD simulations using AM1-BCC charge set and starting conformation of (a) chair, (b) crown, and (c) boat-boat**

Analysis of the various sets from the polar and Cartesian forms of the Cremer-Pople puckering coordinates show that the different conformational groups can be distinguished in various and unobvious ways. The distribution of the polar form Cremer-Pople puckering coordinates are not always obvious because the amplitude values are in the range of  $q_m > 0$ . This results in the asymmetry of the distribution that could be approximated by Gamma distribution. Moreover, for the cases with  $q_m = 0$ , the corresponding phase angle  $\phi_m$  has no meaning. Therefore, all values of  $\phi_m$  are obtained in this case. The equivalent peaks are in both the amplitude (chair and crown families) and phase angle (all families). On the other hand, the distribution of the Cartesian form Cremer-Pople puckering coordinates can be approximated by overlapping Gaussian distributions that can be separated.

From the distributions obtained from the MD simulation of the boat family, it can be deduced that only the starting boat-boat conformation was sampled while other conformations within the family such as the twist-boat or boat conformation was not found during the short simulation run.

The representative phase angles are shown to be effective in reducing the number of peaks for most of the conformations, except for  $\theta$  of crown family which has two distinct values. Although using representative phase angles can be a good solution if identifying one of these conformations is desired, there are many overlaps between different conformations within the range of  $0 < \phi_2 < \pi/4$  and  $0 < \phi_3 < \pi/2$ .

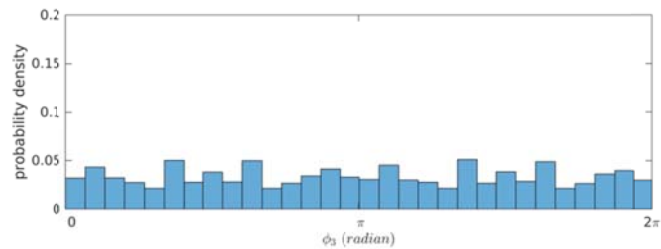
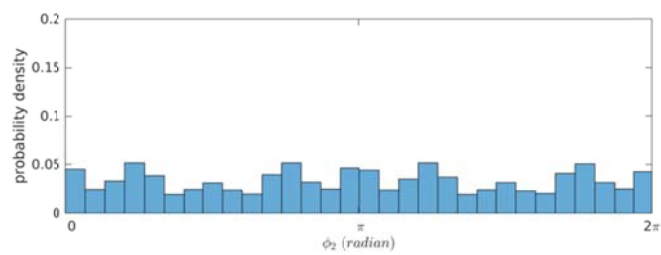
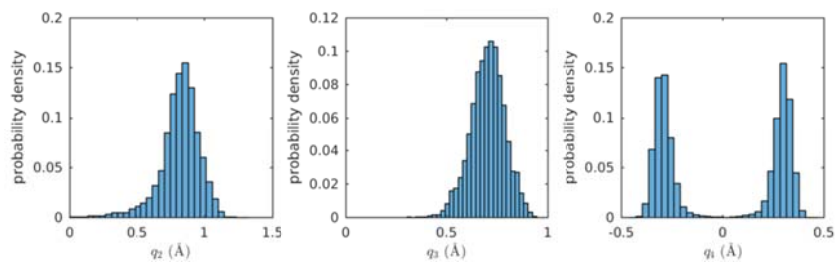


**Figure 5-8. Polar Cremer-Pople puckering coordinates obtained from MD simulation of the chair family.**

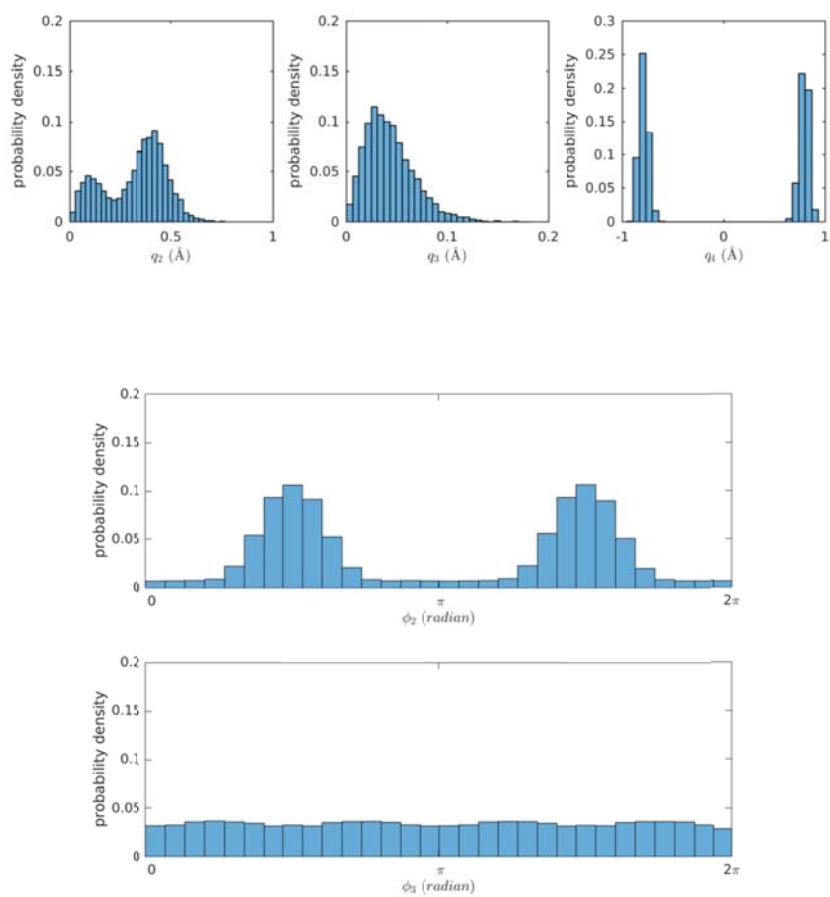


**Figure 5-9. Polar Cremer-Pople puckering coordinates obtained from MD simulation of the crown family.**

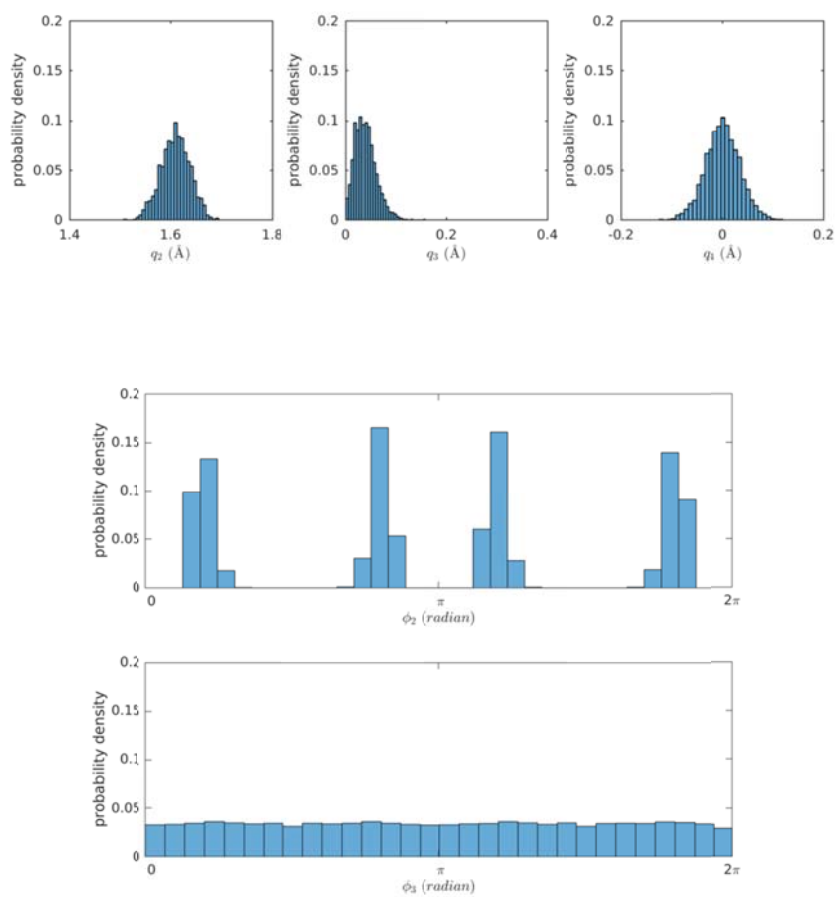


**Figure 5-10. Polar Cremer-Pople puckering coordinates obtained from MD simulation of the boat family.**

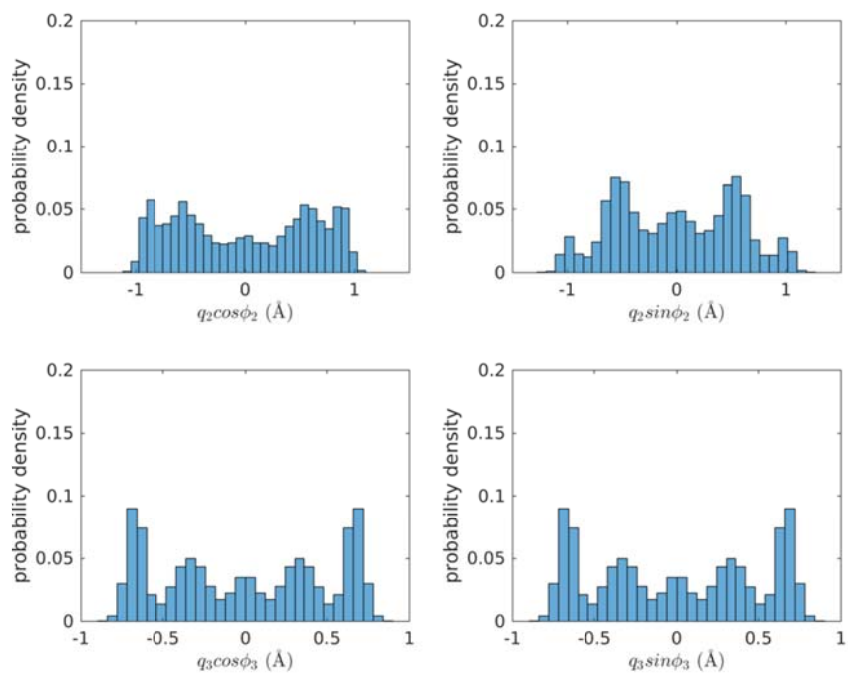


**Figure 5-11. Cartesian Cremer-Pople puckering coordinates obtained from MD simulation of the chair family.**

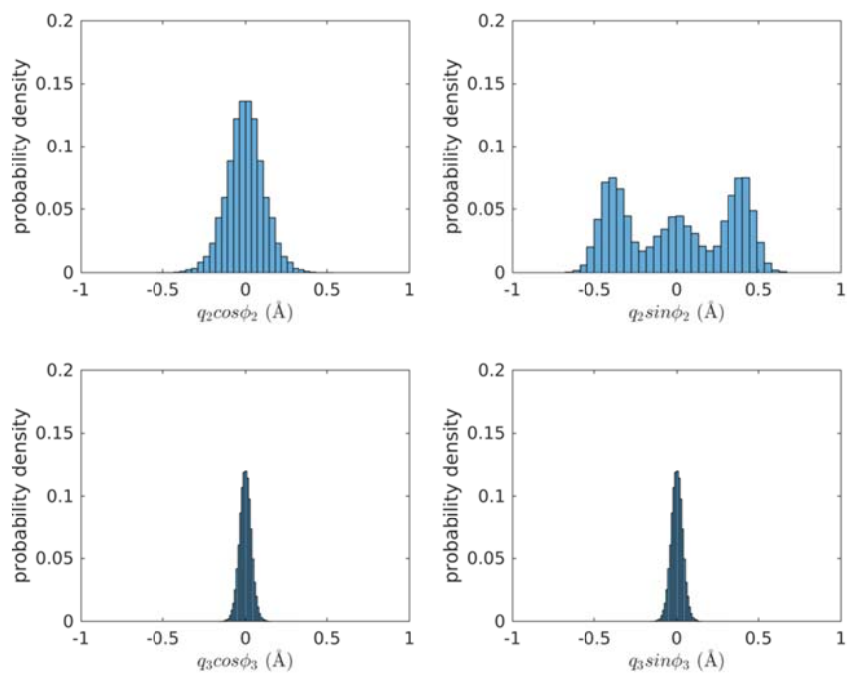


**Figure 5-12. Cartesian Cremer-Pople puckering coordinates obtained from MD simulation of the crown family.**

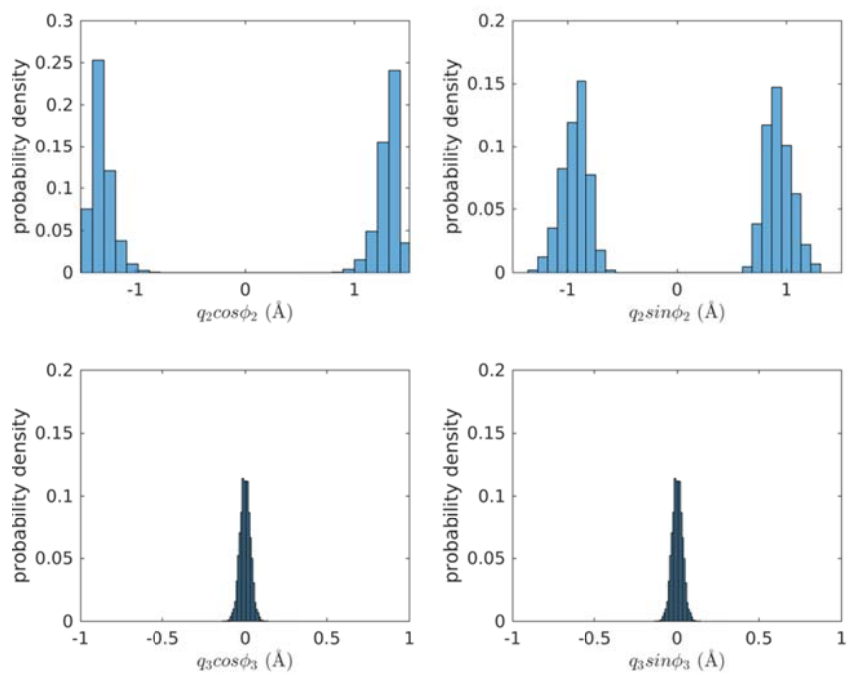


**Figure 5-13. Cartesian Cremer-Pople puckering coordinates obtained from MD simulation of the boat family.**

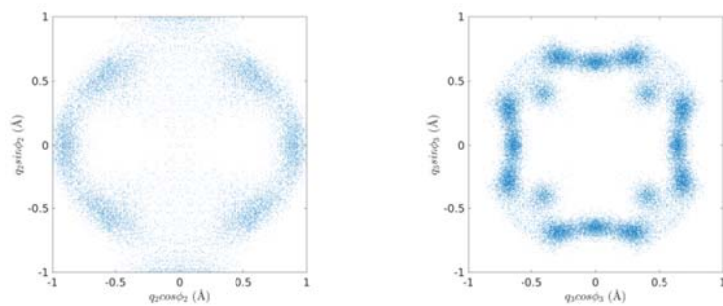


**Figure 5-14. Cartesian Cremer-Pople puckering coordinates for  $m = 2$  and 3 obtained from MD simulation of the chair family.**

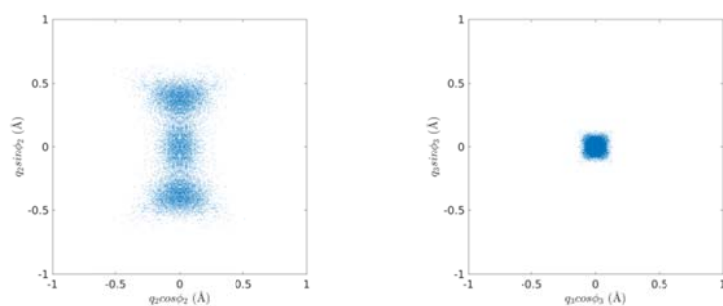


**Figure 5-15. Cartesian Cremer-Pople puckering coordinates for  $m = 2$  and 3 obtained from MD simulation of the crown family.**

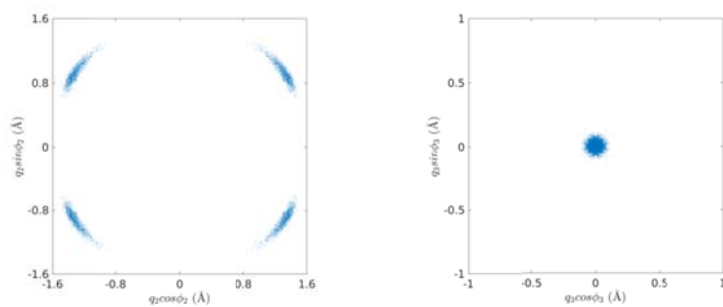


**Figure 5-16. Cartesian Cremer-Pople puckering coordinates for  $m = 2$  and 3 obtained from MD simulation of the boat family.**

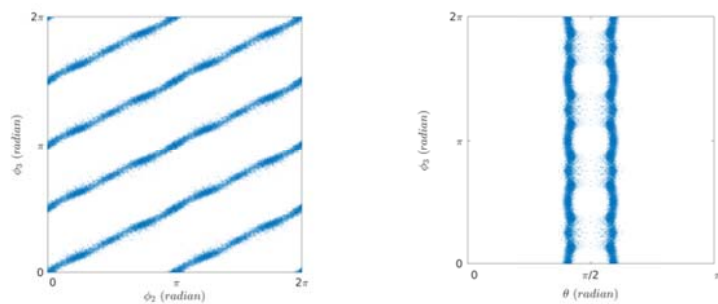


**Figure 5-17. Phase angle components of the polar Cremer-Pople puckering coordinates obtained from MD simulation of the chair family.**

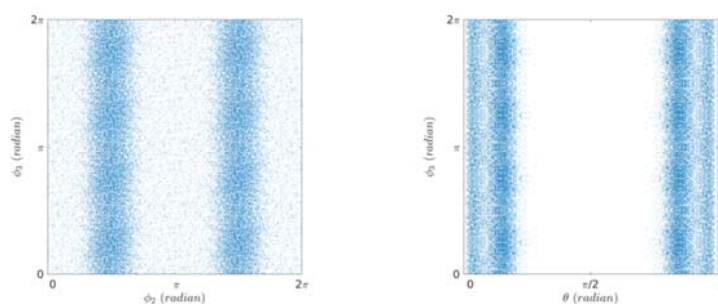


**Figure 5-18. Phase angle components of the polar Cremer-Pople puckering coordinates obtained from MD simulation of the crown family.**

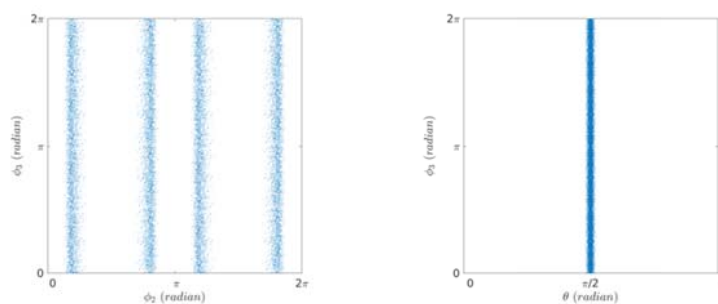


**Figure 5-19. Phase angle components of the polar Cremer-Pople puckering coordinates obtained from MD simulation of the boat family.**

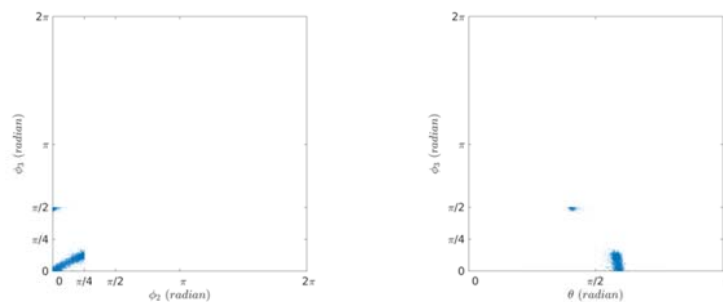


**Figure 5-20. Representative phase angle components of the polar Cremer-Pople puckering coordinates obtained from MD simulation of the chair family.**

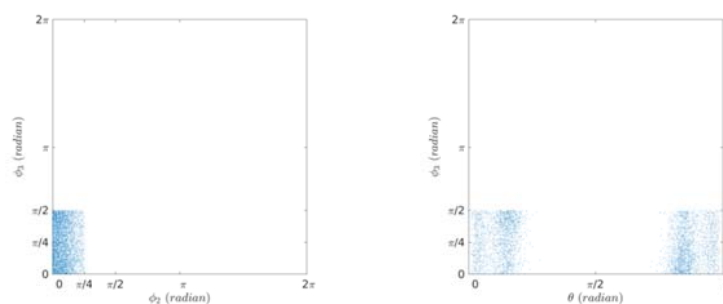


**Figure 5-21. Representative phase angle components of the polar Cremer-Pople puckering coordinates obtained from MD simulation of the crown family.**

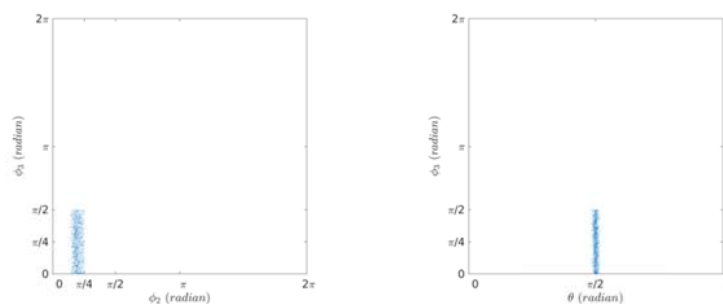


**Figure 5-22. Representative phase angle components of the polar Cremer-Pople puckering coordinates obtained from MD simulation of the boat family.**

The dimensionality of the five-dimensional conformational space described by the Cremer-Pople puckering coordinates can be reduced into lower dimensions using dimensionality reduction methods [Brown et al., 2008; Martin et al., 2010]. Brown, Martin, and their coworkers investigated the dimensionality reduction of the conformational space of cyclooctane and its derivative trans,trans-1,2,4-trifluorocyclo-octane. The ring closure constraints of these molecules with eight-membered ring require that there are only two degrees of freedom in this space. However, analytical descriptions are in much higher dimension as in Cartesian coordinates (72D), dihedral angles (8D), and Cremer-Pople puckering coordinates (5D). Using various dimensionality reduction methods including principal component analysis, Isomap, and autoencoder neural network, embedding in lower dimensions was possible [Brown et al., 2008]. However, analysis of Betti number revealed that the topology of this space is composed of a spherical component and a Klein bottle component. A Klein bottle, which is a nonorientable surface without boundary that can be described by two Möbius strips glued along the edge, cannot be embedded in less than four dimensions. Therefore it was concluded that at least five dimensions are needed to fully capture the characteristics of the cyclooctane conformational space [Martin et al., 2010].

In this work, autoencoder neural network [Hinton and Salakhutdinov, 2006] was used to reduce the dimensionality of the conformational space of HMX. The autoencoder model was built and trained using Keras [Chollet, 2015] library using Theano [Bastien et al., 2012] backend. Eight dihedral angles were used as the input to the autoencoder with the structure of 8-64-64-32-32-3-32-32-64-64-8, where the numbers indicate the number of units in the layer. Training/validation/test sets were comprised of 10000/500/2000 samples. Batch normalization [Ioffe and Szegedy, 2015] was adopted before sigmoid activation. Adadelta optimizer [Zeiler, 2012] was used with a mini batch size of 32. The network was trained for  $10^6$  epochs. Dropout [Srivastava et al., 2014] was not used.

The resulting three-dimensional representation shows that all three conformational families are well separated within this representation. It is also observed that metadynamics simulations explore all three conformational families as well as other intermediate conformations that have not been found in the MD simulations.

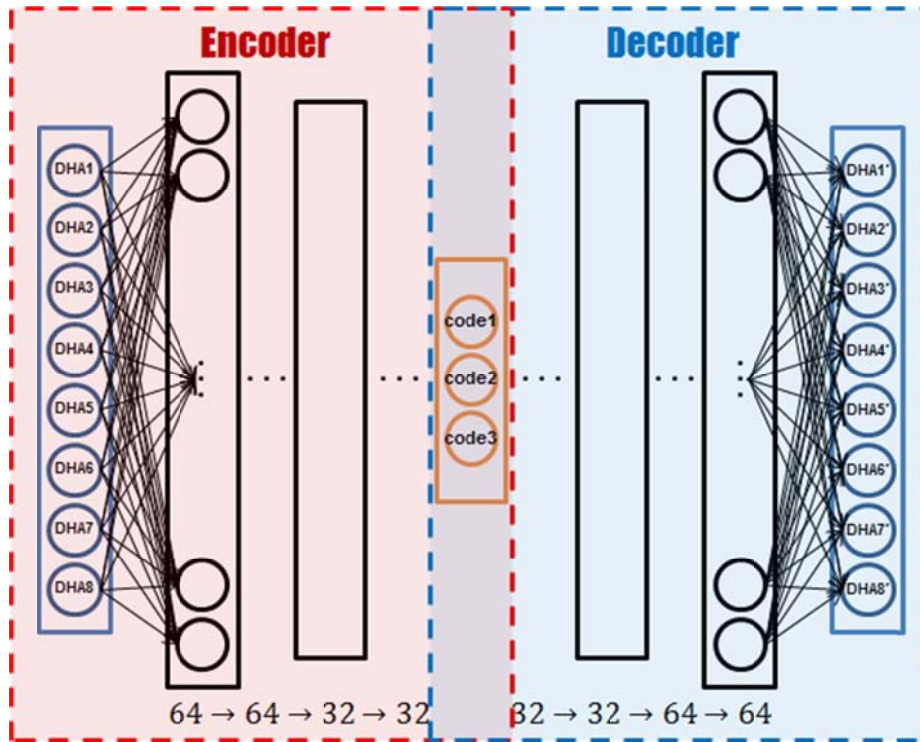


Figure 5-23. Structure of the autoencoder neural network.

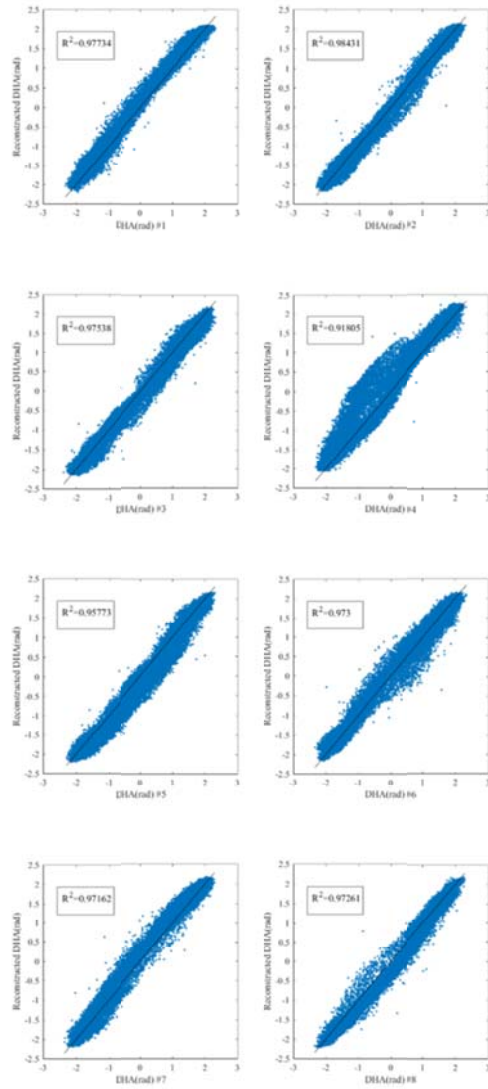


Figure 5-24. Mean squared error of the input and reconstructed data.

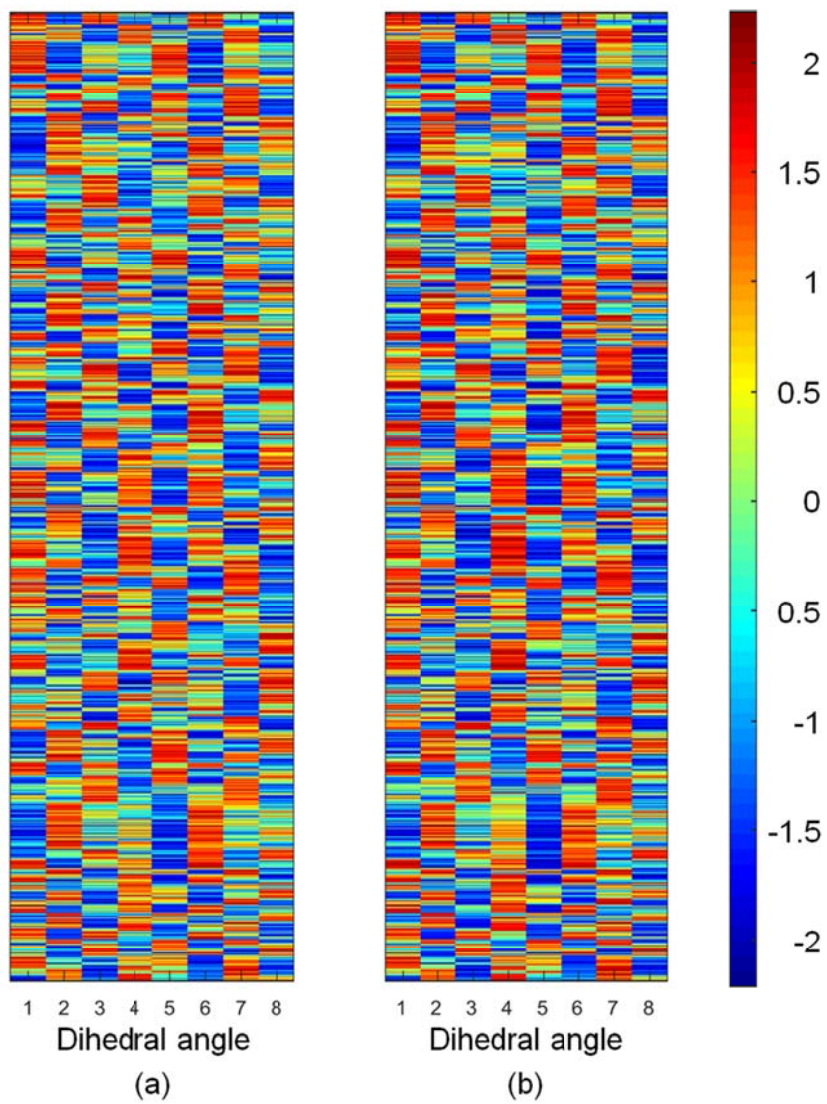
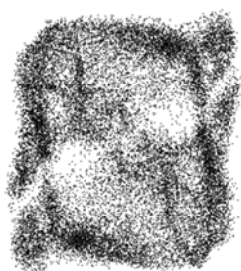


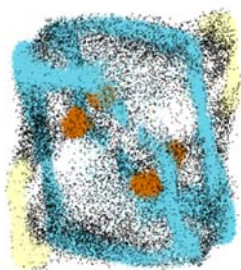
Figure 5-25. Comparison of the (a) input data and (b) reconstructed data in the test set.



(a)



(b)



(c)

**Figure 5-26. A three-dimensional visualization of the conformational space of HMX obtained from (a) MD simulations of ●: chair, ●: crown, and ●: boat families, (b) metadynamics simulations starting from chair conformation, and (c) overlap.**

The F1-unit of the  $\beta$ -HMX crystal has the conformation of chair. However, the MD simulations starting from different conformational families have shown that chair conformation is not found for the free HMX molecule in the acetone solution. In order to analyze the chair conformation of HMX, a method suggested by Santiso and Trout has been used [Santiso and Trout, 2011]. 720 HMX molecules prepared from the unit cell of the  $\beta$ -HMX crystal was cooled to 0 K and 293.15 K using NPT simulation for duration of 100 ps. Other simulation details are the same as described in section 4.2.2. The statistics were obtained from the puckering coordinates of all of the crystal molecules.

For both of the distributions of the polar and Cartesian form Cremer-Pople puckering coordinates of the chair conformation, eight distinct peaks are found. In this work, the Cartesian form was used because all the peaks can easily be approximated with Gaussian distribution in this case. The average values obtained from the simulation at 0 K and the standard deviation values obtained from the simulation at 293.15 K are summarized in Table 5-3. For the chair conformation, the eight peaks are spread in the dimensions of  $q_3 \cos \phi_3$  and  $q_3 \sin \phi_3$ , which is visualized in Figure 5-32.

From these Gaussian distributions, the order parameter for identifying conformation can be defined using Equation (163). A slicing of one of the peaks is shown in Figure 5-37, where the order parameter  $S_1$  is a Gaussian distribution which has the same average and variance but with a peak height of 1.

The representative phase angle for the chair conformation results in 4 different values in the dimension of  $\phi_3$ . Although the number of peaks is reduced to half in this case, the effectiveness is relatively worse than that for other conformations. Therefore, this method has not been used for the order parameter.

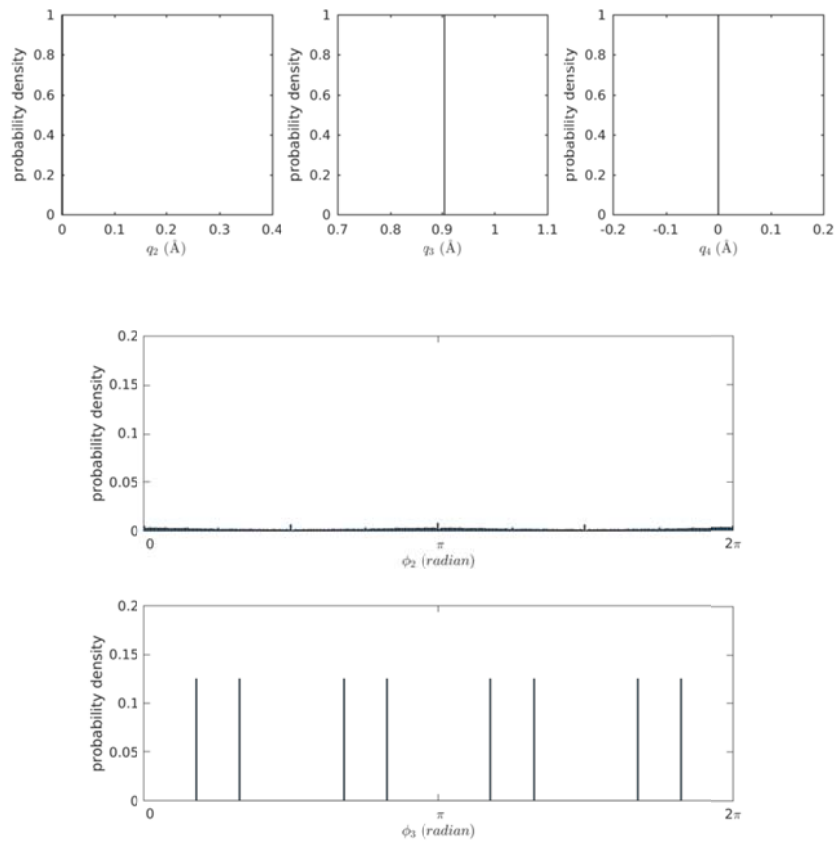


**Figure 5-27. Polar Cremer-Pople puckering coordinates of  $\beta$ -HMX at 0 K.**

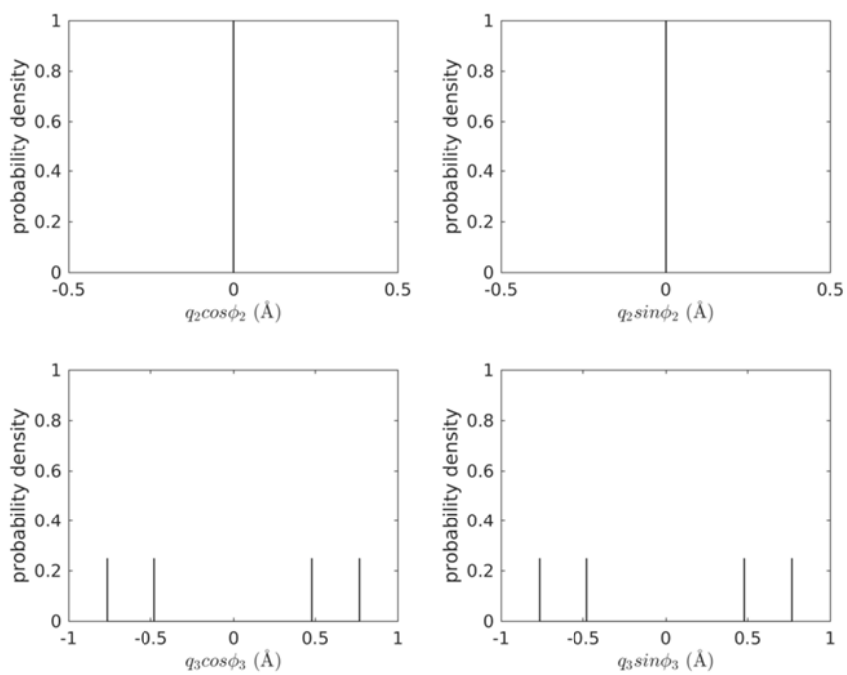


**Figure 5-28. Cartesian Cremer-Pople puckering coordinates of  $\beta$ -HMX at 0 K.**

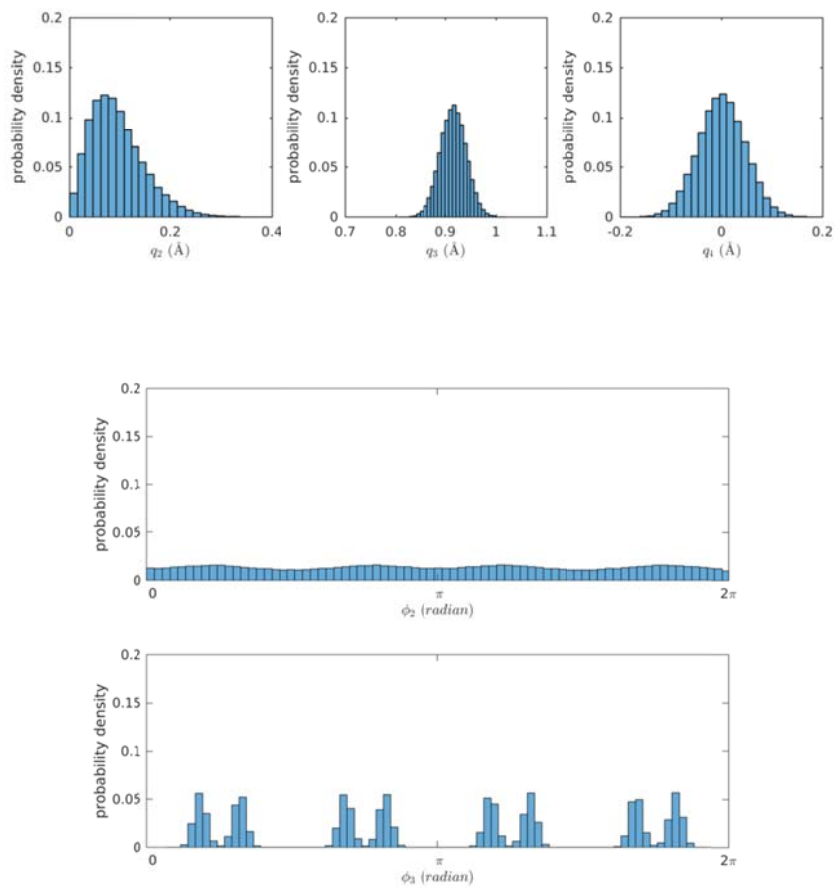


**Figure 5-29. Polar Cremer-Pople puckering coordinates of  $\beta$ -HMX at 293.15 K.**

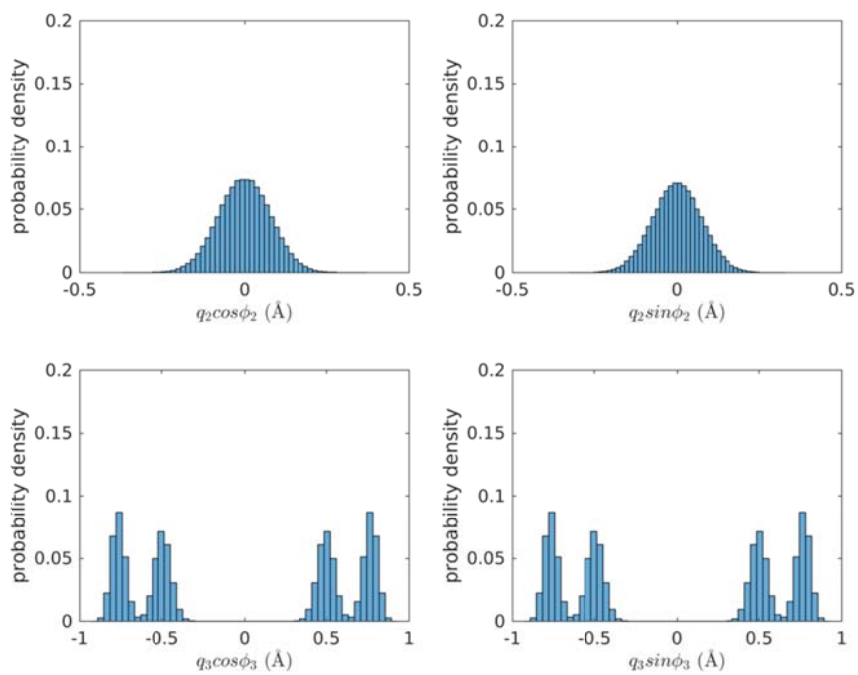


**Figure 5-30. Cartesian Cremer-Pople puckering coordinates of  $\beta$ -HMX at 293.15 K.**

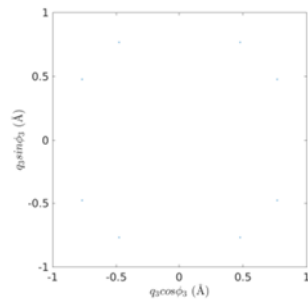


**Figure 5-31. Cartesian Cremer-Pople puckering coordinates of  $\beta$ -HMX for  $m = 3$  at 0 K.**

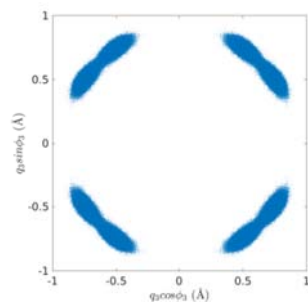


**Figure 5-32. Cartesian Cremer-Pople puckering coordinates of  $\beta$ -HMX for  $m = 3$  at 293.15 K.**

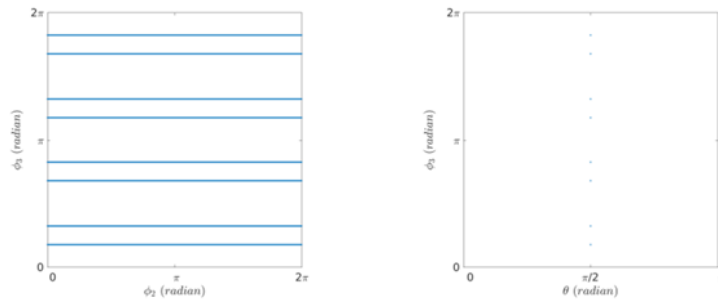


**Figure 5-33. Phase angle components of the polar Cremer-Pople puckering coordinates of  $\beta$ -HMX at 0 K.**

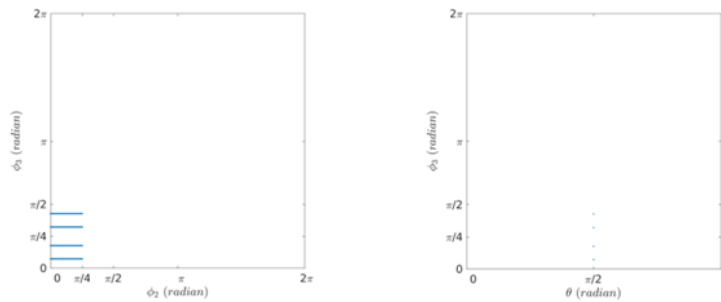


**Figure 5-34. Representative phase angle components of the polar Cremer-Pople puckering coordinates of  $\beta$ -HMX at 0 K.**

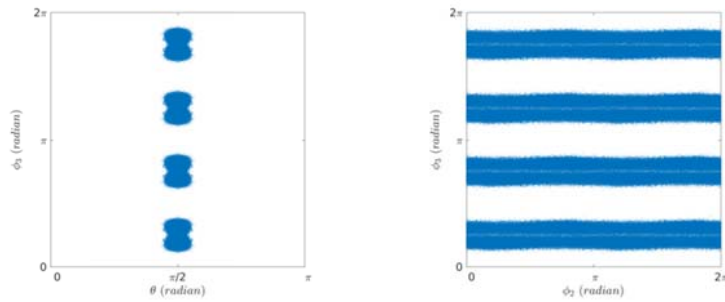


**Figure 5-35. Phase angle components of the polar Cremer-Pople puckering coordinates of  $\beta$ -HMX at 293.15 K.**

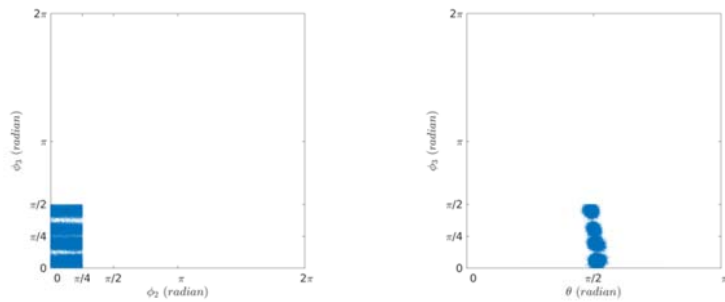


**Figure 5-36. Representative phase angle components of the polar Cremer-Pople puckering coordinates of  $\beta$ -HMX at 293.15 K.**

**Table 5-3 Parameters used for the calculation of the molecular order parameters**

Parameters	Values
$\overline{\text{CP}}_{1,\alpha}, \overline{\text{CP}}_{2,\alpha}, \overline{\text{CP}}_{5,\alpha} [\text{\AA}]^a$	0.00000
$(\overline{\text{CP}}_{3,\alpha}, \overline{\text{CP}}_{4,\alpha}) [\text{\AA}]^a$	$(\pm 0.47800, \pm 0.76736)$ or $(\pm 0.76736, \pm 0.47800)$
$\sigma_{\text{CP}_\alpha} [\text{\AA}]^b$	$(0.078518, 0.074183, 0.040945, 0.050535, 0.046278)$
$\xi_\alpha^b$	211.58

<sup>a</sup> from 0 K MD simulation of a crystal

<sup>b</sup> from 293.15 K MD simulation of a crystal

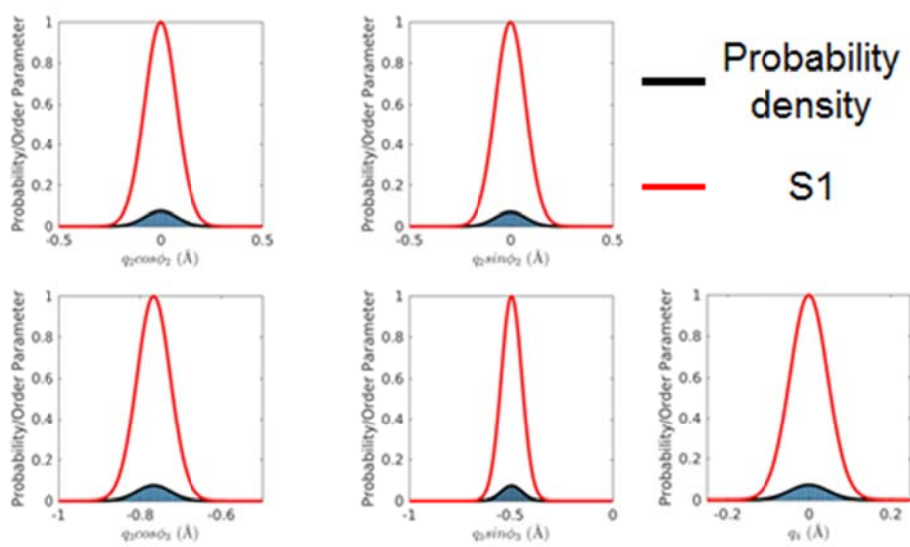


Figure 5-37. Order parameter  $S_1$  defined from the Cremer-Puckering coordinates.

## 5.2.2. Orientational and Conformational Free Energy Surface

In the original ISA models, hand-picked angles are used to derive the orientational free energy surface. For molecules such as HMX, however, too many angles are needed to account for both orientation and conformation. For the orientation, quaternion can be used to reduce the number of parameters, but still require at least 4 set of quaternions for each nitro groups for every asymmetric unit in the unit cell. For the conformation, eight angles are required in the description by dihedral angles. The number can be reduce to five using Cremer-Pople puckering parameter. Our approach of using order parameters can easily identify the correct orientation and conformation of the F1 units using just two parameters which can greatly reduce the dimensionality. The downside of this approach is that all the other states that cannot be identified using these parameters are assumed as in the same state. This can lead to error in the free energy differences if there are any metastable states that have significantly different free energy with respect to the most stable state in solution.

The calculated free energy surface in Figure 5-39 show similar trends for all faces. The monotonic increase and the plateau indicate that a stable F1-unit with the same orientation and conformation as the molecule in crystal does not exist in the interfacial layer. This is different from the adipic acid case in which the orientational free energy is low near the F1-units for most of the faces. The relatively high free energy at  $S_1 = 1$  and  $S_2 = 1$  is more easily seen by using Finite Temperature String method to visualize the free energy barrier in one dimension as in Figure 5-40. For all faces, the disordered state at  $S_1 = 0$  and  $S_2 = 0$  is the most stable and the free energy increases along the possible minimum energy path  $S$ .

Although there is no report on the stability of the chair conformation of HMX in acetone, the relative stability can be presumed from the literature. The potential energy for the gas phase conformations by density functional theory were in the order of boat-chair < chair < boat-boat < crown [Smith and Bharadwaj, 1999; Molt et al., 2013]. This also coincides with our structural optimization at the B3LYP/6-31G(d,p) level for the four low-energy conformers presented by Molt and coworkers, which were boat-boat, chair, chair-chair, and crown, resulting in the chair and crown conformations. But it should be noted that these are potentials calculated for gas phase conformations. On the other hand, the stability can also be presumed from known free energy differences for molecules with similar structure such as the cyclooctane. Martin and others calculated the MM3 potential energy landscapes and transition pathways for three conformational families of crown (CR: crown, CC: chair-chair, TCC: twist-chair-chair), boat (B: boat, BB: boat-boat, TB:

twist-boat), and boat-chair (BC: boat-chair, TBC: twist-boat-chair, C: chair, TC: twist-chair) [Martin et al., 2010]. In their derived potential energy, the chair (C) and boat (B) conformation are transition states. The global minimum corresponds to the boat-chair (BC) conformation which is in the same family with the chair conformation. The boat-chair conformation is more stabilized by clustering with various twist-boat-chair (TBC) conformations in the potential energy surface. The crown (CR) conformation has slightly higher potential energy while boat-boat (BB) and twist-boat (TB) conformations have relatively higher potential energy than the former boat-chair (BC) or crown (CR) conformations. Another related work by Spiwok and Králová showed that it is possible to perform metadynamics for these eight-membered ring molecules by reducing the dimensionality which will enable calculation of the free energy differences [Spiwok and Králová, 2011]. They used path collective variables defined by Isomap projections to calculate the conformational free energy surface of trans,trans,-1,2,4-trifluorocyclooctane in vacuum. The results were similar to that by Martin and coworkers in that the crown (CR) and boat (B) conformations have higher free energies than the boat-chair (BC) conformation. The free energy differences compared to the lowest-energy boat-chair conformation were around 20 kJ/mol for boat and 14 kJ/mol for crown conformation. Since the metadynamics simulation starting from chair conformation of HMX instantaneously converted to boat-chair conformation and circulated between boat-chair, crown, and boat-boat conformations, it seems reasonable to deduce that the chair conformation is unstable in acetone solution near the crystal interface similar to the results obtained by Martin and coworkers or that by Spiwok and Králová. This can be validated by performing metadynamics simulations in the reduced dimensions and calculating the free energy differences between the conformational groups.

The underlying assumption of effective growth units is that the pre-ordering of the F2-units into F1-units occurs before incorporating into kinks. If the F1-units are unstable as in the case of chair conformation of HMX, pre-ordering is not likely to occur. Instead, it can be assumed that all the disordered F2-units undergo similar steps of desolvation and reorientation at the time of incorporation. Therefore the differences in the height of the barrier in Figure 5-39 do not matter under this assumption.

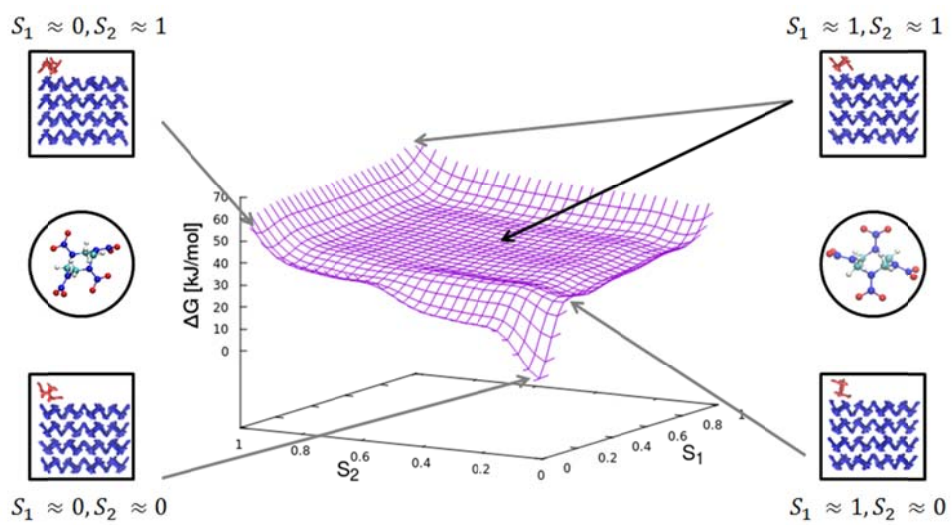
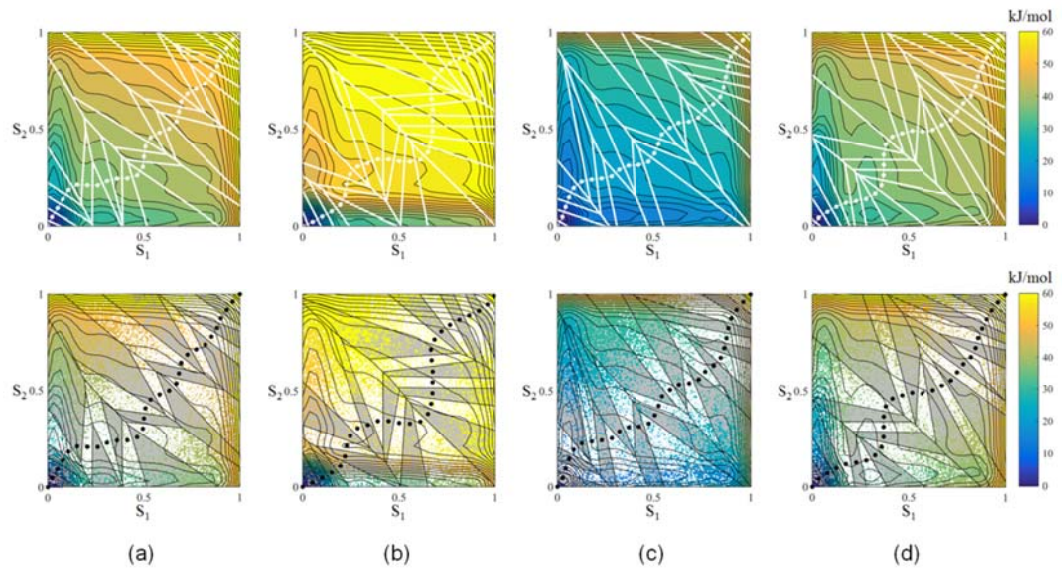
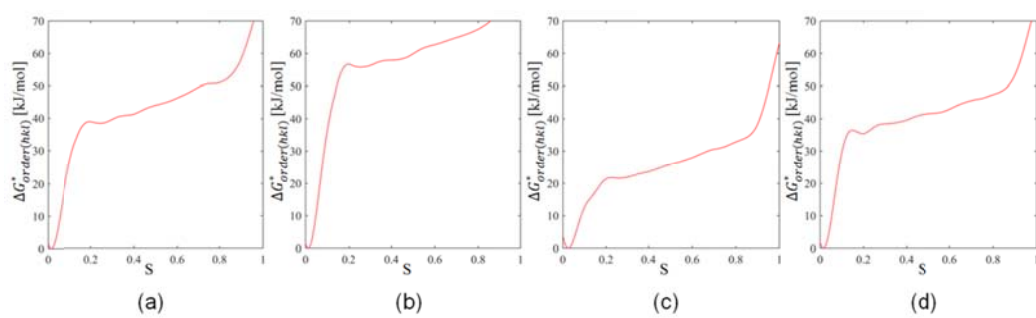


Figure 5-38. Typical free energy surfaces with regard to the order parameters obtained from the metadynamics simulations.



**Figure 5-39. String evolution and transition tube by Finite Temperature String method on the free energy surfaces for (a) (020), (b) (011), (c) (110), and (d) (101) faces**



**Figure 5-40. Free energy along the minimum energy path for the (a) (020), (b) (011), (c) (110), and (d) (101) faces**

### 5.2.3. Predicted Growth Morphology from Acetone

In the ISA models, two external habit-controlling factors are used to represent the local concentrations at the interface and the free energy barriers for pre-ordering of the growth units. As was mentioned in Section 5.1.1, these two factors can be expressed with  $C_{h(hkl)}^*$  and  $t_{hkl}$ . If all the F2-units at the interface are assumed equivalent due to the instability of F1-units, the value of  $t_{hkl}$  has to be 0 which is equivalent to  $\delta_{hkl} = 1$  and  $X_{A(hkl)}^{eff} = X_{A(hkl)}$ .

The experimental morphology from evaporative crystallization can be found in the literature [Duan et al., 2010; Zhang et al., 2013; Gallagher et al., 2014; Shim and Koo, 2014; Gallagher et al., 2017]. The crystals obtained from the evaporative crystallizations are usually polyhedron surrounded by large (011) or (020) face. The (110) face is usually present but the existence of the (101) face is not clear since they are sometimes absent.

In this dissertation, Gas Anti-Solvent (GAS) method is used to crystallize  $\beta$ -HMX from acetone solution. The same method has been attempted by Teipel and coworkers to obtain particles with the size of about 65  $\mu\text{m}$  [Teipel et al., 1999]. The particles had truncated octahedron morphology that is similar to the case of evaporative crystallization. In a GAS process, the supersaturation is created by mixing the carbon dioxide antisolvent with the solvent. The prepared solution is placed inside the crystallizer using solution pump before the antisolvent is introduced. Then the antisolvent is introduced by a high pressure pump (model: HKS-12000, Hanyang Accuracy, Republic of Korea) into the crystallizer from below passing through the pre-cooler, high pressure pump, and preheater. The purpose of the pre-cooler is to avoid cavitation in the line while that of the preheater is to control the temperature of the antisolvent. The pre-cooler is connected to a refrigerated bath circulator (model: RBC-20, JEIO TECH, Republic of Korea) and cooled at 259 K. The crystallizer and preheater are connected to a heating bath circulator (model: RW-1040G, Lab Companion, USA). The antisolvent is continuously introduced to increase the pressure up to a desired value which is maintained by two back-pressure regulators (model: 26-1700, TESCO, USA). After the pressure is met, the solution is stirred and dried with fresh antisolvent for a desired amount of time. Lastly, the pressure is lowered and the crystals are collected at the membrane filter (FLUOROPORE<sup>TM</sup>, membrane filters 0.45  $\mu\text{m}$  FH, Millipore, Ireland). The operating conditions of the GAS process crystallization are summarized in Table 5-4. The obtained particles had average particle size  $D_{50}$  of 12.90  $\mu\text{m}$ . The XRD patterns confirm the polymorph form of the crystal as  $\beta$ .

The resulting morphology obtained from the generalized ISA model shows morphology similar to that reported by Shim and Koo. The morphology also

closely resembles the experimental morphology except for the absence of the (101) face in the latter. This resemblance can be interpreted that the effect of anisotropic local concentration of the growth units at the interface is the dominant external habit-controlling factor for  $\beta$ -HMX crystal.

It should be noted, however, that the assumption of  $t_{hkl} = 0$  was put forward because of the instability of the chair conformation in the interfacial layer. For the more general case, accurate value of the desolvation free energy barrier  $\Delta G_{desolv}^*$  (or  $\Delta G_{kink}^*$  in the original ISA nomenclature) is needed in order to compare it with the orientational and conformational free energy barrier  $\Delta G_{order}^*$ . Although the original ISA model and further studies assumed the value of  $\Delta G_{desolv}^*$  as close to the thermal fluctuation,  $k_B T$  [Liu et al., 1995; Gnanasambandam and Rajagopalan, 2010], Vekilov suggested that this could be as high as 28 kJ/mol for the enthalpy part (near zero for the entropy part) [Vekilov, 2007; De Yoreo, 2001]. Accurate determination of this value will be a key factor in order to evaluate the effects of orientational and conformational free energy barriers in the interfacial layer.

**Table 5-4 Operating conditions for the GAS process**

Operation Parameter	Value
Temperature [K]	303
Pressure [bar]	100
Solution concentration [wt%]	2.17
Amount of acetone [mL]	20
Antisolvent addition rate [ml/min]	200
Agitation rate [rpm]	900
Drying time [min]	30

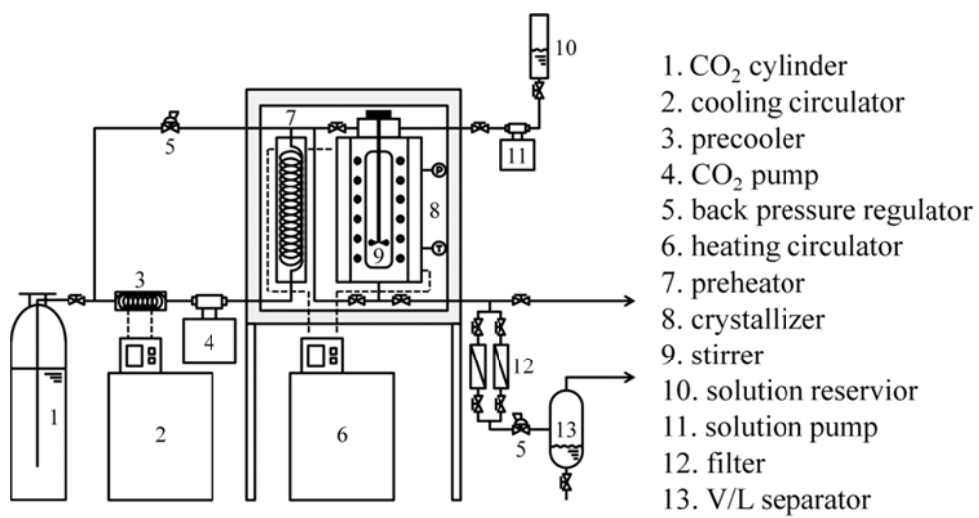


Figure 5-41 Schematic diagram of the GAS process apparatus

**Table 5-5 External habit-controlling factors obtained from ISA on the F-Faces of adipic acid crystals**

Layer Miller Index	$X_{A(hkl)}$	$\delta_{hkl}$	$X_{A(hkl)}^{eff}$	$\bar{\Phi}_{hkl}^{step}$	$\rho_{hkl}^{kink}$
(020)	0.05100	1	0.05100	0.3338	0.5889
(011)	0.05611	1	0.05611	0.2398	0.6114
(110)	0.05596	1	0.05596	0.1967	0.6216
(101)	0.07347	1	0.07347	0.2430	0.6107

**Table 5-6 Habit-controlling factors and relative growth rates for the F-Faces of  $\beta$ -HMX crystals**

Layer Miller Index	$d_{hkl}$ [Å]	$\xi_{hkl}$	$n_{hkl}$	$C_{l(hkl)}^*$	$t_{hkl}$	$R_{hkl}^{rel}$
(020)	5.518	0.4438	4	0.6038	0	0.865
(011)	6.021	0.4940	6	0.5845	0	1.00
(110)	5.515	0.4048	6	0.5850	0	1.13
(101)	4.318	0.3682	4	0.5298	0	1.39

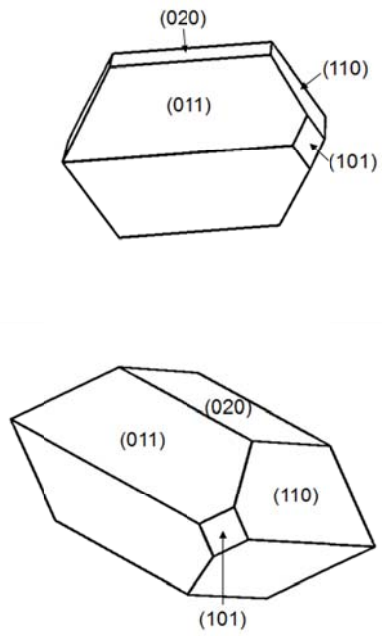
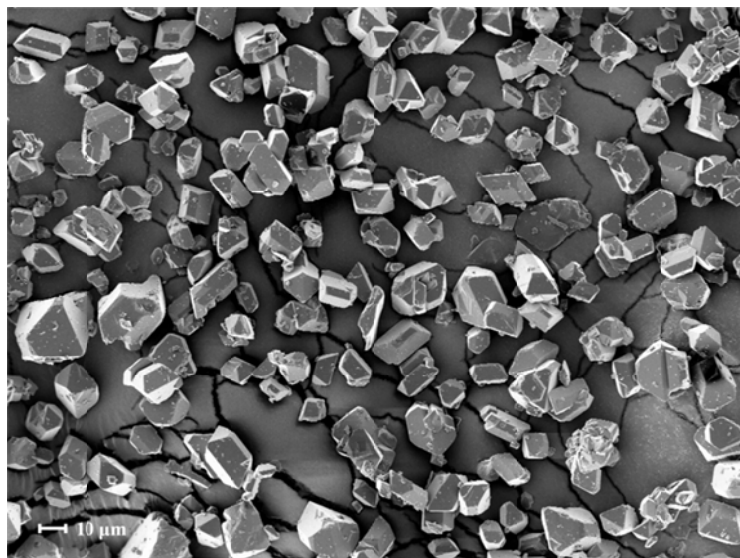


Figure 5-42.  $\beta$ -HMX crystal morphology predicted by the generalized interfacial structure analysis model.



**Figure 5-43. Morphology of the  $\beta$ -HMX crystal obtained by using GAS process.**

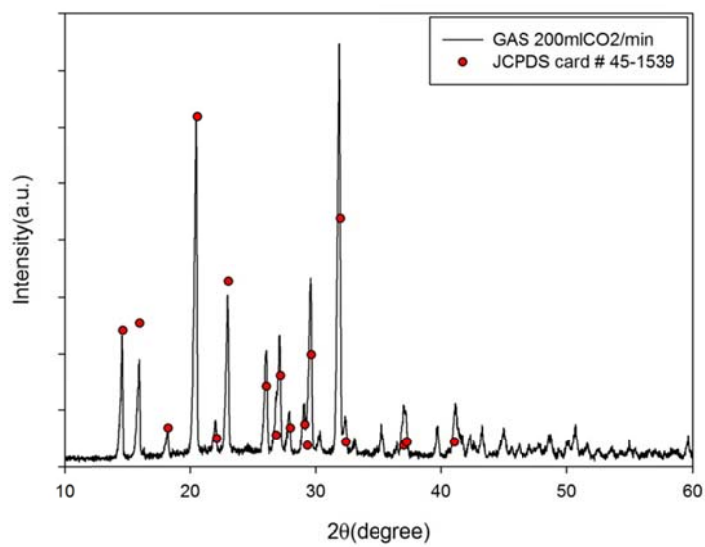
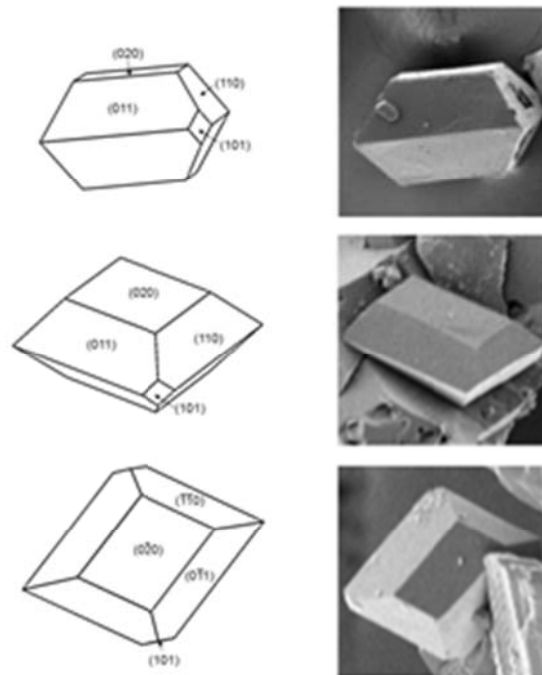


Figure 5-44. XRD pattern of the  $\beta$ -HMX crystal obtained by using GAS process.



**Figure 5-45. Comparison of the predicted morphology with the experimentally obtained  $\beta$ -HMX crystal morphology at various angles.**

## Chapter 6. Conclusion

In this dissertation, the morphology of crystals comprised of two well-known centrosymmetric growth units have been elucidated using the ISA model. This model has the attractive feature of being able to handle the local concentration of the growth units at the interface and reorientation free energy barrier related to the orientation and conformation. The significance of this model was that it brought a breakthrough in modeling the crystal morphology with a mechanistic view. However, there are some concepts that have to be revised for this model to be applied to various types of crystals. The concepts presented here have been generalization of the original model to account for both orientation and conformation of the growth units. As was suggested in the former researches on the same topic, the way to overcome the high dimensionality of the free energy surface becomes an important issue. String methods and enhanced sampling methods with appropriate collective variables have been suggested so far, but other innovative dimensionality reduction methods can play significant roles in this sense.

For both of the crystals investigated, integration of the spiral geometry and spiral rotation time resulted in significantly better resemblance to the experimental morphologies compared to the results obtained by using the original assumption of simple isotropic concentric spirals. On the other hand, the conformational free energy barrier of ring-containing molecules is expected to have larger effect than orientational free energy barrier because of the relative heights of the barriers. However, assumption of neglecting the effect of conformational differences based on the fact that crystal-like F1-unit is a transition state in the interface layer resulted in a good agreement with the experimental morphology. Such factors imply that our better understanding of the crystal growth phenomena is crucial in order to construct better models for morphology prediction.

Therefore, more rigorous descriptions are required for the less well-defined concepts such as the height of the desolvation free energy barrier, importance of surface diffusion, as well as those already well-defined concepts in other approaches such as asymmetric spiral geometries, non-centrosymmetric growth units, and transition to two-dimensional nucleation growth in order to provide an accurate prediction of the crystal morphology which can be considered as a harbinger of the crystal growth.

## Bibliography

Allen, F. H.; Howard, J. A. K.; Pitchford, N. A.; Symmetry-Modified Conformational Mapping and Classification of the Medium Rings from Crystallographic Data. IV. Cyclooctane and Related Eight-Membered Rings. *Acta Crystallographica* **1996**, *B52*, 882-891.

Atkins, P., de Paula, J. *Physical Chemistry* 8th ed.; Oxford University Press: UK, 2006.

Barducci, A.; Bussi, G.; Parrinello, M. Well-tempered metadynamics: a smoothly converging and tunable free-energy method. *Physical Review Letters* **2008**, *100*, 020603.

Bastien, F.; Lamblin, P.; Pascanu, R.; Bergstra, J.; Goodfellow, I.; Bergeron, A.; Bouchard, N.; Warde-Farley, D.; Bengio, Y. Theano: new features and speed improvements. *arXiv preprint arXiv:1211.5590* **2012**.

Bayly, C.; Cieplak, P.; Cornell, W.; Kollman, P. A well-behaved electrostatic potential based method using charge restraints for deriving atomic charges: the RESP model. *The Journal of Physical Chemistry* **1993**, *97*, 10269-10280.

Berendsen, H. J. C.; Postma, J. P. M.; van Gunsteren, W. F.; DiNola, A.; Haak, J. R. Molecular dynamics with coupling to an external bath. *The Journal of Chemical Physics* **1984**, *81*, 3684-3690.

Berendsen, H. J. C.; van der Spoel, D.; van Drunen, R. GROMACS: A message-passing parallel molecular dynamics implementation. *Computer Physics Communications* **1995**, *91*, 43-56.

Bergh, M.; Caleman, C. A Validation Study of the General Amber Force Field Applied to Energetic Molecular Crystals. *Journal of Energetic Materials* **2016**, *34*, 62-75.

Bernstein, J. *Polymorphism in Molecular Crystals*; Oxford University Press: USA, 2002.

Bonomi, M.; Barducci, A.; Parrinello, M. Reconstructing the Equilibrium Boltzmann Distribution from Well-Tempered Metadynamics. *Journal of Computational Chemistry* **2009**, *30*, 1616-1621.

Bourne, J. R.; Davey, R. J. The role of solvent-solute interactins in determining crystal growth mechanisms from solution: I. The surface entropy factor. *Journal of Crystal Growth* **1976**, *36*, 278-286.

Bourne, J. R.; Davey, R. J. The role of solvent-solute interactins in determining crystal growth mechanisms from solution: II. The growth kinetics of hexamethylene tetramine. *Journal of Crystal Growth* **1976**, *36*, 287-296.

- Bravais, A.; Études cristallographiques; Gauthier-Villars: Paris, 1866.
- Brown, W. M.; Martin, S.; Pollock, S.; Coutsiias, E. A.; Watson, J.-P. Algorithmic dimensionality reduction for molecular structure analysis. *The Journal of Chemical Physics* **2008**, *129*, 064118.
- Bruns, E. A.; Greaves, J.; Finlayson-Pitts, B. J. Measurement of Vapor Pressures and Heats of Sublimation of Dicarboxylic Acids Using Atmospheric Solids Analysis Probe Mass Spectrometry. *The Journal of Physical Chemistry A* **2012**, *116*, 5900–5909.
- Burton, W. K.; Cabrera, N.; Frank, F. C. The growth of crystals and the equilibrium structure of their surfaces. *Philosophical Transactions of the Royal Society A* **1951**, *243*, 299–358.
- Bussi, G.; Donadio, D.; Parrinello, M. Canonical sampling through velocity rescaling. *The Journal of Chemical Physics* **2007**, *126*, 014101.
- Cabrera, N.; Levine, M. M. On the dislocation theory of evaporation of crystals. *Philosophical Magazine* **1956**, *1*, 450–458.
- Chen, L.-Z.; Zhang, J.; Wang, W.-Y.; Diao, Y. Solubility of  $\beta$ -HMX in Acetone + Water Mixed Solvent Systems at Temperatures from 293.15 K to 313.15 K. *Journal of Solution Chemistry* **2012**, *41*, 1265-1270.
- Cheong, D.; Boon, Y. D. Comparative Study of Force Fields for Molecular Dynamics Simulations of  $\alpha$ -Glycine Crystal Growth from Solution. *Crystal Growth & Design* **2010**, *10*, 5146-5158.
- Chernov, A. A. The Kinetics of the Growth Forms of Crystals, *Soviet Physics, Crystallography* **1963**, *7*, 728-730.
- Chernov, A. A.; *Modern Crystallography III. Crystal Growth*; Springer-Verlag: Berlin, 1984.
- Chernov, A. A.; De Yoreo, J.; Rashkovich, L. N.; Vekilov, P. G. Step and Kink Dynamics in Inorganic and Protein Crystallization. *MRS Bulletin* **2004**, *29*, 927-934.
- Choi, C. S.; Boutin, H. P. A study of the crystal structure of  $\beta$ -cyclotetramethylene tetranitramine by neutron diffraction. *Acta Crystallographica* **1970**, *B26*, 1235–1240.
- Chollet, F. keras; <http://keras.io>. 2015.
- Chow, K. Y.; Go, J.; Mehdizadeh, M.; Grant, D. J. W. Modification of adipic acid crystals: influence of growth in the presence of fatty acid additives on crystal properties. *International Journal of Pharmaceutics* **1984**, *20*, 3–24.

Clydesdale, G.; Thomson, G. B.; Walker, E. M.; Roberts, K. J.; Meenan, P.; Docherty, R. A Molecular Modeling Study of the Crystal Morphology of Adipic Acid and Its Habit Modification by Homologous Impurities. *Crystal Growth & Design* **2005**, *5*, 2154–2163.

Connolly, M. L. Solvent-accessible surfaces of proteins and nucleic acids. *Science* **1983**, *221*, 709-713.

Cornell, W. D.; Cieplak, P.; Bayly, C. I.; Gould, I. R.; Merz, K. M.; Ferguson, D. M.; Spellmeyer, D. C.; Fox, T.; Caldwell, J. W.; Kollman, P.A. A second generation force field for the simulation of proteins, nucleic acids, and organic molecules. *Journal of the American Chemical Society* **1995**, *117*, 5179-5197.

Cremer, D.; Pople, J. A. A General Definition of Ring Puckering Coordinates. *Journal of the American Chemical Society* **1975**, *97*, 1354-1358.

Darden, T.; York, D.; Pedersen, L. Particle mesh Ewald: An  $N \cdot \log(N)$  method for Ewald sums in large systems. *The Journal of Chemical Physics* **1993**, *98*, 10089–10092.

Davey, R. J.; Black, S. N.; Logan, D.; Maginn, S. J.; Fairbrother, J. E.; Grant, D. J. W. Structural and Kinetic Features of Crystal Growth Inhibition : Adipic Acid Growing in the Presence of n-Alkanoic Acids. *Journal of the Chemical Society, Faraday Transactions* **1992**, *88*, 3461–3466.

Deschamps, J. R.; Frisch, M.; Parrish, D. CCDC 792930: Experimental Crystal Structure Determination, 2014.

De Yoreo, J. J. In 13th International Conference on Crystal Growth; Hibiya, T., Mullin, J. B., Uwaha, M., Eds.; Elsevier: Kyoto, Japan, 2001.

Donnay, J. D. H.; Harker, D. A new law of crystal morphology extending the law of Bravais. *American Mineralogist* **1937**, *22*, 446-467

Duan, X; Wei, C.; Liu, Y.; Pei, C. A molecular dynamics simulation of solvent effects on the crystal morphology of HMX. *Journal of Hazardous Materials* **2010**, *174*, 175-180.

Dupradeau F.-Y.; Pigache, A.; Zaffran, T.; Savineau, C.; Lelong, R.; Grivel, N.; Lelong, D.; Rosanski, W.; Cieplak, P. The R.E.D. tools: advances in RESP and ESP charge derivation and force field library building. *Physical Chemistry Chemical Physics* **2010**, *12*, 7821-7839.

Eisenhaber, F.; Lijnzaad, P.; Argos, P.; Sander, C.; Scharf, M. The double cubic lattice method: Efficient approaches to numerical integration of surface area and volume and to dot surface contouring of molecular assemblies. *Journal of Computational Chemistry* **1995**, *16*, 273-284.

- Evans, D. G.; Boeyens, J. C. A. Mapping the Conformation of Eight-Membered Rings. *Acta Crystallographica* **1988**, *B44*, 663-671.
- Fairbrother, J. E.; Grant, D. J. The crystal habit modification of a tablet lubricant, adipic acid *Journal of Pharmacy and Pharmacology* **1978**, *30*, 19.
- Frank, F. C. The influence of dislocations on crystal growth. *Discussions of the Faraday Society* **1949**, *5*, 48-54.
- Frank, F. C. On the Kinematic Theory of Crystal Growth and Dissolution Processes. In *Growth and Perfection of Crystals*; Doremus, R. H., Roberts, B. W., Turnbull, D., Eds.; Wiley: New York, 1958.
- Frenkel, J. On the surface motion of particles in crystals and the natural roughness of crystalline faces. *Journal of Physics-USSR* **1945**, *9*, 392-398.
- Friedel, M. G. Études Sur la loi de Bravais. *Bulletin de la Société française de Minéralogie* **1907**, *9*, 326-455.
- Gaivoronskii, A. N.; Granzhan, V. A. Solubility Adipic acid in Organic Solvents and Water. *Russian Journal of Applied Chemistry* **2005**, *78*, 404-408.
- Gallagher, H. G.; Sherwood, J. N.; Vrcelj, R. M. Growth and Dislocation studies of  $\beta$ -HMX. *Chemistry Central Journal* **2014**, *8*, 75.
- Gallagher, H. G.; Sherwood, J. N.; Vrcelj, R. M. The growth and perfection of bicyclic tetramethylene-tetranitramine (HMX) studied by laboratory and synchrotron X-ray topography. *Journal of Crystal Growth* **2017**, *475*, 192-201.
- Gibbs, J. W. On the equilibrium of heterogeneous substances. *American Journal of Science and Arts* **1878**, *16*, 441-458.
- Giberti, F.; Salvalaglio, M.; Mazzotti, M.; Parrinello, M. Insight into the nucleation of urea crystals from the melt. *Chemical Engineering Science* **2015**, *121*, 51-59.
- Gilli, G. Molecules and Molecular Crystals. In *Fundamentals of Crystallography*; C. Giacovazzo, Ed.; Oxford University Press: Oxford, 1992.
- Gnanasambandam, S.; Rajagopalan, R. Growth morphology of  $\alpha$ -glycine crystals in solution environments: an extended interface structure analysis. *CrystEngComm* **2010**, *12*, 1740-1749.
- Gordon, M. S.; Schmidt, M. W. Advances in electronic structure theory: GAMESS a decade later. In *Theory and Applications of Computational Chemistry: the first forty years*; Dykstra, C. E., Frenking, G., Kim, K. S., Scuseria, G. E., Eds; Elsevier: Amsterdam, 2005.
- Hartman, P.; Perdok, W. G. On the relations between structure and morphology of crystals. I *Acta Crystallographica* **1955**, *8*, 49-52.

- Hartman, P.; Bennema, P. The attachment energy as a habit controlling factor: I Theoretical considerations. *Journal of Crystal Growth* **1980**, *49*, 145–156.
- Herring, C. Some Theorems on the Free Energies of Crystal Surfaces. *Physical Review* **1951**, *82*, 87-93.
- Hess, B.; Kutzner, C.; van der Spoel, D.; Lindahl, E. GROMACS 4: Algorithms for Highly Efficient, Load-Balanced, and Scalable Molecular Simulation. *Journal of Chemical Theory and Computation* **2008**, *4*, 435-447.
- Hinton, G. E.; Salakhutdinov, R. R. Reducing the Dimensionality of Data with Neural Network. *Science* **2006**, *313*, 504-507.
- Housty, J.; Hospital, M. Localisation des Atomes d'Hydrogène dans l'Acide Adipique COOH[CH<sub>2</sub>]<sub>4</sub>COOH. *Acta Crystallographica* **1965**, *18*, 693–697.
- Hwang, K. C.; Sagadevan, A. One-pot room-temperature conversion of cyclohexane to adipic acid by ozone and UV light. *Science* **2014**, *346*, 1495–1498.
- Ioffe, S.; Szegedy, C.; Batch normalization: accelerating deep network training by reducing internal covariate shift. *Proceedings of the 32nd International Conference on International Conference on Machine Learning* **2015**, *37*, 448-456.
- Jion, A. I.; Rajagopalan, R. On the study of crystal growth via interfacial analysis and string optimization. *CrystEngComm* **2014**, *16*, 6224-6233.
- Kaischew, R.; Stranski, I. N. Zur Theorie der linearen Kristallisationsgeschwindigkeit. *Zeitschrift für Physikalische Chemie* **1934**, *170A*, 295-299.
- Kaischew, R.; Budevski, E. Surface processes in electrocrystallization *Contemporary Physics*. **1967**, *8*, 489-516.
- Kaischew, R. The Molecular-Kinetic Theory of Crystal Growth. In *Growth of Crystals*, Shubnikov, A. V.; Sheftal, N. N., Eds.; Consultants Bureau: New York, 1962, Vol. 3.
- Kaminsky, W. WinXMorph: a computer program to draw crystal morphology, growth sectors and cross sections with export files in VRML V2.0 utf8-virtual reality format. *Journal of Applied Crystallography* **2005**, *38*, 566–567.
- Keel, T. R.; Thompson, C.; Davies, M. C.; Tendler, S. J. B.; Roberts, C. J. AFM studies of the crystallization and habit modification of an excipient material, adipic acid. *International Journal of Pharmaceutics* **2004**, *280*, 185–198.
- Kessler, M.; Perez, J. Equivalence properties of the Cremer & Pople puckering coordinates for N-membered rings. *Journal of Mathematical Chemistry* **2012**, *50*, 187-209.

Kim, S. H.; Dandekar, P.; Lovette, M. A.; Doherty, M. F. Kink Rate Model for the General Case of Organic Molecular Crystals. *Crystal Growth & Design* **2014**, *14*, 2460-2467.

Kittel, C. *Introduction to Solid State Physics*, 8th ed.; John Wiley & Sons, Inc.: USA, 2005.

Klug, D. L.; Van Mil, J. H. (E. I. Du Pont de Nemours and Company, USA). Adipic Acid Purification. US Patent 5,296,639. March 22, 1994.

Kossel, W. Zur Theorie des Kristallwachstums. *Nachrichten von der Gesellschaft der Wissenschaften zu Göttingen, Mathematisch-Physikalische Klasse* **1927**, *206*, 135-143.

Kuvadia, Z. B.; Doherty, M. F. Spiral Growth Model for Faceted Crystals of Non-Centrosymmetric Organic Molecules Grown from Solution. *Crystal Growth & Design* **2011**, *11*, 2780-2802.

Laio, A.; Parrinello, M. Escaping free-energy minima. *Proceedings of the National Academy of Sciences* **2002**, *49*, 12562-12566.

Li, J.; Tilbury, C. J.; Joswiak, M. N.; Peters, B.; Doherty, M. F. Rate Expressions for Kink Attachment and Detachment During Crystal Growth. *Crystal Growth & Design* **2016**, *16*, 3313-3322.

Lindahl, E.; van der Spoel, D.; Hess, B. GROMACS 3.0: a package for molecular simulation and trajectory analysis. *Journal of Molecular Modeling* **2001**, *7*, 306-317.

Liu, X. Y.; Boek, E. S.; Briels, W. J.; Bennema, P. Analysis of morphology of crystals based on identification of interfacial structure. *The Journal of Chemical Physics* **1995**, *403*, 3747-3754.

Liu, X. Y.; Boek, E. S.; Briels, W. J.; Bennema, P. Prediction of crystal growth morphology based on structural analysis of the solid-fluid interface. *Nature* **1995**, *374*, 342-345.

Liu, X. Y.; Bennema, P. An inhomogeneous cell model and the growth of crystals. *Journal of Crystal Growth* **1996**, *166*, 112-116.

Liu, X. Y.; Bennema, P. Prediction of the growth morphology of crystals. *Journal of Crystal Growth* **1996**, *166*, 117-123.

Liu, X. Y. Modeling of the fluid-phase interfacial effect on the growth morphology of crystals. *Physical Review B* **1999**, *60*, 2810-2817.

Lovette, M. A.; Doherty, M. F. Reinterpreting edge energies calculated from crystal growth experiments. *Journal of Crystal Growth* **2011**, *327*, 117-126.

- Lovette, M. A.; Doherty, M. F. Predictive Modeling of Supersaturation-Dependent Crystal Shapes. *Crystal Growth & Design* **2012**, *12*, 656-669.
- Lovette, M. A.; Doherty, M. F. Multisite models to determine the distribution of kink sites adjacent to low-energy edges. *Physical Review E* **2012**, *85*, 021604.
- Markov, I. V. *Crystal Growth for Beginners, Fundamentals of Nucleation, Crystal Growth and Epitaxy* 2nd ed.; World Scientific: Singapore, 2003.
- Martin, S.; Thompson, A.; Coutsiaris, E.; Watson, J.-P. Topology of cyclo-octane energy Landscape. *The Journal of Chemical Physics* **2010**, *132*, 234115.
- Michaels, A. S.; Colville, A. R.; The effect of surface active agents on crystal growth rate and crystal habit. *The Journal of Physical Chemistry*, **1960**, *64*, 13-19.
- Michaels, A. S.; Tausch, F. W. Modification of growth rate and habit of adipic acid crystals with surfactants. *The Journal of Physical Chemistry* **1961**, *65*, 1730-1737.
- Molt, R. W.; Watson, T.; Bazanté, A. P.; Bartlett, R. J. The great diversity of HMX conformers: probing the potential energy surface using CCSD(T). *The Journal of Physical Chemistry A* **2013**, *117*, 3467–3474.
- Mullin, J. *Crystallization* 4th ed.; Butterworth-Heinemann: UK, 2001.
- Myerson, A. S.; Jang, S. M. A comparison of binding energy and metastable zone width for adipic acid with various additives. *Journal of Crystal Growth*, **1995**, *156*, 459-466.
- Nielsen, A. E. *Kinetics of Precipitation*; Pergamon Press: Oxford, 1964.
- Nosé, S.; Klein, M. L. Constant pressure molecular dynamics for molecular systems. *Molecular Physics* **1983**, *50*, 1055–1076.
- Ohara, M., and Reid R. C. *Modeling Crystal Growth Rates from Solution*; Prentice-Hall: Englewood Cliffs, NJ, 1973.
- Owen, D. K.; Wendt, R. C. Estimation of the Surface Free Energy of Polymers. *Journal of Applied Polymer Science* **1969**, *13*, 1741-1747.
- Parrinello, M.; Rahman, M. Polymorphic transitions in single crystals: A new molecular dynamics method. *Journal of Applied Physics* **1981**, *52*, 7182–7190.
- Pfefer, G.; Boistelle, R. Theoretical morphology of adipic acid crystals. *Journal of Crystal Growth* **2000**, *208*, 615–622.
- Qian, W.; Zhang, C.; Xiong, Y.; Zong, H.; Zhang, W.; Shu, Y. Thermal expansion of explosive molecular crystals: anisotropy and molecular stacking. *Central European Journal of Energetic Materials* **2014**, *11*, 59–81.

Salvalaglio, M.; Vetter, T.; Giberti, F.; Mazzotti, M.; Parrinello, M. Uncovering Molecular Details of Urea Crystal Growth in the Presence of Additives. *Journal of the American Chemical Society* **2012**, *134*, 17221-17233.

Salvalaglio, M.; Vetter, T.; Mazzotti, M.; Parrinello, M. Controlling and Predicting Crystal Shapes: The Case of Urea. *Angewandte Chemie International Edition* **2013**, *52*, 13369-13372.

Santiso, E. E.; Trout, B. L. A general set of order parameters for molecular crystals. *The Journal of Chemical Physics* **2011**, *134*, 064109.

Schmidt, M. W.; Baldrige, K. K.; Boatz, J. A.; Elbert, S. T.; Gordon, M. S.; Jensen, J. H.; Koseki, S.; Matsunaga, N.; Nguyen, K. A.; Su, S.; Windus, T. L.; Dupuis, M.; Montgomery J. A. General Atomic and Molecular Electronic Structure System. *Journal of Computational Chemistry* **1993**, *14*, 1347-1363.

Singh, M. K.; Banerjee, A. Role of Solvent and External Growth Environments to Determine Growth Morphology of Molecular Crystals, *Crystal Growth & Design*, **2013**, *13*, 2413-2425.

Shim, H.-M.; Koo, K.-K. Prediction of Growth Habit of  $\beta$ -Cyclotetramethylenetetranitramine Crystals by the First-Principles Models. *Crystal Growth & Design* **2015**, *15*, 3983-3991.

Shim, H.-M.; Myerson, A. S.; Koo, K.-K. Molecular Modeling on the Role of Local Concentration in the Crystallization of L-Methionine from Aqueous Solution. *Crystal Growth & Design*, **2016**, *16*, 3454-3464.

Shim, H.-M.; Koo, K.-K. Molecular Approach to the Effect of Interfacial Energy on Growth Habit of  $\epsilon$ -HNIW. *Crystal Growth & Design* **2016**, *16*, 6506-6513.

Smith, G. D.; Bharadwaj, R. K. Quantum Chemistry Based Force Field for Simulations of HMX. *The Journal of Physical Chemistry B* **1999**, *103*, 3570-3575.

Snyder, R. C.; Doherty M. F. Predicting crystal growth by spiral motion. *Proceedings of the Royal Society of London A* **2009**, *465*, 1145-1171.

Song, X.; Wang, Y.; An, C.; Guo, X.; Li, F. Dependence of particle morphology and size on the mechanical sensitivity and thermal stability of octahydro-1,3,5,7-tetranitro-1,3,5,7-tetrazocine. *Journal of Hazardous Materials* **2008**, *159*, 222-229.

Spiwok, V.; Králová, B. Metadynamics on the conformational space nonlinearly dimensionally reduced by Isomap. *The Journal of Chemical Physics* **2011**, *135*, 224504.

van der Spoel, D.; Lindahl, E.; Hess, B.; Groenhof G.; Mark, A. E.; Berendsen, H. J. C. GROMACS: Fast, flexible, and free. *Journal of Computational Chemistry* **2005**, *26*, 1701-1718.

Srivastava, N.; Hinton, G.; Krizhevsky, A.; Sutskever, I.; Salakhutdinov, R. Dropout: A Simple Way to Prevent Neural Networks from Overfitting. *Journal of Machine Learning Research* **2014**, *15*, 1929-1958.

Steinhardt, P.; Nelson, D.; Ronchetti, M. Bond-orientational order in liquids and glasses. *Physical Review B* **1983**, *28*, 784-805.

Stewart, J. J. P. Optimization of parameters for semiempirical methods V: modification of NDDO approximations and application to 70 elements. *Journal of Molecular Modeling* **2007**, *13*, 1173-1213.

Stranski, I. N. Zur Theorie des Kristallwachstums. *Zeitschrift für Physikalische Chemie* **1928**, *136U*, 259-278.

Strauss, H. L.; Pickett, H. M. Conformational structure, energy, and inversion rates of cyclohexane and some related oxanes. *Journal of the American Chemical Society* **1970**, *92*, 7281-7290.

Suren, S.; Sunsandee, N.; Stolcova, M.; Hronec, M.; Leepipatpiboon, N.; Pancharoen, U.; Kheawhom, S. Measurement on the solubility of adipic acid in various solvents at high temperature and its thermodynamics parameters. *Fluid Phase Equilibria* **2013**, *360*, 332-337.

Teipel, U.; Förter-Barth, U.; Krause, H. H. Crystallization of HMX-Particles by Using the Gas Anti-Solvent Process, *Propellants, Explosives, Pyrotechnics* **1999**, *24*, 195-198.

Teng, H. H.; Dove, P. M.; Orme, C. A.; De Yoreo, J. J. Thermodynamics of calcite growth: baseline for understanding biomineral formation. *Science* **1998**, *282*, 724-727.

Thiel, W. The MNDOC method, a correlated version of the MNDO model. *Journal of the American Chemical Society*, **1981**, *103*, 1413-1420.

Tilbury, C. J.; Green, D. A.; Marshall, W. J.; Doherty, M. F. Predicting the Effect of Solvent on the Crystal Habit of Small Organic Molecules. *Crystal Growth & Design* **2016**, *16*, 2590-2604.

Tilbury, C. J.; Doherty, M. F. Modeling Layered Crystal Growth at Increasing Supersaturation by Connecting Growth Regimes. *AIChE Journal* **2017**, *63*, 1338-1352.

Tribello, G. A.; Bonomi, M.; Branduardi, D.; Camilloni, C.; Bussi, G. PLUMED 2: New feathers for an old bird. *Computer Physics Communications* **2014**, *185*, 604-613.

Vanden-Eijnden, E.; Venturoli, M. Revisiting the finite temperature string method for the calculation of reaction tubes and free energies. *The Journal of Chemical Physics* **2009**, *130*, 194103.

Vekilov, P. G. What determines the rate of growth of crystals from solution? *Crystal Growth & Design* **2007**, *7*, 2796-2810.

Volmer, M.; Marder, M. Zur Theorie der linearen Kristallisationsgeschwindigkeit unterkühlte Schmelzen und unterkühlter fester Modifikationen. *Zeitschrift für Physikalische Chemie* **1931**, *154A*, 97-112.

Voronkov, V. V. Dislocation mechanism of growth with a low kink density. *Soviet Physics Crystallography* **1973**, *18*, 19–23.

Wang, J.; Wolf, R. M.; Caldwell, J. W.; Kollman, P. A.; Case, D. A. Development and testing of a general amber force field. *Journal of Computational Chemistry* **2004**, *25*, 1157–1174.

Weinan, E.; Ren, W.; Vanden-Eijnden, E. Finite Temperature String Method for the Study of Rare Events. *The Journal of Physical Chemistry B* **2005**, *109*, 6688-6693.

Winn, D.; Doherty, M. F. A New Technique for Predicting the Shape of Solution-Grown Organic Crystals. *AIChE Journal* **1998**, *44*, 2501–2514.

Winn, D.; Doherty, M. F. Modeling Crystal Shapes of Organic Materials Grown from Solution. *AIChE Journal* **2000**, *46*, 1348–1367.

Wulff, G. Zur Frage der Geschwindigkeit des Wachstums und der Auflösung der Krystallflächen. *Zeitschrift für Kristallographie* **1901**, *34*, 449-530.

Zamiri, A. R.; De, S. Multiscale modeling of the anisotropic shock response of  $\beta$ -HMX. molecular polycrystals. *Interaction and Multiscale Mechanics* **2011**, *4*, 139-153.

Zeiler, M. D. ADADELTA: an adaptive learning rate method. *arXiv preprint arXiv:1212.5701* **2012**

Zhang, C.; Ji, C.; Li, H.; Zhou, Y.; Xu, J.; Xu, R.; Li, J.; Luo, Y. Occupancy Model for Predicting the Crystal Morphologies Influenced by Solvents and Temperature, and Its Application to Nitroamine Explosives. *Crystal Growth & Design* **2013**, *13*, 282-290.

Zhu, W.; Xiao, J.; Ji, G.; Zhao, F.; Xiao, H. First-Principles Study of the Four Polymorphs of Crystalline Octahydro-1,3,5,7-tetranitro-1,3,5,7-tetrazocine. *The Journal of Physical Chemistry B* **2007**, *111*, 12715-12722.

## Notes

Parts of this dissertation have been included in

Seo, B.; Kim, T.; Kim, S.; Ryu, J.; Ryu, J. Yoon, J.; Lee, W. B.; Lee, Y.-W.  
Interfacial Structure Analysis for the Morphology Prediction of Adipic Acid  
Crystals from Aqueous Solution. *Crystal Growth & Design*, **2017**, *17*, 1088-1095.

and

Seo, B.; Kim, S.; Lee, M.; Kim, T.; Kim, H.; Lee, W. B.; Lee, Y.-W.  
Prediction of the Crystal Morphology of  $\beta$ -HMX using a Generalized Interfacial  
Structure Analysis Model. **2018**, *Manuscript submitted for publication*.

## 요약

# 계면 구조 분석 모델을 통한 중심 대칭성 분자의 결정 형상 예측

서울대학교 대학원  
화학생물공학부  
서범준

결정은 제약, 방위, 식품, 전자, 에너지 등 다양한 분야의 산업에서 중요한 소재로 활용되는데, 그 소재의 성능은 결정의 구조, 크기, 크기 분포, 형상, 순도 등 성질들에 의해 좌우된다. 이러한 결정의 성질들은 대부분 결정화 공정에서 바뀌기 때문에 결정화 공정을 통해 얻어지는 결정의 성질을 예측하고 조절하는 과정은 공정의 최적화에 있어 필수적이다. 결정의 성질 중에서 형상은 특히 용해 속도, 생체이용률, 반응 속도 등의 효능이나 유동성, 습윤성 등의 공정 효율처럼 다양한 부분에 영향을 주기 때문에 이를 예측하는 연구가 활발히 이루어져 왔다. 결정화 공정에서 결정의 형상에 영향을 주는 요소는 내부 요소와 외부 요소로 구분되는데, 내부 요소는 결정 구조, 결정 내 상호작용 등이 있으며 외부 요소는 용매, 온도, 과포화도 등이 있다. 결정의 형상을 예측하기 위해 초기에는 Bravais-Friedel-Donnay-Harker 모델이나 Attachment Energy 모델 등이 이용되었다. 이 두 가지 모델은 오직 내부 요소만을 고려하기 때문에 외부 요소의 작용이 작은 기상 결정화에는 적합하지만 외부 요소의 작용이 큰 용액 결정화에는 적합하지 않다. 따라서 용액 결정화로부터 얻어지는 형상을 예측하기 위해 외부 요소를 포함한 구체적인 결정 성장 과정이 반영된 이차원 핵생성을 통한 성장 모델과 나선 성장 모델 등이 개발되었다.

나선 성장 모델의 다양한 종류 중에서 계면 구조 분석 모델은 복합적인 외부 요소로서 두 가지를 제안하였다. 첫 번째 외부 요소는 계면 층 내 성장 단위의 국부 농도이며 두 번째 외부 요소는 계면 층 내 성장 단위의 방향 및 배좌 (配座)에 대한 재배열시 관여되는 자유 에너지 장벽이다. 계면 층 내의 흡착된 모든 용질을 F2-성장 단위,

결정에 포함된 성장 단위와 동일한 방향 및 배좌를 가진 임의의 성장 단위를 F1-성장 단위라고 정의하면, 계면 층 내 F2-성장 단위의 농도와 F2-성장 단위가 F1-성장 단위가 되기 위해 넘어야 하는 자유 에너지 장벽을 분자 동력학 등의 방법을 이용하여 계산할 수 있다. 이 두 가지 외부 요소를 Burton-Cabrera-Frank 이론에 기반을 둔 나선 성장 모델 식에 도입하면 각 면의 상대적인 성장 속도를 구할 수 있다.

본 연구에서는 기존의 계면 구조 분석 모델과 확장된 계면 구조 분석 모델을 성장 단위의 방향 및 배좌에 대해 일반화한 방법론을 제안하였다. 최초의 계면 구조 분석 모델에서는 한 개의 각도를 이용해 F1-성장 단위를 구별하였으며 확장된 계면 구조 분석 모델에서는 두 개 이상의 각도를 이용해 이를 구별하였다. 이 기존 방법들은 고리구조분자 등 복잡한 분자에 대해서는 분자동력학 상에서 배좌에 대한 충분한 표본 추출이 어렵다는 단점이 있다. 이를 극복하는 방안으로써 F1-성장 단위와 그 외 F2-성장 단위를 구별하는 질서변수를 도입하여 각도에 관한 다차원 자유 에너지 평면을 질서변수에 대한 저차원으로 자유 에너지 평면을 차원 감소시키고, 메타동력학을 이용하여 저차원 상의 높은 에너지 장벽을 넘는 방법을 이용하였다. 이 방법과 다각형 나선의 경우를 고려하여 수정된 성장 모델 식을 통해 임의의 중심 대칭성 성장 단위로 이루어진 결정의 형상을 예측할 수 있다.

아디프산과  $\beta$ -HMX는 대표적인 중심 대칭성의 성장 단위로 형성된 결정이다. 각각 사슬형과 고리형 분자라는 특징이 있으며, 이 때문에 이들을 F2-성장 단위의 방향과 배좌의 영향을 보기 위한 모델 물질로써 선정하여 그 형상을 예측해 보았다. 이를 위해 두 결정에 대해 공통적으로 첫 번째 외부 요소인 각 면에 대해 이방성 (異方性)인 계면 층 내 성장 단위의 국부 농도가 결정 형상에 미치는 영향을 고찰해 보았다. 두 번째 외부 요소인 F2-성장 단위의 방향과 배좌의 경우, 아디프산은 방향을 나타내는 F1-성장 단위의 방위각을 통해서,  $\beta$ -HMX은 F1-성장 단위의 3차원 공간상 배열과 의자형 배좌를 각각 구분할 수 있는 사원수(四元數)와 구김 변수로 이루어진 질서 변수 두 개를 통해 계면 층 내의 용질들의 거동을 살펴보았다. 두 외부 요소를 본 연구에서 제안한 다각형 나선 구조를 가정한 모델 식과 기존 계면 구조 분석 모델에서 사용된 동심원 나선 구조를 가정한 모델 식에 대입하여 얻어진 상대 속도를 비교하고 형상을 예측하였다.